A STUDY ON THE FAILURE ANALYSIS OF THE NEUTRON EMBRITTLED REACTOR PRESSURE VESSEL SUPPORT USING FINITE ELEMENT ANALYSIS

by

Goeun Han

A Thesis

Submitted to the Faculty of Purdue University

In Partial Fulfillment of the Requirements for the degree of

Master of Science in Civil Engineering

Lyles School of Civil Engineering

West Lafayette, Indiana

December 2018

THE PURDUE UNIVERSITY GRADUATE SCHOOL
STATEMENT OF COMMITTEE APPROVAL

Dr. Sukru Guzey, Chair
Lyles School of Civil Engineering
Dr. Ayhan Irfanoglu
Lyles School of Civil Engineering
Dr. Ghadir Haikal
Lyles School of Civil Engineering

Approved by:
Dr. Dulcy Abraham
Head of the Graduate Program

This thesis is dedicated to my family,
Jungran Lee, Sungchul Han and Dongmin Han
with love, spirit and encouragement.

ACKNOWLEDGMENTS

This study was made possible by grant from Korea Hydro & Nuclear Power Co.(KHNP). The investigation was carried out at Lyles school of Civil Engineering of Purdue University, West Lafayette.

I wish to express sincere gratitude to all those who supported to build up this research possible.

Dr. S. Guzey is thanked for the continuous support of this study, patience, encouragement, and immense knowledge. His insightful guidance as a mentor made this research a thoughtful and rewarding journey.

Dr. A. Irfanoglu and Dr. G. Haikal are thanked for their valuable comments and suggestions and strengthen the fundamentals of my knowledge, also for the discussion which incented me to widen my research from various perspectives.

Soojin, Yeonjin, Chulmin, Seung-uk Yoonjeong are specially thanked for their guidance and inspiration in all the time of this journey.

I appreciate the warm encouragements from the colleagues of KHNP to achieve my goals throughout the years.

TABLE OF CONTENTS

LIST OF TABLES

LIST OF FIGURES

ABSTRACT

Author: Han, Goeun. MSCE
Institution: Purdue University
Degree Received: December 2018
Title: A Study on the Failure Analysis of the Neutron Embrittled Reactor Pressure Vessel Support using Finite Element Analysis
Committee Chair: Sukru Guzey

One of the major degradation mechanisms in a nuclear power plant structural or mechanical component is the neutron embrittlement of the irradiated steel component. High energy neutrons change the microstructure of the steel, so the steel loses its fracture toughness. This neutron embrittlement increases the risk of the brittle fracture. Meanwhile, the reactor pressure vessel support is exposed in low temperature with high neutron irradiation environment which is an unfavorable condition for the fracture failure. In this study, the failure assessment of a reactor pressure vessel support was conducted using the fitness-for-service failure assessment diagram of API 579-1/ASME FFS-1(2016, API) with quantifying the structural margin under the maximum irradiation and extreme load events.

Two interrelated studies were conducted. For the first investigation, the current analytical methods were reviewed to estimate the embrittled properties, such as fracture toughness and the yield strength incorporates the low irradiation temperature. The analytical results indicated that the reactor pressure vessel support may experience substantial fracture toughness decrease during the operation near the lower bound of the fracture toughness. A three-dimensional (3D) solid element finite element model was built for the linear stress analysis. Postulated cracks were located in the maximum stress region to compute the stress intensity and the reference stress ratio. Based on the stress result and the estimated physical properties, the structural margin of the reactor pressure vessel support was analyzed in the failure assessment diagram with respect to the types of the cracks, level of the applied load and the level of the neutron influence.

The second study explored the structural stress analysis approaches at hot-spot which was found to be key parameter in failure analysis. Depending on the methods to remove the non-linear peak stress and the stress singularities, the accuracy of the failure assessment result varies. As an alternative proposal to evaluate the structural stress in 3D finite element analysis (FEA), the 3D model was divided into two-dimensional (2D) plane models. Five structural stress determination

approaches were applied in 2D FEA for a comparison study, the stress linearization, the single point away approach, the stress extrapolation and the stress equilibrium method and the nodal force method. Reconstructing the structural stress in 3D was carried by the 3x3 stress matrix and compared to the 3D FEA results. The difference in 2D FEA structural stress results were eliminated by the constructing the stress in 3D.

This study provides the failure assessment analysis of irradiated steel with prediction of the failure modes and safety margin. Through the failure assessment diagram, we could understand the effects of different levels of irradiation and loadings. Also, this study provides an alternative structural stress determination method, dividing the 3D solid element model into two 2D models, using the finite element analysis.

1. INTRODUCTION

1.1 Technical Background

For the past several years, nuclear power plant safety enhancement against the extreme hazard has been raised as a prominent issue after experiencing Fukushima Dai-ichi accident in Japan, 2011. This accident was addressed as a demonstration that nuclear reactors must be protected even against accidents which have been assessed as highly improbable in the past [1]. From the European Council`s first step of nuclear power plant safety re-assessment, nuclear safety regulators request to evaluate safety margin beyond the design basis (which is called as "stress test"). Stress tests is the evaluation of current structure, system and component (SSC) under applying the high confidence of low probability of failure factor [2].

Meanwhile, not only the increased level of the hazard events but also the material degradation under the radiation environment is critical for the long-term operation of a nuclear power plant. In particular, the structural steel in a nuclear facility experiences considerable degradation due to accumulated neutron irradiation. The high energy neutron hardens the steel with lowering the fracture toughness (see Fig. 1.1). Therefore, a brittle fracture may occur when subjected to stress increase such as pressurized thermal shock events or the strong earthquake events. Therefore, the reactor pressure vessel toughness research has been a significant issue in the nuclear industry and numerous studies have been carried including performing experiments and building computational models to prevent the brittle fracture of the reactor pressure vessel. However, in the reactor cavity, there is another structure exposed to the neutron embrittlement. It is the reactor pressure vessel support which supports the vessel and maintains the primary coolant system in stable position. The U.S. Nuclear Regulatory Committee (NRC) investigated the reactor pressure vessel support embrittlement from late 1970s and published an investigation report of the reactor pressure vessel support in 1996 [3]. Since the U.S. NRC did not investigate the long column type support because the number of the long column type supports were only found in 9 in 125 nuclear power plants in U.S., the long column type reactor pressure vessel support has not been studied. Considering the increased stress events under the extreme load and the neutron irradiated embrittlement, in this study, the failure assessment of reactor pressure vessel support was investigated.

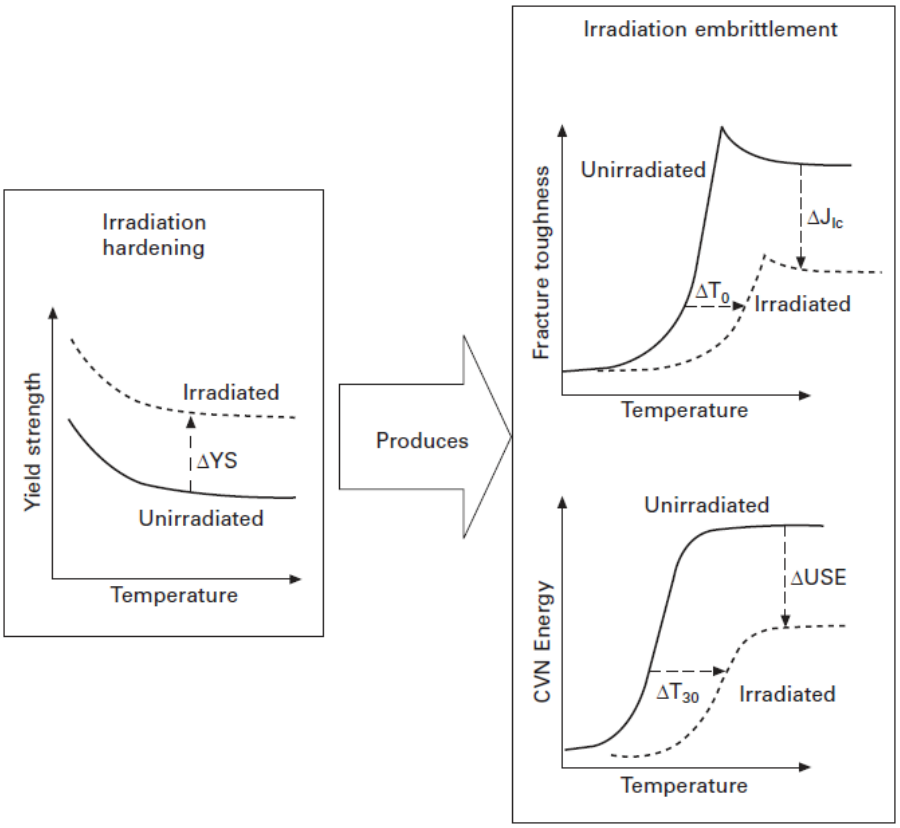

Fig. 1.1 Schematic relationship between changes in temperature dependences in yield stress, DBTT from Charpy impact and fracture toughness (Figure from Irradiation hardening and materials embrittlement in light water reactor (LWR) environments, Brumovsky [4])

For the representative model of reactor pressure vessel support, the APR1400 pressurized water reactor (Advanced Power Reactor with electrical power output of 1,400 MWe) was selected because it is classified as one with long-column type support which had been analyzed as 'susceptible for radiation damage' and it is exposed to neutron embrittlement for long designed-life [5].

The ASME Boiler and Pressure Vessel Code Section XI [6] provides a straightforward calculation for checking the stress intensity only. To estimate the failure modes and structural margin between the brittle fracture and ductile failure in each phases (see , Fig. 1.2) according to the neutron fluence levels, the fitness-for-service failure assessment diagram from the API 579-1/ASME FFS-1 [7] was implemented in this study. This standard provides detailed guidance with comprehensive procedures. The concept of the failure assessment diagram is widely accepted in

many other industries and their documents, such as the British standard, BS 7910 [8], SINTAP [9], also used in R6 [10] procedure of UK nuclear industry flaw assessment.

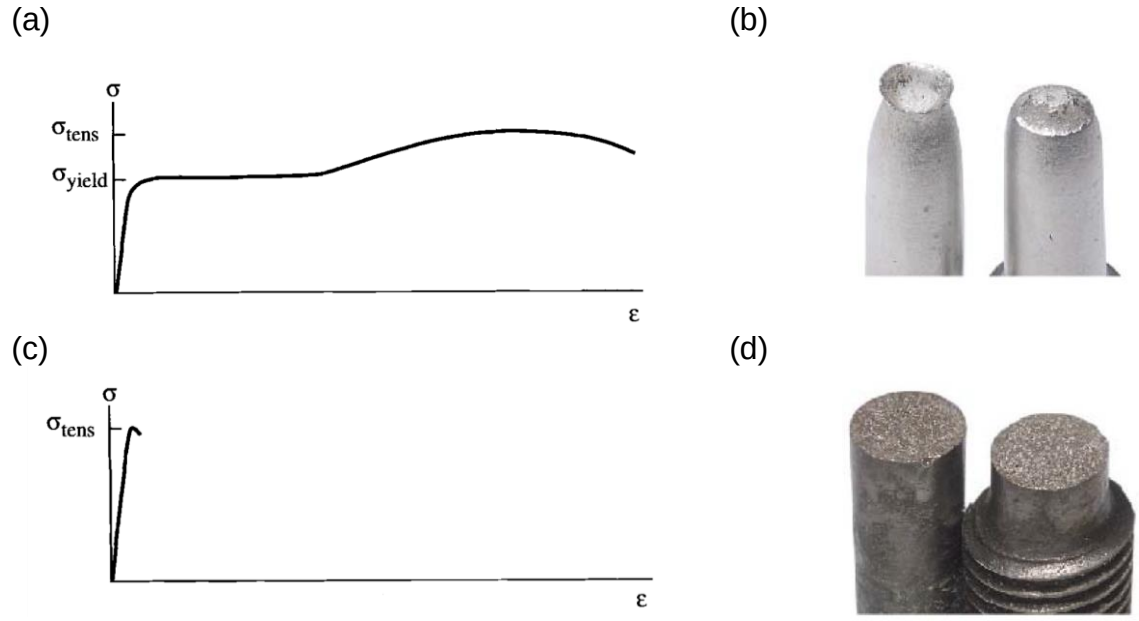

Fig. 1.2 Comparison of curves for ductile and brittle materials

(a) stress-strain curve of the ductile material (b) ductile failure (c) stress-strain curve of the brittle material (d) brittle fracture (Figure (a) and (c) from *Fracture and Fatigue Control in Structures*, Barsom and Rolfe [11], Figure (b)and (d) from *Materials Science and Engineering: An Introduction*, Callister and Rethwisch [12])

The degradation of the physical properties under the estimated neutron fluence by analytical methods was investigated based on the previous researches on reactor pressure vessels. The low irradiation temperature played important role in the embrittlement of reactor pressure vessel support. A structural stress analysis by linear finite element analysis to compute the structural stress was performed with three-dimensional solid element model. Unlike the vessel and the piping, the support is relatively thick, so it needed further computational method for the structural stress analysis, particularly at the maximum structural stress regions such as geometry discontinuities. Focusing the importance of the accuracy of stress value in failure assessment, a structural analysis alternative approach was proposed using two-dimensional model comparing the five structural stress estimating approaches, the stress linearization, the single point away approach, the stress extrapolation and the stress equilibrium method and the nodal force method.

1.2 Research Objectives

The objective of the study is to analyze the neutron embrittled structure by failure assessment and estimate the failure modes and the structural margin to diagnose the structural integrity during the designed life of nuclear power plant. This objective will be processed as follows.

1. Estimate the physical properties of irradiated reactor pressure vessel support
2. Assess the structural safety margin under the different level of the neutron fluences and loading
3. Propose a structural stress estimating approach for the failure assessment of solid element finite element model

1.3 Thesis Outline

This thesis is consisted of three chapters. Chapter 2 starts with review of the previous studies of the neutron embrittlement on reactor pressure vessel and suggests the estimating equations for the RPV steel considering the low irradiation temperature. Degradation of the physical properties degradation with neutron fluence level is presented in this chapter. A stress analysis by 3D FEA was performed and the physical properties were derived for the failure assessment by the API 579-1/ASME FFS-1(2016). The assessment provides comprehensive results with respect to types of postulated crack, the effects of the neutron irradiation and level of the load.

In the chapter 3, an alternative structural stress determination method is proposed. The structural stress applied in chapter 2 is examined with five different analysis approaches to estimate the maximum structural stress. The 3D model was cut into two 2D models to apply the previous structural stress approaches and they are reconstructed by 3D matrix by each approach for comparison study.

Lastly, the chapter 4 summarizes the main conclusion of each chapter and provides the further research topic.

2. FAILURE ASSESSMENT OF IRRADIATED REACTOR PRESSURE VESSEL SUPPORT

2.1 Introduction

Irradiation has been considered as a critical degradation mechanism of the mechanical and structural components of a nuclear power plant. One of the great concerns of irradiation is that the high energy neutron changes the microstructure and physical properties of steel which is a major material of a nuclear power plant. Particularly, as the neutron exposure increases overtime, the irradiated steel substantially loses its fracture toughness. This reduced fracture toughness is called neutron embrittlement. In an event that increases the structural stress of a mechanical or structural component, such as an earthquake or a pressurized thermal shock which are more severe than the design event, the irradiated steel component may fail with an abrupt brittle fracture rather than a ductile failure. This is because the neutron embrittlement increases the possibility for propagation of flaws that might exist in the steel component.

In a nuclear power plant, neutron embrittlement generally occurs in the confined cavity structure where the reactor pressure vessel and the reactor pressure vessel supports are located. Based on the International Atomic Energy Agency (IAEA) technical report [13], reactor vessel embrittlement is rated as one of the life-limiting risk factors for a nuclear power plant. The steel material of a reactor pressure vessel (RPV) is monitored by periodically testing specimens which are pre-installed in the vessel. However, the reactor pressure vessel support is apart from the neutron irradiation sources, and the support has 1) no in-service assessment after installation and 2) they are generally in the lower temperature compared with the RPV which a disadvantageous condition for the brittle fracture resistance is.

With these concerns raised in the late 1970s, the U.S. Nuclear Regulatory Commission (NRC) classified the RPV supports embrittlement as a safety issue [14]. Later, in the NRC resolution report [15], there were two types of RPV supports classified as the vulnerable supports for the high radiation damage: the short-column and the long-column type supports. However, only the short-column type support was investigated because about 75% of the U.S. pressurized water reactors (PWR) had the short-column type support while only nine U.S. PWR vessels were supported with the long-column type support. However, the long-column type reactor pressure vessel supports have been built globally over the last few decades.

One of the notable nuclear power plant designs that this study is focused on is the APR 1400 nuclear power plant, 1400 MWe advanced pressurized water reactor with four long-column type reactor vessel supports. The APR 1400 has 60-year design life which means that the supports will be exposed to the neutron embrittlement for 20 years longer than the investigated nuclear power plant at the NRC resolution report [15]. Considering this reason, the APR 1400 RPV supports were chosen for the structural model and for the fracture toughness calculation applying the data from the design documents [16] to the numerical analysis.

Recent research related to the neutron irradiation of reactor vessel supports is the EPRI's technical report [17] focusing on the irradiated concrete model proposed by Le Pape [18]. Different types of irradiated RPV steel have been studied with various approaches [19–22] and the relation between decreased toughness and the crack stress in RPV has been investigated with multiple approach [23,24]. The probabilistic fracture analysis model, such as FAVOR of U.S. NRC [25], has been used for the failure analysis [26–29]. While the stress intensity factors of ASME Section XI have been improved with detailed equations covering various kinds of cases [19], the fitness-for-service (FFS) assessment methodology also has been applied for the nuclear industry. Using the FFS methodology, the structural integrity of steam generator tubes and steam lines were investigated [30–32] and the pressure vessel under fire damage also assessed by FFS [33]. In Japan, from 2008, the Japan Society of Mechanical Engineers (JSME) applied the FFS methodology for nuclear power plants and has been developing the detailed solution [34,35]. However, a FFS of neutron irradiated RPV supports has seldom been performed.

The aim of this study is to understand the features of the irradiated steel's structural integrity by exploring the implementation of a fitness-for-service assessment methodology, incorporated in both the degraded fracture toughness by the neutron embrittlement and the structural failure mode under the extreme events.

The assessment methodology followed is the fitness-for-service (FFS) approach of API 579-1/ASME FFS-1[7], hereafter referred to as API 579, to quantify the structural margin and predict the most probable failure mechanism, brittle fracture, the plastic collapse or the combination mode. The fitness-for-service provides the quantitative engineering evaluation of an in-service component that might have flaws and has already been implemented among a wide variety of industries with massive steel components, such as oil and gas, power, chemical and marine industries.

For postulating flaws and stress analysis, three-dimensional linear elastic finite element analysis was used with perfect geometry without any modeled crack to cover the interaction that geometry and loadings generate giving sufficient plausible basis in assumption of the flaws. Based on these failure assessment results, the flaws were diagnosed to understand their contribution to failure in severe environments and compared with the current allowable limits. In each irradiation level and load level, the structural safety margins were calculated taking account of the RPV supports dominant failure behavior.

This study begins with a brief overview of the RPV support design and previous related research. The technical review of failure assessment and the environmental parameter study are covered in the following section 2.3. With these determined parameters, the section 2.4 methodology provides the analytical methods used and the stress analysis result in detail. In sections 2.5 and 2.6, the numerical failure assessment results are discussed.

2.2 Background

This section will cover the background of the RPV supports discussing the structural impacts, the previous studies of the irradiation damage of RPV supports and the design overview of APR 1400 long-column type supports.

2.2.1 Importance of Structural Integrity of RPV Supports

The role of the RPV supports is to transfer loads from the reactor vessel to the adjacent structure located in the reactor cavity between the RPV and the shield wall. The RPV supports hold the RPV in both the horizontal and vertical (gravity) directions. They not only support the dead load, but also transmit the lateral load to the reactor cavity structure.

Furthermore, the RPV supports with the steam generator support and the reactor coolant pump support are in a group and maintain the primary reactor coolant system in their position. Failure of RPV support may allow the reactor pressure vessel to move and consequently may impact the whole primary reactor coolant system stability. Eventually, the structural failure of RPV supports may worsen the loss of a coolant accident.

2.2.2 Previous Studies Related to the RPV Support

In 1981, the U.S. Nuclear Regulatory Commission, NRC, addressed a generic safety issue, GSI-15, "Radiation Effects on Reactor Vessel Supports" to solve the concern that low-temperature and low-energy neutron irradiation may embrittle the RPV supports rapidly as described in NUREG-0705 [14]. After the safety issue was announced, many investigation reports on the RPV supports had been published. In 1989, the Oak Ridge National Laboratory report submitted to NRC [5] concluded that the low-flux may produce excess embrittlement rate and the critical crack size was predicted as 0.42 in. (10.67mm) depth and 2.5 in. (63.5mm) long under the small-break loss-of-coolant accident.

Unlike the RPV, the RPV support types and the environmental conditions varied depending on their design, the structural shape, material and the level of the neutron fluence. Considering these data, the reevaluation request was done in a specific design case that can be representative of the RPV supports of the time. The investigators did structural analysis, probabilistic risk assessments and collected metallurgical degradation data. As a result of these investigations, the safety issue was resolved stating that the RPV irradiation was no longer a safety issue [3]. For the investigation mentioned above, two U.S. plants were selected as for the most vulnerable cases. The investigated RPV supports were expected to experience the brittle fracture after 23 effective-full-power-years (EFPY) during the 30 EFPY design life [36]. However, base on the results of the two studies, the disaster frequency caused by the failure of the RPV supports and the estimated consequences were found to be low.

The consequence of failure of the RPV supports were predicted as a safe condition because the short pipe between the reactor pressure vessel and the cavity wall was evaluated and it found to support the coolant system. In spite of this promising result, there is still a need to investigate the RPV supports subjected to irradiation in light of the current nuclear power plant designs. In NRC report [15], the two nuclear power plants that were selected had short-column type RPV supports. Even though the long-column type supports are exposed in high-irradiation damage zone, the long-column type supports were rare in the U.S. as mentioned earlier. Furthermore, as the two nuclear power plants investigated were assessed to have brittle fracture after 23 EFPY, the APR 1400 power plant with 56 EFPY may be exposed to the risky brittle fracture situation for 33 years of EFPY. This is much longer than the NRC report had considered.

2.2.3 Overview of RPV Long-Column Type Support

There are four cold leg (inlet) nozzles of reactor coolant system attached to the APR 1400 RPV. Under each nozzle, the RPV support is installed vertically supporting the RPV [16]. The RPV supports are arranged around the reactor pressure vessel, located within 1.5 ft (0.46 m) from the RPV outside surface as shown in Fig. 2.1. The RPV supports are located in the reactor cavity, facing the RPV's belt line, and the base plates are anchored to concrete. In accordance with the ASME BPVC Section III, Division 1 [37], these RPV supports are classified as a linear-type support which is evaluated by the allowable stress values. Among the types of the RPV supports classified in NRC investigation reports, this type of support is classified as the long-column support because it is extended from the base of the cavity to the inlet nozzle and the whole part is exposed to the irradiation environment.

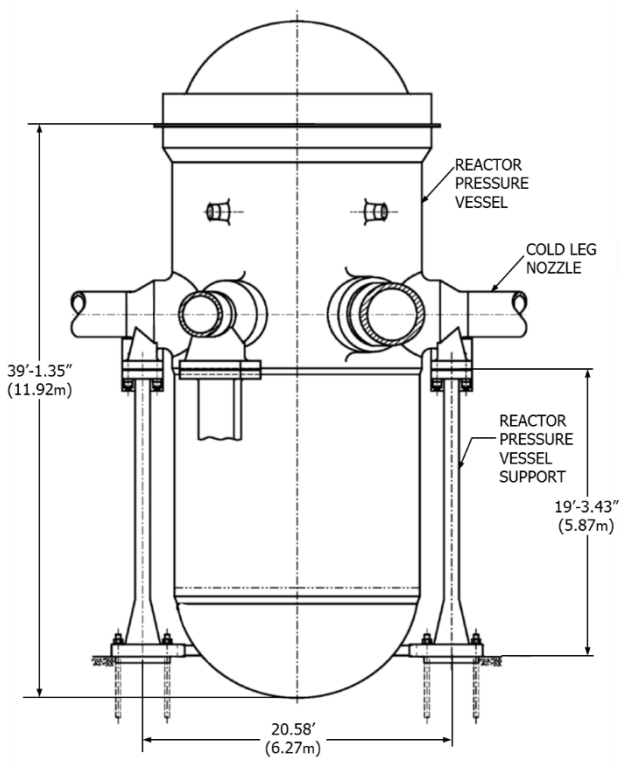

Fig. 2.1 Elevation view of APR 1400 reactor vessel and reactor vessel supports
(Adopted from APR 1400 design control document, 2014, modified)

The support is made from ASME SA 508 grade 3, class 1 [38] steel by forging, manufactured in one large piece, which is the identical material used in the reactor pressure vessel steel. The overall height of the RPV support including the shear key at the bottom end is approximately 20 ft (6.1 m). The column support has a 30 ×11 in. (762 × 279.4 mm) rectangular cross section facing the reactor pressure vessel on its long side. The RPV support consists of a base plate, support column and flange plate and shear key under the base plate. Fig. 2.2 provides a schematic view of a RPV support with each part pointed out. Each part is smoothly continued with a typical fillet radius of 1 in. (25.4mm). The shear key is embedded in the concrete slab for restraining the movements in the bottom to prevent the primary coolant loop failure. The flange plate is connected to the nozzle pad with bolts and allows for the RPV's thermal expansion and limits the horizontal movement. At the bottom of the column support, the rectangular section expands to a trapezoidal-shaped segment connected to the base plate.

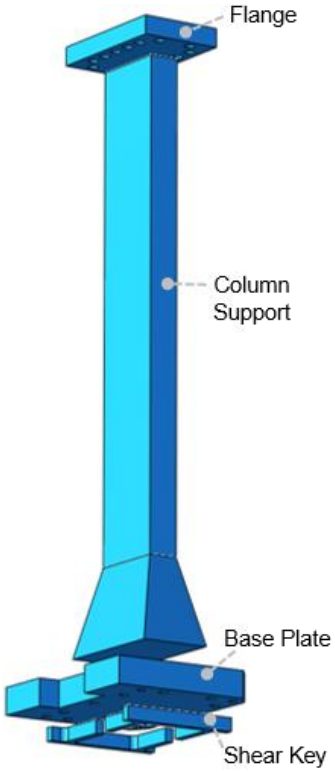

Fig. 2.2 Schematic view of the long-column type reactor vessel support
(Note that the actual RPV support is a monolithic forged member, not separated.)

A structural assessment of APR 1400 long-column type support was recently provided by Nguyen and Namgung [39]. They proposed a plate-type support system as an alternative type of support for the APR 1400 by using finite element analysis and assessed the structural capacity of the long-column type support since the column-type support has a higher chance to absorb energy during a seismic event and may transfer the amplified displacement to the reactor pressure vessel. The long-column type support was evaluated as satisfying the ASME code allowable limits. However, they have not studied the irradiation embrittlement of the supports.

2.3 Technical Overview

This section includes the current available failure assessment methods focusing on the failure assessment diagram (FAD) of the FFS evaluation. The fracture toughness measurement and the assessment conditions to be determined are discussed in this section as well.

2.3.1 FAD Approach

The FAD approach is used in the FFS evaluation to determine the structural integrity of a component with a crack-like flaw. The RPV support structural integrity should consider various conditions that may cause a failure, from the loss of toughness by irradiation to the plastic collapse due to an extreme load. To compromise for this wide range of failure modes, from linear elastic to fully plastic behavior, the FAD approach is implemented in this study. As illustrated in Fig. 2.3, the FAD approach determines not only where the assessment point falls, in the acceptable or unacceptable region, but also indicates the nature of the failure based on interaction between the toughness and the load as two parameters. The toughness ratio is resistance to brittle fracture and the load ratio indicates the resistance to plastic collapse. These will be discussed in more detail in Section 2.4.

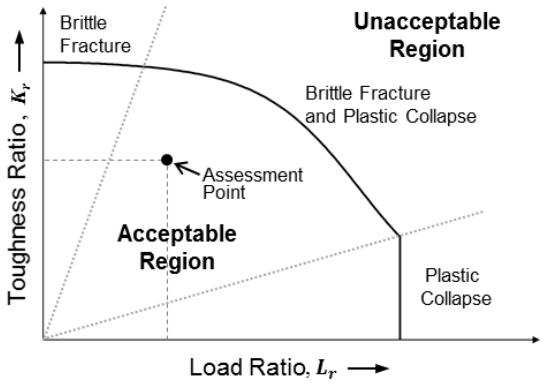

Fig. 2.3. Overview of an FFS analysis using the FAD approach

The RPV design documents require the use of ASME BPVC Section XI [6] to evaluate the embrittlement fracture for the RPV and its support. This approach assesses the structural safety by using the mathematical relationship between the fracture toughness and the stress intensity. As the irradiated embrittlement is a great concern in RPV safety, codes and regulations have focused on the fracture toughness in the matter of the linear elastic fracture mechanics method (LEFM) [40,41]. When the reactor pressure vessel is in the ductile region with the high toughness, it is hard to characterize the plastic failure because the LEFM does not include the plastic collapse and the possible ductile plasticity effects at the flaw [42]. For this case, the ASME Section XI additionally introduces other approaches for the elastic-plastic fracture behavior, such as J-integral, J-R curve or FAD approach for crack depth of one- quarter of the wall thickness [6,42]. Given that both RPV and its support are made of identical material specification, exposed in a similar irradiation environment, this failure assessment of the RPV supports should consider both the LEFM method and the elastic-plastic fracture assessment method to incorporate the degree of the fracture toughness.

The FAD approach is a useful approach because it covers both LEFM and ductile overload behavior. Additionally, with the need for the extreme hazard evaluation against a significant extreme load, the nuclear power plant structural components should be assessed in simplified quantitative results to check the current safety status and the structural margin against the expected failure mode.

2.3.2 FAD Technique used in This Study

Currently, the two of the widely used documents for the fitness-for-service using the FAD approach are the API 579 [7] and the BS 7910 [8]. According to the Larrosa and Ainsworth [43], these two standards and the another FFS guide, R6 [10] for UK nuclear industry show some divergent results depending on the crack size, level of the residual stress and other features. However, this study followed the API 579 rules because the API 579 provides the pressure vessel fracture toughness equation and the maximum permitted load ratio value for ASME SA 508 material.

In API 579, part 9, crack-like-flaws assessment is applied. This procedure provides a guide to evaluate a structural component with a crack-like flaw that has a given depth and length, and covers the brittle fracture behavior. The level 3 assessment was selected to consider the crack growth and the FAD envelope was built by method ‘A’ assessment.

2.3.3 Measurement of Fracture Toughness of Structural Steel

The U.S. NRC regulatory guide [41] introduces two methods to predict the fracture toughness of irradiated steel. One is an experimental method and the other one is an estimation based on analytical methods. Since the RPV support, that are in-service do not have specimens to do impact test, or it needs to be evaluated by analytical methods or non-destructive methods. A non-destructive monitoring method for radiation damage was introduced by Matlack et al. [44] providing the correlation with the microstructural radiation change and nonlinear ultrasonic measurement results. Similarly, the analytical method using the temperature and the fracture toughness relation is widely in use with an extensive fracture toughness data set accumulated for decades.

The fracture toughness varies from ductile to brittle at around a particular temperature point as shown in Fig. 2.4. This transition point is called the reference nil-ductility temperature and it is found that the irradiation embrittlement increases the transition temperature. This nil-ductility transition temperature shift (TTS) is used as the indicator of irradiation embrittlement in numerous analytical methods and discussed in section 2.4.

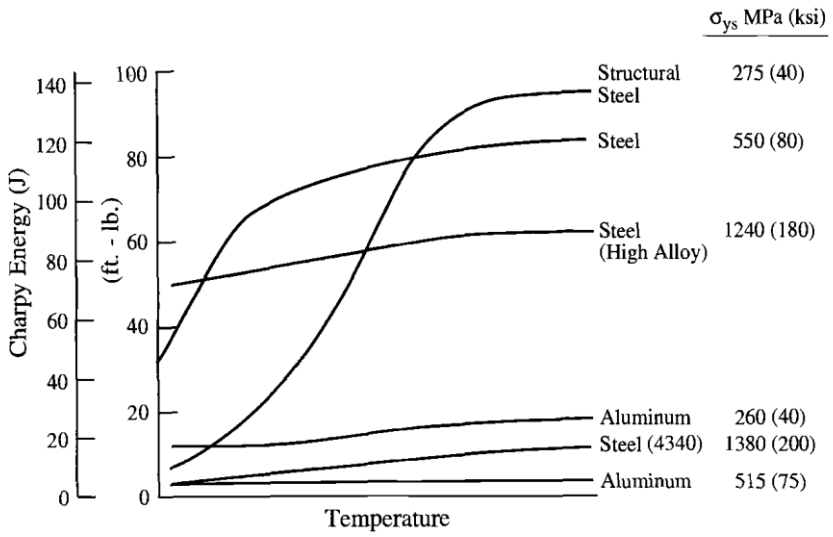

Fig. 2.4 Charpy V-notch impact energy versus temperature behavior for selected structural materials (Figure from Fracture and Fatigue Control in Structures (Barsom & Rolfe [11]))

2.3.4 Assessment Conditions of the RPV Supports

There are four major condition parameters needed for the assessment: 1) in-service temperature, 2) assessment temperature, 3) neutron fluence and 4) the applied loads. The two temperature parameters and the neutron fluence are used for the fracture toughness determination and the applied loads are for the stress levels for the FAD approach. This study referenced ASME Class 1 supports design requirements in ASME Section III-1 and the APR 1400 design documents [16] for the assessment conditions of the RPV support. The assessment conditions of the RPV supports are defined in Table 2.1 and Table 2.2

Table 2.1 In-service temperature (irradiation temperature, T_i) of RPV supports

Part	Level [a], in. (cm)	Temperature, ° F (° C)
Flange	231 in. (587 cm)	330° F (166° C)
Column	224 in. (569 cm)	270 ~ 100° F (132~38° C)
Base	10 in. (25 cm)	350° F (177° C)

[a.] Measured at top level of each part, from the bottom of the support.

Table 2.2 Analysis parameters for different fluence levels

Parameters	Fluence Level [a, b]								
	5% MDF [c]			25% MDF [d]			100% MDF [e]		
	Base	Column	Flange	Base	Column	Flange	Base	Column	Flange
T_i, ° F (° C)	350 (177)	150 (66)	330 (166)	350 (177)	150 (66)	330 (166)	350 (177)	150 (66)	330 (166)
E, ksi (MPa)	26,450 (1.82E+5)	27,370 (1.89E+5)	26,275 (1.81E+5)	26,450 (1.82E+5)	27,370 (1.89E+5)	26,275 (1.81E+5)	26,450 (1.82E+5)	27,370 (1.89E+5)	26,275 (1.81E+5)
ΔRT_{NDT}, ° F (° C)	31.3 (-0.39)	54.7 (12.61)	41.8 (5.44)	81.4 (27)	126.8 (53)	85.9 (30)	172.2 (77.9)	257.2 (125.1)	180.6 (82.6)
ART , ° F (° C)	101.5 (38.61)	124.9 (51.61)	112 (44.44)	151.6 (66.4)	196.9 (91.6)	156.1 (68.9)	242.4 (116.9)	327.4 (164.1)	250.8 (108.6)
K_{IC}, ksi$\cdot\sqrt{in.}$ (MPa$\sqrt{m}$)	42.24 (46.42)	38.86 (42.70)	41.83 (45.97)	36.52 (40.13)	34.54 (37.96)	36.23 (39.81)	33.70 (37.03)	33.30 (36.59)	33.66 (36.99)
σ_{ys}, ksi (MPa)	57.06 (393.41)	61.98 (427.34)	57.58 (397)	57.03 (393.21)	61.98 (427.34)	57.58 (397.00)	57.06 (393.41)	61.98 (427.34)	57.58 (397)

[a.] For all fluence levels, following parameters are identically applied. Assessment temperature: 60° F (16° C), initial RT_{NDT}: 40° F (4.4° C), Poisson's ratio: 0.3, Temperature Margin calculated as an absolute value 30.2° F (16.8° C)

[b.] The initial state: K_{IC}: 84 ksi·√(in.) Yield strength: 44.8 ksi for base, 48.1 ksi for column, 45.1 ksi for flange

[c.] 5% MDF: fluence level, f = 1E+17 n/cm^2, flux $\emptyset_t$=2.58E+17 n/cm^2

[d.] 25% MDF: fluence level, f = 5E+17 n/cm^2, flux $\emptyset_t$=1.29E+18 n/cm^2

[e.] 100% MDF: fluence level, f = 2E+18 n/cm^2, flux $\emptyset_t$=5.15E+18 n/cm^2

Table 2.1 shows the in-service temperature of RPV supports provided in the design document. The in-service temperature of RPV support is estimated from 100° F (38° C) to 350° F (177° C), lower than 550° F (288° C) which is the reactor pressure vessel normal operating temperature.

The RPV support in-service temperature depends on the distance from the thermal sources, such as the reactor pressure vessel or the reactor coolant nozzle. The distance along the vertical level and the in-service temperature are presented in Table 2.1. Given that the neutron irradiation embrittlement proceeds while the reactor pressure vessel operates, the in-service temperature is used as the irradiation temperature, which is T_i in this study. The in-service temperature determines the elastic modulus of the steel material and the yield strength, provided the data from ASME BPVC Section II-D [45]. These values are presented in Table 2.2 for different percentages of maximum designed fluence (MDF).

The assessment temperature, T is defined as 60° F (16° C) in this study. This temperature is the lowest normal room temperature inside the nuclear power plant. During the extreme events such as a loss of coolant accident which is regarded as the harshest environment of the reactor pressure vessel, the temperature may go up to 360° F (182° C) in tens of seconds and cools down back to normal room temperature. The assessment temperature applied in this study is a highly severe postulating environment for a conservative fracture assessment approach.

For the 60-year designed life, the RPV supports are expected to have 2.0×10^{18} neutrons per square centimeter which have over 1.0 MeV energy. In order to track changes in the structural integrity with neutron irradiation, this study will divide the 60-year designed life into seven sequences depending on the accumulated neutron fluence. The 60-year neutron fluence is expressed with 100% MDF. The seven intermediate assessments are at 5% MDF, 15% MDF, 25% MDF, 50% MDF, 75% MDF and 100% MDF including the initial unirradiated state. The 25% to 100% MDF sequences were associated with the reactor pressure vessel surveillance test schedule from ASTM E 185 [46].

Two loading cases were considered which are outlined in ASME Section III-1: one is the level B load case for normal operation load and the other one is the level D service load case for the extreme loads. The level B load case includes the deadweight, operation loads, thermal load and in-containment refueling water storage tank discharge loads. The level D load case is the most severe event load case. The values are determined by APR 1400 design specification. The Level D load case permits the faulted condition in low probability and postulated events which may produce gross deformation with some loss of stability and damage. The events include the safe shutdown earthquake, dynamic system loadings and pipe breaks including the normal operating loads. The loads were converted in quasi-static conditions and given in section 2.4.3.3.

2.4 Methodology

The overall failure assessment procedure is described as a flowchart in Fig. 2.5. The models of RPV supports were built for the stress analysis using the finite element program, ABAQUS [47].

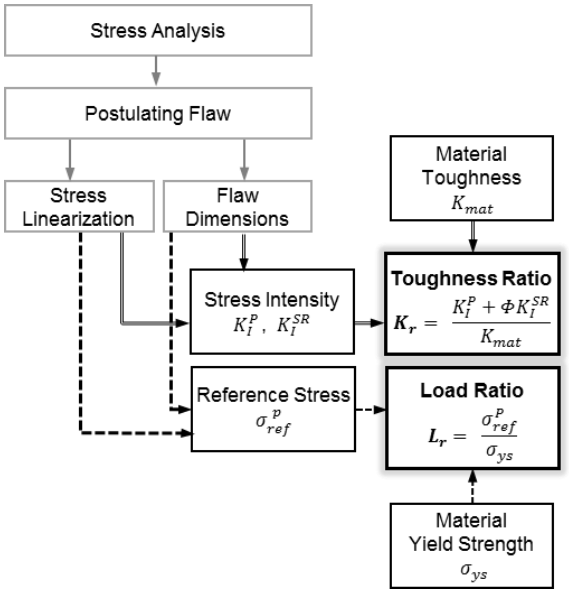

Fig. 2.5. Overall failure assessment procedure for the reactor vessel support

Material properties under irradiation environment were quantified by analytical methods. A typical FAD diagram and a generic assessment point are shown in Fig. 2.3, K_r. As expressed in Equation (1), K_r is the ratio of stress intensity factors, K_I^P and K_I^{SR} to the material fracture toughness, K_{mat}, where K_I^P and K_I^{SR} are stress intensity factors based on the primary stress and secondary stress, respectively. Φ is the plasticity interaction factor.

$$K_r = \frac{K_I^P + \Phi K_I^{SR}}{K_{mat}} \tag{1}$$

Similarly, the assessment value in the horizontal axis of FAD is the load ratio, L_r. As shown in Equation (2), the L_r is calculated as the ratio of reference stress, σ_{ref}^p to the material yield strength, σ_{ys}.

$$L_r = \frac{\sigma_{ref}^P}{\sigma_{ys}} \tag{2}$$

With the assessment values, K_r and L_r, the cracks were evaluated based on their location in the FAD as shown in Fig. 2.3. The first step of this study is to determine the expected material properties, the fracture toughness, K_{mat}, and yield strength, σ_{ys}. Second, a stress analysis was carried out for postulated flaws and the stress classification. Then, based on the flaw size and the stress analysis result, the stress intensity factors K_I^P , and the reference stress, σ_{ref}^p were obtained by solutions from API 579.

2.4.1 Fracture Toughness

2.4.1.1 Basic Method

The fracture toughness is defined as the ability of a material to resist crack initiation and propagation [7]. In Table 2.2, the fracture toughness, K_{IC}, and other material properties of the RPV supports were tabulated on the basis of the neutron fluence level($\emptyset_t$) and the irradiation temperature (T_i).

Because the RPV supports have no available fracture toughness test data, this study followed a conservative estimate method of ASME Section XI. The RPV supports are made of SA-508 which is the same material specification as the RPV which has a large material testing data set as it is required per 10 CFR 50 [40]. Therefore, we referenced the available RPV material testing data set and analysis results in our study. The fracture toughness was measured in-plane strain fracture toughness in terms of the critical stress intensity factor, K_{IC}. The K_{IC} is computed with the temperature parameter using Equation (3) from ASME Section XI which is also prescribed in API 579.

$$K_{IC} = 33.2 + 20.734 \exp[0.02(T - RT_{NDT})] \qquad (ksi\sqrt{in}, °F) \tag{3}$$

where T is the assessment temperature, 60° F (16° C). The term RT_{NDT} is defined as the highest adjusted reference nil-ductility temperature. This RT_{NDT} includes the transition temperature due to the effect of neutron irradiation embrittlement, $\Delta RT_{NDT.}$

The ASME Section XI recommends determining RT_{NDT} from the NRC regulatory guide 1.99 (U.S. NRC, 1988). In this guide, the highest adjusted reference temperature, RT_{NDT} is expressed as ART, adjusted reference temperature and is calculated by the following equation.

$$RT_{NDT} = ART = Initial\ RT_{NDT} + \Delta RT_{NDT} + Margin \tag{4}$$

where $Initial\ RT_{NDT}$ is given as 40° F (4° C) as the unirradiated reference temperature per project design specification. The margin is to be added for uncertainties in the values, set as 30.2° F (16.8° C) following the RPV's margin. The term, ΔRT_{NDT} is the irradiation effect adjustment derived by an analytic method from the Oak Ridge National Laboratory report [48,49]. This report expresses the ΔRT_{NDT} as the transition temperature shift, TTS. The equations for TTS are shown as follows from Equations (5) to (14). The TTS is the sum of the two terms, the matrix feature (MF) term and a copper-rich precipitate (CRP) term.

$$\Delta RT_{NDT} = TTS = MF\ term + CRP\ Term \quad (5)$$

$$MF\ term = A(1 - 0.001718T_i)(1 + 6.13PMn^{2.47})\sqrt{\emptyset_{t_e}} \quad (6)$$

$$CRP\ term = B(1 + 3.77\ Ni^{1.191})\left(\frac{T_i}{543}\right)^{1.1} f(Cu_e, P)\ g(Cu_e, Ni, \emptyset_{t_e}) \quad (7)$$

$$\emptyset_{t_e} = \emptyset_t \left[\frac{4.39 \times 10^{10}}{\emptyset}\right]^{0.259} \quad (8)$$

$$f(Cu_e, P) = [Cu_e - 0.072 + 1.359(P - 0.008)]^{0.668} \quad (9)$$

$$g(Cu_e, Ni, \emptyset_{t_e}) = \frac{1}{2} + \frac{1}{2}\tanh\left[\frac{\log_{10}(\emptyset_{t_e}) + 1.139Cu_e - 0.448Ni - 18.12}{0.629}\right] \quad (10)$$

where,

$A = 1.140 \times 10^{-7}$ (Coefficient for forging)

$B = 102.3$ (Coefficient for forging)

$Cu_e = 0.15$ (Effective amount of Cu weight percent)

$P = 0.015$ (Phosphorous weight percent, followed ASME SA 508)

$Mn = 1.5$ (Manganese weight percent, followed ASME SA 508)

$Ni = 1$ (Nickel weight percent, followed ASME SA 508)

$\emptyset$ = 1.14E+09 n/cm^2/s (Neutron flux, based on 55.8 effective full power years)

$\emptyset_{t_e}$ = Effective fluence computed with each expected neutron fluence, $\emptyset_t$, refer to Table 2.2

T_i = Irradiation-temperature (in-service temperature) refer to Table 2.1

2.4.1.2 The Effect of the Low Irradiation Temperature

The low irradiation temperature (T_i) of RPV support should be considered as a reducing factor against the fracture toughness. Five analytical methods were selected and the comparison of TTS results, with respect to each irradiation temperature are shown in

Fig. 2.6. The Oak Ridge National Laboratory method (ORNL/TM-2006/530) gives conservative result for the in-service temperature of reactor vessel and a moderate value for the low irradiation-temperature. Therefore, the Oak Ridge National Laboratory method was used in this study. Next, other analytical methods will be discussed with a brief comparison.

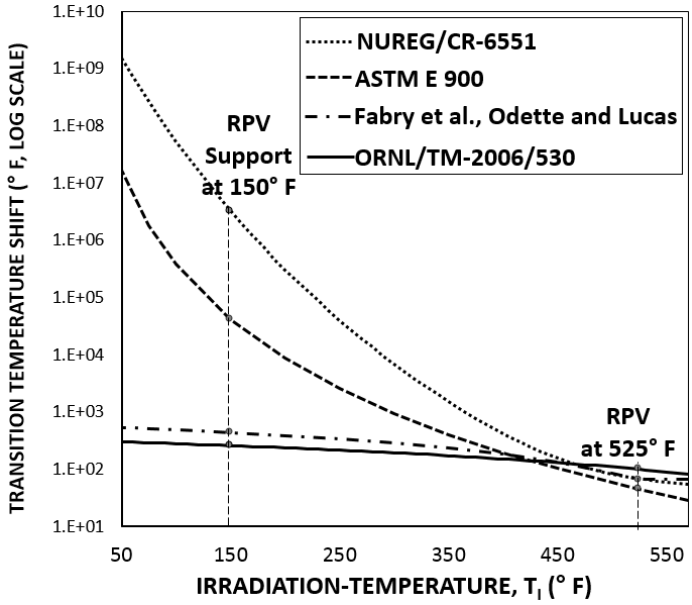

Fig. 2.6. Plots for transition temperature shift (TTS) and for irradiation-temperature (Ti) and by analytical methods

The methods to predict the transition temperature trend were developed by using data from decades of RPV surveillance tests. While the reactor pressure vessel has 550° F (288° C), the RPV support irradiation temperature is only between 150° F (66° C) and 350° F (177° C). The NRC guide [41] recommends to consider the irradiation-temperature effect stating that when the irradiation temperature is under 525° F (274° C), a greater embrittlement effect is expected. It is because the NRC regulatory guide was based on the RPV surveillance tests. Another analysis report from EPRI [50] also suggested an analytical method mentioning that an irradiation temperature from 527° F (275° C) to 590° F (310° C) is reasonable. Haggag [51] also observed the increase of transition temperature shift in low irradiation temperature, from the investigation of modular high-temperature gas-cooled reactor, which runs at relatively lower temperature than the commercial Light Water Reactor (LWR) does.

Fabry et al. [52] studied the outlier values of some LWR vessel steels including the low irradiation-temperature, 500° F (260° C) from the Yankee and BR3 nuclear plants. In this analysis, the temperature correction factor penalty is given as a -1° C (-1.8 ° F) shift per 1° C (1.8 ° F) difference at irradiation temperature. Similarly, Odette and Lucas [53] observed an irradiation temperature decrease with the average of 1 ± 0.2° C/° C (1 ± 0.2° F/° F). In 1998, the U.S. NRC released a further detailed report, NUREG/CR-6551 [54] specifying contribution of each

parameter. From the numerous experimental data, the report identified a 0.6° F (0.33° C) temperature shift per lower temperature median value in the range of 520° F (271° C) to 580° F (304° C). The report, ORNL/TM-2006/530, from the Oak Ridge National Laboratory [48], found the magnitude of the effect to be approximately a 0.65° F (0.36° C) increase per irradiation temperature decrease. Finally, the ASTM also proposed an analytical method in ASTM E900 [55] to predict the radiation-induced transition temperature shift of reactor pressure vessel materials showing a similar trend of low-temperature penalty.

In the comparative study, irradiation at 525° F (288° C), the transition temperature of the Oak Ridge National Laboratory method [48] has a 45% higher value compared with the NRC report [41]. The Oak Ridge National Laboratory method provides the most conservative values in the in-service temperature of reactor pressure vessel. Moreover, the effect of low irradiation temperature seems to have a considerable overestimation in other methods. The result of irradiated transition temperature at 150° F (66° C) is excessively increased while the 525° F (288° C) results are moderate value.

Fig. 2.6 shows that the Oak Ridge National Laboratory method (2007) develops the lowest gradual slope along the temperature compared with the method proposed by Fabry et al. (1996), Odette and Lucas (1986), NUREG/CR-6551 (1998) and ASTM E 900 (2015).

2.4.2 Yield Strength

2.4.2.1 Basic Method

Irradiation embrittlement increases the yield strength of the steel in the RPV supports. This phenomenon is called irradiation hardening. As shown in Equation (11), the yield strength at irradiated condition, σ_{ys} is the sum of the initial yield strength, $Inital\ \sigma_{ys}$ and the increase in yield strength by irradiation embrittlement, $\Delta\ \sigma_{ys}$.

$$\sigma_{ys} = Inital\ \sigma_{ys} + \Delta\ \sigma_{ys} \tag{11}$$

The initial yield strength is the yield strength of unirradiated steel which is taken from ASME Section II-D, for tabulated SA-508 steel yield strength at in-service temperature, 150° F (66° C), 300° F (149° C) and 350° F (177° C), respectively. As each part of the RPV supports has a different in-service temperature as listed in Table 2.1, each initial yield strength is slightly

different in a range of 45 ksi to 48 ksi. The increase of yield strength by the embrittlement, $\Delta\sigma_{ys}$ is calculated by using the extensive experimental program RADAMO calculation sheet of the ASTM E900 supplement [56], which is based on the SCK-CEN report [57]. The equation in this report was made using three radiation hardening mechanisms: copper-rich precipitates (CRP), matrix defects (MD) and phosphorus-rich precipitates (PRP) shown in the following Equations (12) to (16).

$$\Delta\,\sigma_{ys}(MPa) = MD + \sqrt{CRP^2 + PRP^2} \tag{12}$$

$$MD = \left[660\exp\left(-270\exp\left(\frac{-0.27}{k(T_i\ +273)}\right)\right) + Ni\left(6430 - 10.8(T_i\ +273)\right)\right] \times \sqrt{\left[1-\exp\left(0.008(f-f_0)\right)\right]\left[1-\exp\left(\left[1-\exp\left(-0.135(f-f_0)\right)\right]\right.\right.} \tag{13}$$

$$CRP = Cu_{sat}(1-\exp(-2.7(Cu-0.03)))\left[\frac{-1}{\log(0.05)}\log\left(\frac{\min(t,t_p)}{0.05\ t_p}\right)\right] \tag{14}$$

$$PRP = C_p(P-0.008) + \left[1-\exp\left(-P_T\ f\exp\left(-0.038(T_i+273)\right)\right)\right] \times\ \exp\left(-270\exp\left(\frac{-0.27}{K(T_i\ +273)}\right)\right) \tag{15}$$

$$t_p\ = \frac{10^{((2.12/k\cdot\ln(10)(T_i+273))-13.3)}}{1+200\cdot\emptyset/2\cdot 1.00E+10\cdot\exp(2.944/k(T_i+273))} \tag{16}$$

where,

k = 0.00008617 (Boltzmann constant)

f_0= 0.55 (Incubation fluence value)

C_p = 11,000 (Proportionality factor)

Cu_{sat} = 215 (Structural CRP hardening factor)

P_T = 88,466 (Degree of Irradiation Temperature effect on PRP rate)

P = 0.015 (Phosphorous weight percent, followed SA 508 [38])

Ni =1 (Nickel weight percent, followed SA 508 [38])

T_i = 66° C, 149° C and 177° C (150° F, 300° F and 350° F), respectively (Irradiation temperature)

f = Neutron fluence computed with each expected neutron fluence, refer to Table 2.2

$\emptyset$ = 1.14E+09 n/cm^2/s (Neutron flux, based on 55.8 effective full power years)

t_p = The time to reach CRP maximum hardening

2.4.2.2 Determination of Yield Strength

In Table 2.2, the yield strength results per the expected irradiation-temperature and the level of the neutron fluence are presented. The initial yield strength is 46.02 ksi (317 MPa) and the increase in yield strength is 12.85 ksi (89 MPa), as a mean value. As a result, the irradiated yield strength is calculated to be 58.87 ksi (406 MPa) on average. Thus, the yield strength may increase 28% due to the irradiation.

2.4.2.3 Yield Strength Increase Trend with Irradiation Level

The increase in yield strength was calculated per the SCK-CEN report [57] which is introduced in ASTM E900 supplement [56]. There were four increase in yield strength estimation equations available in literature for applying the RPV supports' metallurgical and irradiation values, Odette et al. [58], SCK-CEN report [57], Wechsler et al. [59] and Odette and Lucas [60]. But two of them, Odette et al. [58] and the SCK-CEN report [57] could be applied for comparison due to the lack of the metallurgical data. Finally, the SCK-CEN report was selected because it considers the low irradiation-temperature.

Wechsler et al. [59] presented the temperature variation equation applying strain-rate and tri-axiality corrections using the experimental data such as stress-strain test and impact test. Odette and Lucas [60] detailed the principles of yield stress increase in microstructure changes. These analytic approaches are to predict the stress with correction factors based on the experimental data in a certain range of temperature and irradiation which are not applicable in this study.

Odette et al. [58] proposed an empirical trend equation as shown in Equation (17) with a fractional decrease of the upper-shelf energy (USE). The USE is associated with the decreased impact energy in ductile failure and can be derived per its neutron fluence and copper weight percent from the NRC regulatory guide [41]. The decreased USE ratio was set as f_d , where the $f_d = \Delta USE/USE$.

$$f_d = 9 \times 10^{-4}\Delta\sigma_{ys} + 0.02\sqrt{\Delta\sigma_{ys} - 40}\,\Delta\sigma_{ys} \quad (\Delta\sigma_{ys} > 40\text{MPa}) \tag{17}$$

The result of Equation (17) is presented in Table 2.3. However, due to the lack of data in the USE graph of the regulatory guide, only the limited neutron fluence greater than 50% MDF, $1\text{x}10^{18}$ n/cm^2 were available to calculate. There is a considerable increase in yield stress of

approximately 12% between the initial unirradiated stage and 50% irradiated stage. However, it is noticeable that the increment per neutron fluence level is not considerable, within 0.4 MPa (0.06 ksi) per each neutron fluence level. Likewise discussed in the fracture toughness, the USE plot in the NRC regulatory guide [41] does not consider the low irradiation-temperature effect. The USE values are based on 550° F irradiation temperature. Therefore, these results derived from Odette et al. [58] were used for referencing the yield strength increase trend, not used for the RPV supports analysis.

Table 2.3 Calculated yield strength increase per analysis method

Fluence Level	Increased Yield Strength, ksi (MPa) [a]	
	Odette et al. (1985)	SCK-CEN [57]
Initial state	48.10 (331.6)	44.94 (309.9)
25%MDF [b]	-	58.87 (405.9)
50%MDF	54.12 (373.1)	58.88 (406.0)
75%MDF	54.18 (373.6)	58.88 (406.0)
100%MDF	54.23 (373.9)	58.88 (406.0)

[a.] The steel yield strength is based on the irradiation temperature, Odette et al case was based on 550° F (288° C), the SCK-CEN is average value of the 150° F (66° C) , 330° F(166° C) and 350° F (177° C).

[b.] The given USE value for calculating the increased yield strength in the NRC regulatory guide starts from 50% MDF.

Meanwhile, the ASTM E 900 provides a supplement [56] which was used for technical basis in assessing transition temperature shift by the embrittlement, with 4,438 data records from the surveillance program and research test data. This supplement presents the irradiation hardening equations of the SCK-CEN report [57]. Parameters for this assessment are readily available such as material weight percent, neutron flux and the irradiation temperature is also considered.

The yield strength increase trend with Odette et al. [58] and the SCK-CEN report, are presented in Table 2.3. The irradiation hardening peak was achieved in the first phase, from the unirradiated condition to the 25% maximum design fluence. After the first irradiation stage, the increment per each fluence level is relatively small. This fast yield strength increase of the low irradiation temperature is also presumed in Chaouadi and Gérard [61], as well.

2.4.3 Linear Elastic Stress Analysis using Finite Element Method

2.4.3.1 Basic Method

The stress analysis is required to quantify the stress intensity and the plasticity effects of the postulated crack. It is also required to define the stress concentration region so this study examines the postulated crack which gives the most conservative analysis. The elastic stress analysis was carried out on a perfect structure without any crack using the finite element software ABAQUS [47].

2.4.3.2 Modeling

The RPV supports geometry was built in a 3D solid three-dimensional structural model referencing the APR 1400 design control documents [16]. The geometry comprises all of the main structural parts of the support which are the flange plate, support column, and base plate with shear keys attached. The schematic models and assembly are given in Fig. 2.2. This model has a fixed boundary condition at the base plate as the shear key is embedded in the base concrete. The material property of this model is considered to be linear elastic with applying the elastic modulus and the Poisson's ratio.

The elastic modulus was taken from the ASME Section II-D [45], following SA 508 grade 3 class 1 steel [38] elastic modulus per the in-service temperature. The applied elastic modulus per in-service temperature and the Poisson's ratio are listed in Table 2.2. The model was meshed using three dimensional 20 noded quadratic structural solid element, C3D20. This mesh is shown in Fig. 2.7 with approximately 763,000 nodes and 176,000 solid elements. A convergence analysis to evaluate the mesh size was carried out in this study. The model had meshed with a seed distance of 0.5 in. (12.7 mm) to 2 in. (50 mm) to verify the stress convergence. The result of the mesh study showed convergence within 0.1% in stress. Thus, finite elements with about 1 in. (25.4 mm) mesh size were applied. Modeling the fillets between the flange plate to column were not possible because it produces some distorted elements.

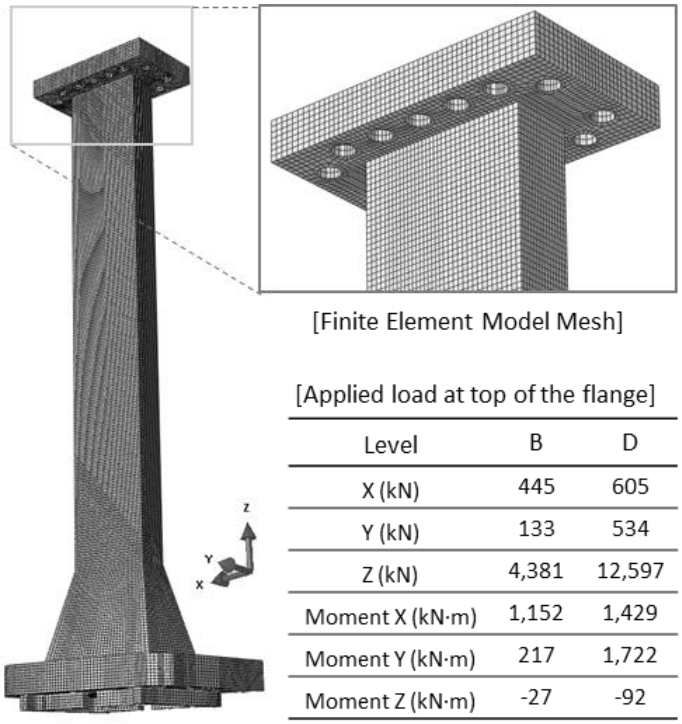

[Applied load at top of the flange]

Level	B	D
X (kN)	445	605
Y (kN)	133	534
Z (kN)	4,381	12,597
Moment X (kN·m)	1,152	1,429
Moment Y (kN·m)	217	1,722
Moment Z (kN·m)	-27	-92

Fig. 2.7 Reactor vessel support finite element 3D Model, detail on mesh and the load applied

2.4.3.3 Load Cases

The two load cases, the operational level load - Level B and the extreme level load - Level D were applied in this study. The loads are shown in Fig. 2.7 where x direction is horizontal along the short direction of support, y direction is horizontal along the long direction of support and z direction is the gravity direction. The loads were uniformly distributed along the flange plate, base plate and shear key.

Both load cases are included in the thermal load. The thermal load is classified as secondary stress according to the ASME Section III-1 and API 579 and it generates the secondary stress intensity factor, K_I^{SR}. The thermal stress in this study will offset the primary membrane stress because the thermal stress is acting in the direction of contraction while the primary membrane stress is in tension. The separately applied thermal stress as a secondary stress results in underestimated stress intensity by adding up the membrane stress in the opposite direction with decreased reference load ratio. This study treated the stresses as primary stress keeping the effect of the thermal stress though the reference load ratio is increased about 0.1 to be more conservative as per section 9 of API 579.

2.4.3.4 Stress Singularity

The stress results from the finite element analysis are depicted in Fig. 2.8 for Level D load case and Fig. 2.9 for Level B load case. These stress diagrams are expressed in 75% averaged von Mises equivalent stress showing the maximum stress region. The locations of the concentrated stress regions were generated on the RPV support column part: (1) at the top corner of the column support under the bottom of the flange part at the front side and (2) the bottom corner of the column support where the section changes to a trapezoidal-shaped section at the back side.

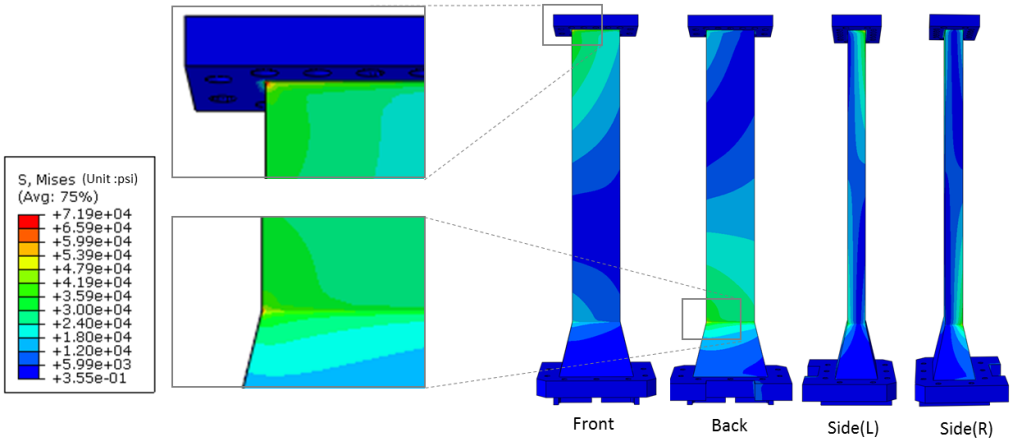

Fig. 2.8. Concentrated stress region from the stress analysis result in level D load case (von Mises, 75% averaged)

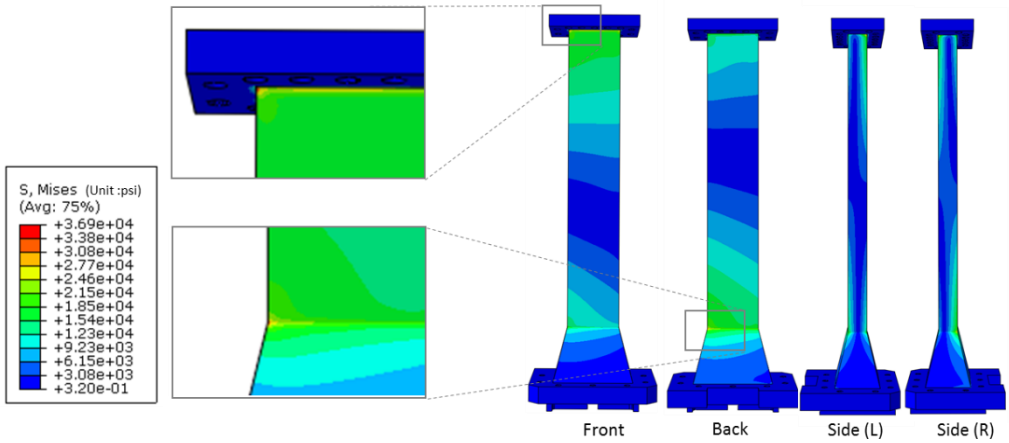

Fig. 2.9 Concentrated stress region from the stress analysis result in level B load case (von Mises, 75% averaged)

It is usual that the exaggerated stress is obtained at the sharp corners of the solid element-type FEM model. According to the stress categories in ASME BPVC Section VIII-2 [62], the possible causes are structural discontinuities and peak stress by sharp edge. The stress generated

by the gross structural discontinuities is classified as membrane stress and the local discontinuities are covered by the peak stress. Fig. 2.10 shows the linearized stress distribution of the RPV support column in vertical direction providing the membrane stress, bending stress and the peak stress. The maximum stress was generated where the section changes particularly at the corners. However, as the meshes are refined, these membrane stress and peak stress values tend toward infinite value and stress divergence meaning that those singularities by the stress linearization were not removed.

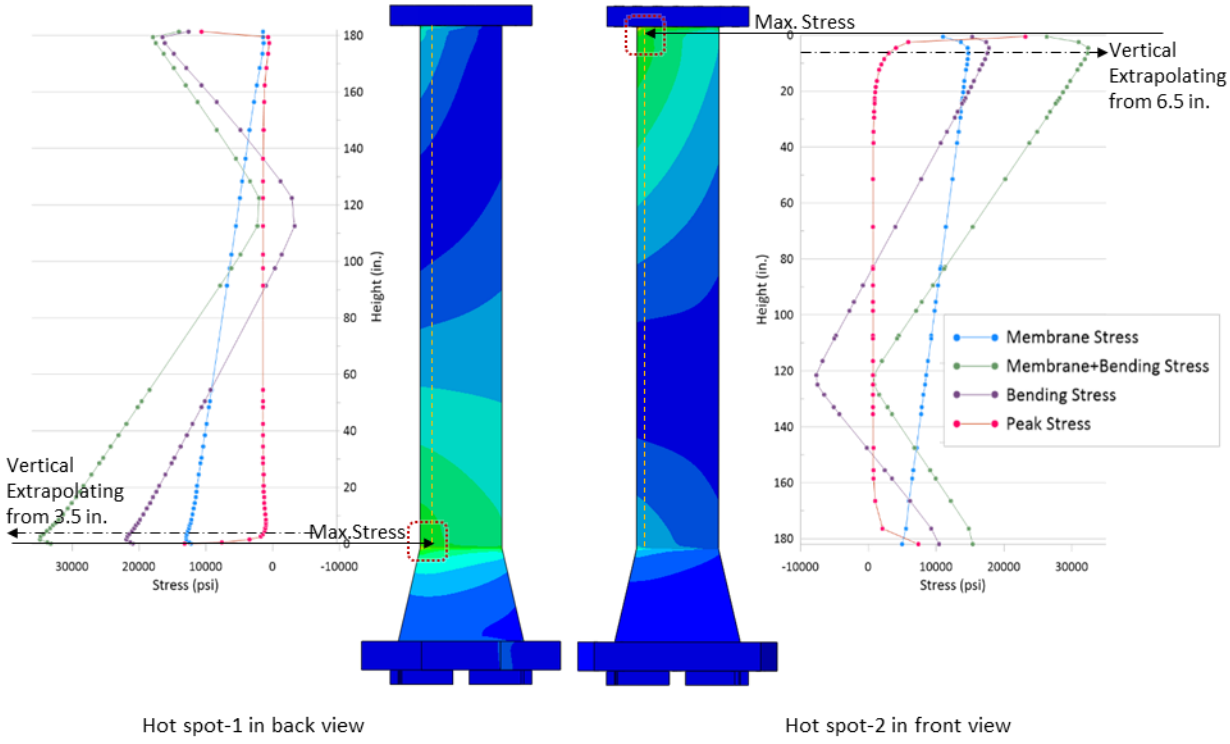

Fig. 2.10. The stress distribution along the vertical direction through the structural hot-spots

Niemi et al. [63] named this unrealistic stress singularity region as the structural ‘hot-spot’ and proposed several modifying methodologies to filter out unrealistic peak stress and keep the structural stress in terms of membrane and bending stresses. One of the methods is the stress extrapolation. However, this method was not applicable to this study due to the relatively high thickness of the component. The structural hot-spot is located on the support column which is 11 in. (279.4 mm) thickness. The stress gauge points those are used in estimating the hot-spot stress are quite far from the hot-spot. This results in a higher value compared to the original value. Compared to the stress extrapolation example in Niemi et al. [63], the 11 in. (279.4 mm) thickness is considerably thick.

Kalnins [64] proposed another stress extrapolation method for the values of the equivalent stress calculated by the stress linearization approach particularly in the stress singularities. In the stress singularity, the exaggerated stress component would lead to errors in computing the equivalent stress. After evaluating the validity of the stress classification lines, using recommendations of Hollinger and Hechmer [65] and the ASME Section VIII-2, the valid point is found and the each stress components values will be extrapolated from the valid point. The valid points were found where the stress does not converge with refined mesh and the normal stress varies monotonically.

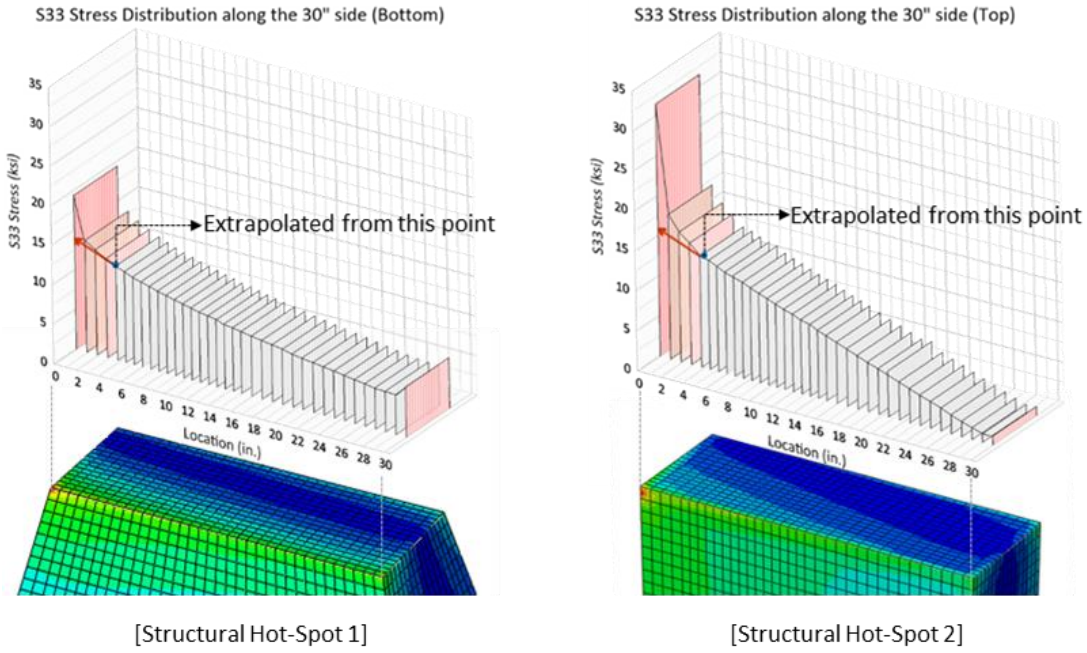

[Structural Hot-Spot 1] [Structural Hot-Spot 2]

Fig. 2.11 The averaged normal stress (S33) extrapolating near the structural hot-spots

In Fig. 2.11, the normal stress distributions on normal stress classification lines of the hot-spot 2, under the level D load case were plotted along the horizontal section. The valid point in the horizontal direction was determined to be 3.74 in.(95.0 mm) from the singularity and in the vertical direction valid point starts from 2.50 in.(63.5 mm) from the top. To get a more conservative result, the vertical point was adjusted to 6.50 in. (165 mm), as illustrated in Fig. 2.10. Using the same methods, the hot spot-1 valid point starts at 3.43 in. (87.1 mm) in the horizontal direction from the corner and 3.50 in. (88.9 mm) level from the corner. The valid stress linearization points are in Table 2.4 and the stress result from the stress linearization and extrapolation of the structural hot-spots are given in Table 2.5.

Table 2.4 The valid stress linearization point measured from the hot-spots

Load Level / Location		Direction from the corner	
		Horizontal	Vertical
Level B	Hot-spot1	2.57 in. (65.3 mm)	2.00 in. (50.8 mm)
	Hot-spot2	1.88 in. (47.8 mm)	2.50 in. (63.5 mm)
Level D	Hot-spot1	3.43 in. (87.1 mm)	3.50 in. (88.9 mm)
	Hot-spot2	3.74 in. (95.0 mm)	6.50 in. (165 mm)

Table 2.5 The stress applied to the FAD method

Stress		Location	
		Hot-spot1	Hot-spot2
Level B	Membrane	5.468 ksi (37.70 MPa)	4.634 ksi (31.95 MPa)
	Bending	15.86 ksi (109.4 MPa)	16.63 ksi (114.7 MPa)
Level D	Membrane	13.42 ksi (92.53 MPa)	17.03 ksi (117.4 MPa)
	Bending	24.08 ksi (166.0 MPa)	19.41 ksi (133.8 MPa)

2.4.4 Postulating Flaws

This study postulated the flaw length from 0.1 in. (2.54 mm) and up to the length which the failure assessment fails with increments of 0.01 in. (0.25 mm). The depth of the flaw were assumed to be 1/6, 1/3, 1/2, 2/3 and 5/6 of the given flaw length. The crack locations are at the corner of the structural hot-spots.

The RPV supports may contain very small sized flaws that original fabrication allows because the steel forging is subject to massive heat through the metallurgical phase. The preservice flaw may be a possible cause that can be propagated into significant flaws considering the recent issue of the carbon macro-segregation issue in the vessel [66]. The 0.19 in. (4.83 mm) length is to review the surface type preservice flaw limitation and the 0.33 in. (8.38 mm) length crack is for embedded type preservice flaw limitation following the SA 508 nondestructive inspection requirements. Furthermore, during the in-service inspection, the allowable limits are derived from ASME Section XI.

2.4.5 Partial Safety Factor

To consider the reliability of the failure assessment, the uncertainties of the independent parameters are included in the failure assessment procedure. Each uncertainty source is taken into account as a partial safety factor, PSF. The parameters applied by this PSF are stresses, flaw dimensions, and the fracture toughness. However, in the 2016 edition of API 579, it allows to determine the PSF value in the probabilistic approach and does not provide a specific number. This study followed the PSF values of the 2007 edition of the API 579 [67] and applied to the stress, fracture toughness and crack depth. The PSF for fracture toughness after irradiation were taken as 1.0 because the lower-bound fracture toughness was used. The calculated fracture toughness for each intermediate neutron level, plotted in Fig. 2.12 shows that the fracture toughness converged to the lower bound. According to the U.S. NRC seismic probabilistic risk assessment guide [68], the high confidence of low probability of failure is defined as 5% which gives a conservative estimation considering uncertainty and randomness variables. In accordance with this 5% probability of failure, this study chose the highest probability among the category given in the API 579 2007 edition which gives PSF of stress as 1.2 in initial unirradiated condition and 1.25 after irradiated condition. The crack depth PSF was applied after irradiation: 1.08 for the shallower than 0.2 in. (5 mm) depth and 1.1 for the deeper crack sizes.

2.4.6 Toughness Ratio and Load Ratio for the FAD Approach

To plot evaluation points for each crack in the FAD, the stress intensity and the reference stress were determined at each crack. The stress intensity and reference stress solution for the RPV supports, a plate with bending and membrane stress case were applied from the solution table of API 579. For the surface crack, stress intensity K_I^P was computed by the KPSCE1 solution and the reference stress, L_r^P were given by the RPSCE1 solution for the plates with a semi-elliptical shaped surface crack using through-wall membrane and bending stress. For the embedded crack, stress intensity and the reference stress were derived from KPECE1 and RPECE1, respectively which are for the plates with elliptical shaped embedded crack, using through-wall membrane and bending stress. The assessments were done in each type of cracks, load cases and the irradiation neutron fluence level, from the initial state, 5% MDF to the 100% MDF state were applied.

2.5 Neutron Irradiation Effect on Failure Assessment Parameters

2.5.1 Effect of Fracture Toughness

The decrease of the fracture toughness of the RPV support varies in an exponential trend as shown in Fig. 2.12. The fracture toughness per irradiation levels are marked on the plot of the Equation (3) from ASME Section XI showing the fracture toughness (K_{IC}) and the temperature difference between the assessment temperature (T) and the adjusted reference temperature (ART). The initial fracture toughness, 84 ksi$\cdot\sqrt{in.}$ (92 MPa$\cdot\sqrt{m}$) is the minimum value required by the design documents for the SA 508 material. As the ART increases by neutron irradiation, the fracture toughness substantially decreases to the baseline. From the point where ART exceeds the assessment temperature (T), the fracture toughness is close to the lower bound and it is practically indistinguishable between the irradiation levels. Furthermore, in Fig. 2.13, the effect of the neutron irradiation has been reviewed at each of the various neutron fluence levels showing how the fracture toughness and the yield strength trends change with respect to the neutron fluence level.

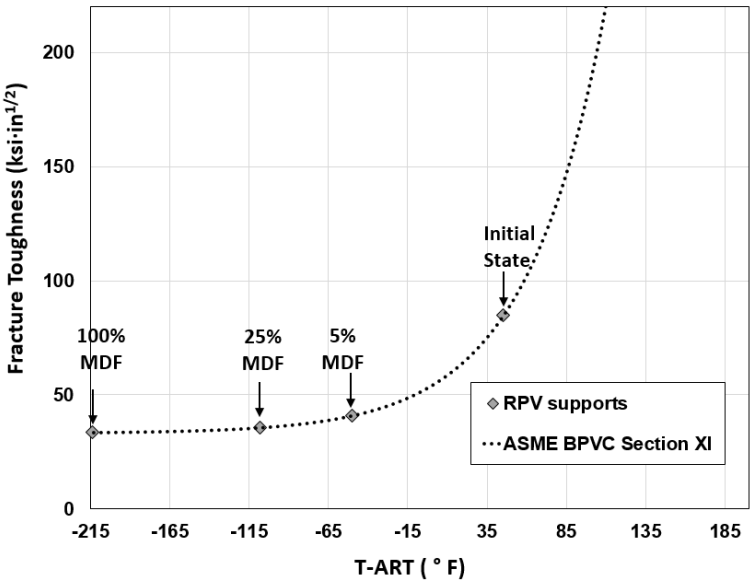

Fig. 2.12 Exponential curve of equation and analysis results plot for the fracture toughness and temperature transition (Added results on the ASME BPVC SEC XI, Figure G-2210-1)

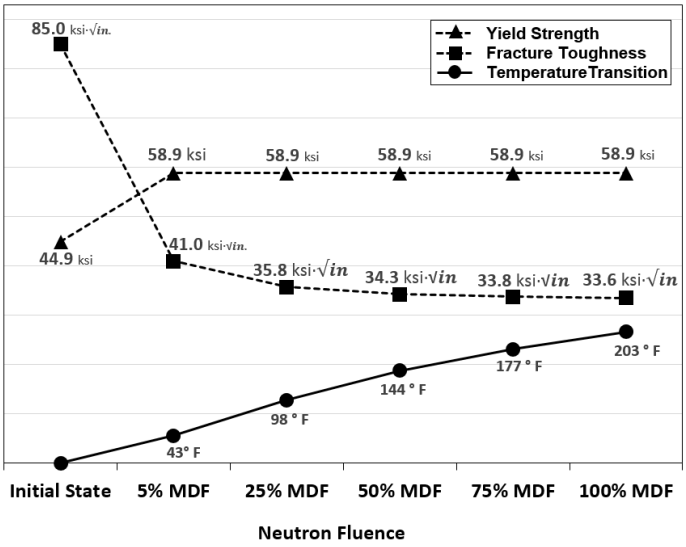

Fig. 2.13 Fracture toughness and yield strength variation across the accumulated fluence and the TTS

It is notable that the fracture toughness and the yield strength vary significantly only during the first irradiation phase while the transition temperature shows gradual increase corresponding to the neutron fluence accumulation. The two trends of the yield strength and fracture toughness are similar to the trend of the neutron fluence level. It corresponds to the irradiation sequences reported in the Oak Ridge National Laboratory report (ORNL/TM-2006/530, 2007). The metallurgical change from the irradiation generates the precipitates. The precipitates affect the irradiation hardening and also increase in the yield strength. Thus, the yield strength and the fracture toughness trends are similar. Recently, Margolin et al.[69] investigated radiation embrittlement of support structure materials for the Water-Water Energetic Reactor(WWER) with experimental and analytical methods. Given that the neutron fluence, type of material and the irradiation temperature are different from this APR 1400 model, the trend of the results compared, the low irradiation temperature conditions result in considerable embrittlement and increased yield strength, likewise the result from this study.

2.5.2 Effect of Yield Strength

The yield strength has increased from 45 ksi (310 MPa) to 60 ksi (414 MPa) from the first irradiation phase in the same trend as the fracture toughness does, as shown in the Fig. 2.13. The reason for the steep increase in yield strength can be explained by the RADAMO calculation sheet of the ASTM E900 supplement [56]. The hardening is generally admitted that it results from the

precipitation and matrix hardening and they are independent in results [61]. The radiation precipitations are the copper-rich precipitates (CRP), and phosphorus-rich precipitates (PRP). The matrix hardening is usually referred to as the matrix defects (MD) which represent the defect clusters. These three contributions in the increase of the yield strength are described in Fig. 2.14, (a) for the RPV support and (b) for the RPV. The CRP, PRP and MD effects are calculated by Equations (12) to (16) with applying each parameter such as the neutron fluence, irradiation temperature and the flux. The graph in Fig. 2.14 (a) shows that the three contributions go into the constant values before the 5% MDF reaches. This plot can be explained by the minutes of the ASTM E900 supplement [56].

(a)

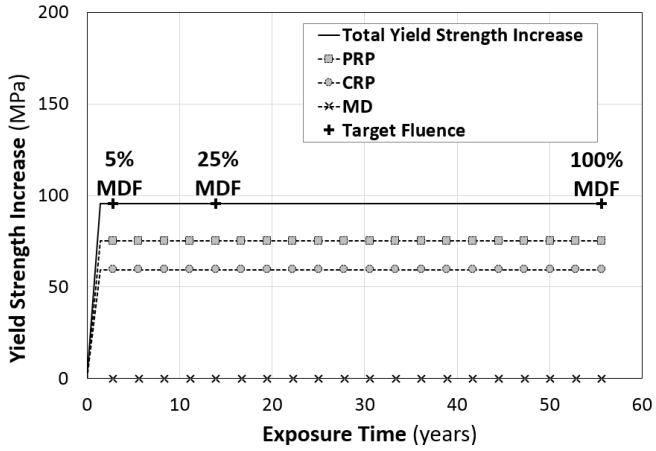

(b)

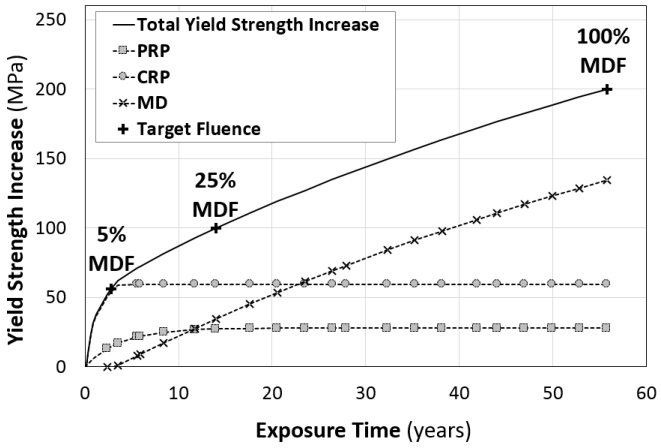

Fig. 2.14 Yield strength increase and the exposure time, Reactor Pressure Vessel Support and Reactor Pressure Vessel

(a) Reactor Vessel Support (f=2E+18 n/cm^2, Ti=150° F), (b) Reactor Pressure Vessel (f=9.5E+19 n/ cm^2, Ti=550° F)

Among the three contributions, the matrix defects (MD) take effect when the neutron fluence is greater than the incubation fluence, 5.5E+10^{18} n/cm^2. As the neutron fluence of RVS support is 2E+10^{18} n/cm^2, below the incubation fluence, the MD hardening does not influence showing 0 in the graph Fig. 2.14 (a). Meanwhile, the CRP and PRP have increased to the highest value before the 5% MDF level. The time to peak in CRP hardening, t_p is calculated as 1.73E-02 years by the Equation (16). Considering that the time to the 5% MDF level takes about 3 years, the CRP reached to peak before the 5% MDF level. As shown in Equation (16), the time to reach CRP maximum hardening, t_p depends on the neutron flux and irradiation temperature. These two factors have affected the fast CRP peak. In the same manner, the PRP hardening effect accelerates as the irradiation temperature decreases according to Equation (15). Therefore, the RPV support experiences peak irradiation hardening in the first irradiation phase.

Meanwhile, the RPV irradiation hardening shows the gradual increase in yield strength as plotted in Fig. 2.14 (b). The CRP and PRP reach the almost maximum value before the 5% MDF level like the trends of the RPV support. However, the MD plot increases gently in effect of the MD hardening with the high neutron fluence. Through the influence of the MD, the overall reactor pressure vessel irradiation hardening graph trend shows a gradual increase. From the plots of the hardening factor in Fig. 2.14 (a), the considerable increase of the RPV supports yield strength in the first MDF phase can be explained.

2.6 Failure Assessment of Irradiated Long Column Type RPV Support

2.6.1 Localized Assessment in the RPV Support

Taking into account the results of the fracture toughness estimation and the stresss analysis, the column suppport part was selected to be the most vulnerable part in the long-column type support. The column support part has the lowest irradiation temperature, 150° F (66° C), which leads to larger fracture toughness decrease compared with other parts. From the stress results of the finite element analysis, the structural hot-spots were generated at the top and bottom corner of the column support. Therefore, the cracks were postulated in the two structural hot-spots in the column support.

2.6.2 The Effect of Neutron Fluence in FAD Assessment

By increasing the level of neutron irradiation in the selected intermediate phases, the behavior of irradiated RPV supports with 5/6 depth to length ratio surface cracks have been assessed with failure assessment diagram as in Fig. 2.15 and Fig. 2.16 which are hot-spot 1 and hot-spot 2, respectively. This assessment was carried out at surface type cracks under the Level D load condition. As the fracture toughness and the yield strength are similar from 25% MDF level, the considered irradiation levels are 5% MDF, 25% MDF and the 100% MDF with respect to the color that represents the irradiation level.

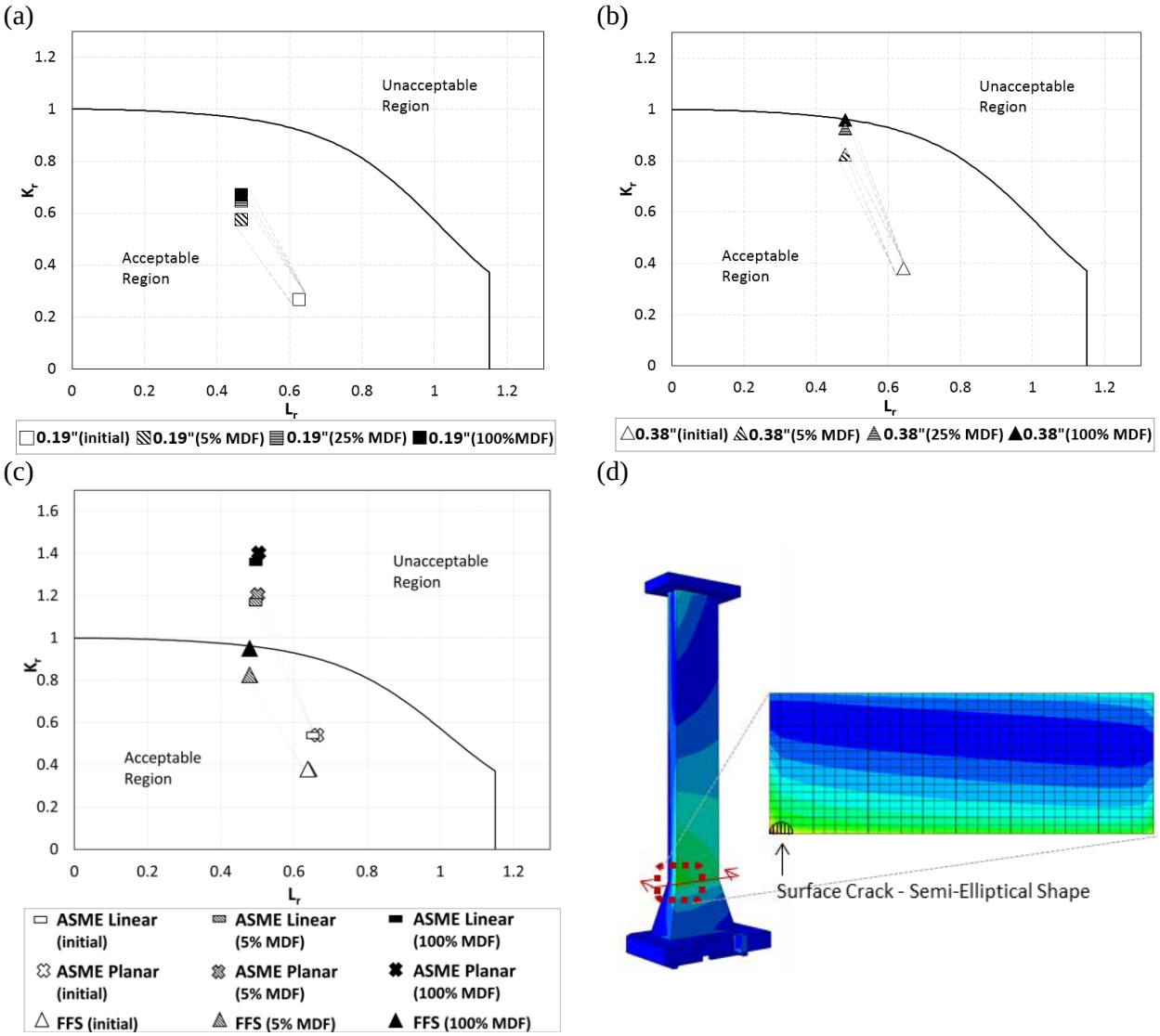

Fig. 2.15 Failure assessment of hot-spot 1 (Level D load case, surface crack)

(a) Maximum pre-service allowable crack size of 0.19" length from un-irradiated to the 100% MDF, (b) Maximum permissible crack size of 0.38" length from un-irradiated to the 100% MDF (c) Maximum in-service allowable crack size in each method from un-irradiated to the 100% MDF (d) Surface crack location

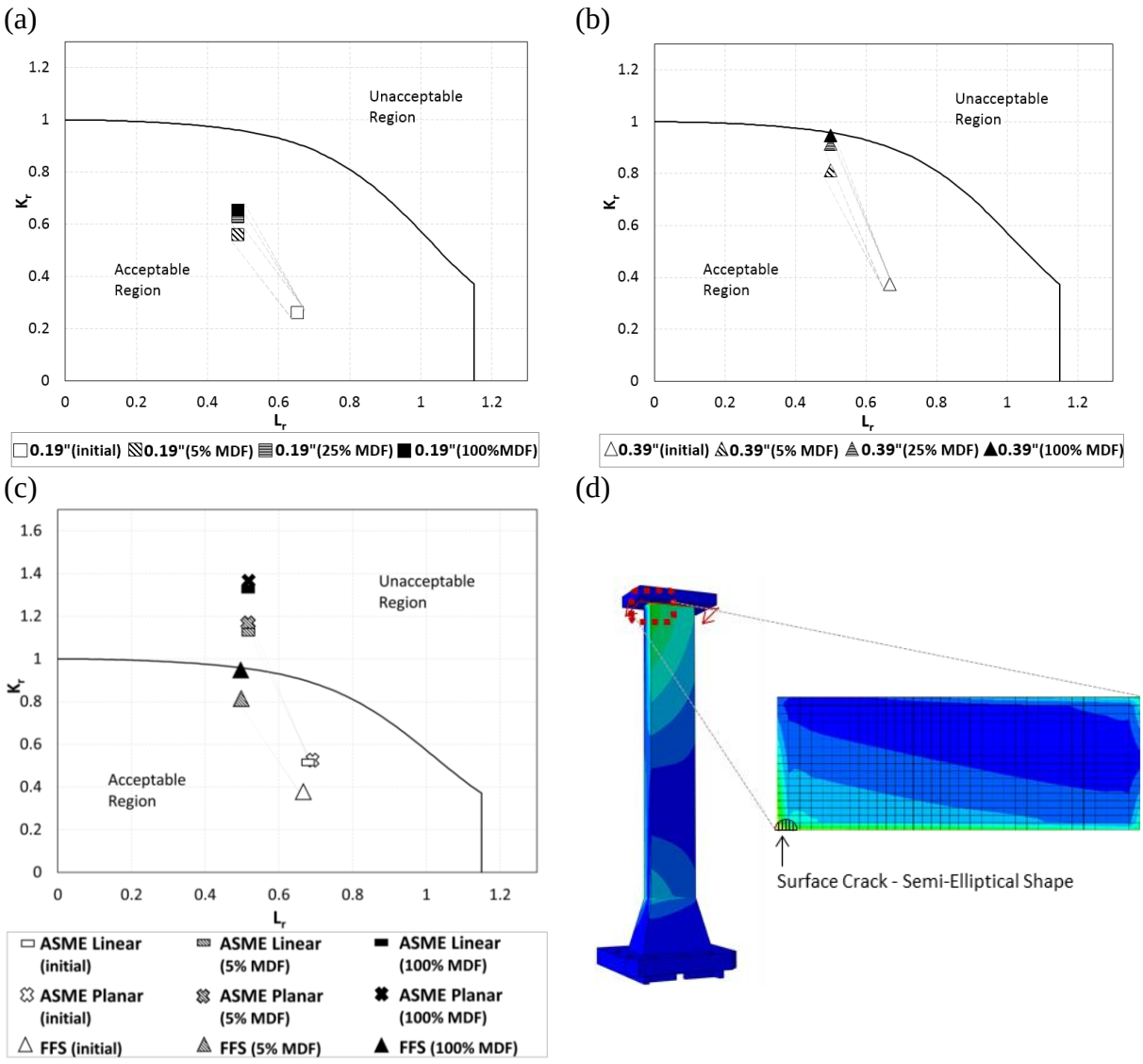

Fig. 2.16 Failure assessment of hot-spot 2 (Level D load case, surface crack)

(a) Maximum pre-service allowable crack size of 0.19" length from un-irradiated to the 100% MDF, (b) Maximum permissible crack size of 0.39" length from un-irradiated to the 100% MDF, (c) Maximum in-service allowable crack size in each method from un-irradiated to the 100% MDF, (d) Surface crack location

Fig. 2.15 (a) shows the assessment points of the maximum pre-service allowable surface crack size in preservice, 0.19 in. (4.83 mm) length in variation of irradiation levels. As the neutron fluence increases, the assessment points tend to move upward because of the increased stress intensity by the decreased fracture toughness and the gained yield strength through the neutron irradiation pushed the assessment points to the left side, lowering the load ratio. However, they are

still in the acceptable region with sufficient margin in stress intensity of 0.67 while the critical stress intensity in this point is estimated as 0.96. In Fig. 2.15 (b), larger size of surface cracks were postulated to estimate the maximum permissible crack sizes in the hot-spot 1 under the level D load, 100% neutron irradiated condition. Based on the deepest crack of 5/6 depth to length ratio, the maximum permissible crack was calculated to have 0.38 in. (9.65 mm). length. The results of the hot-spot 1 are similar to the hot-spot 2, see Fig. 2.15.

From the (a) and (b) plot of Fig. 2.15 and Fig. 2.16, the assessment points plotted in the left part in the failure assessment diagram tell us this RPV supports appeared to be critical to a brittle fracture rather than a plastic collapse. Comparing the initial assessment points with the 100% MDF assessment points, the increased yield strength lowered the load ratio by about 75% on average, and the decreased fracture toughness raised the toughness ratio by about 250% on average. These numbers indicate to us that the effect of the fracture toughness is considerable compared to the yield strength in this RPV supports structural integrity.

The estimated maximum permissible crack derived by the FAD method was compared to the other in-service allowable limits of ASME Section XI (ASME, 2017b), plotted at (c) of Fig. 2.15 and Fig. 2.16. The allowble limits per each references, types and the phases are given in Table 2.6.

Table 2.6 Maximum allowable crack lengths for the RPV support in this study

Method	Types of the crack	
	Surface	Embedded
Pre-service	0.19 in. (4.83 mm)	0.33 in.(8.38 mm)
ASME Linear [a]	1.10 in. (27.9 mm)	1.67 in (42.4 mm)
ASME Planar [a]	1.15 in. (29.2 mm)	1.59 in. (40.4 mm)
FAD Method [b]	0.38 in. (9.65 mm)	1.70 in. (43.2 mm)

[a.] Crack depth to length ratio of 1/2 is used

[b.] Crack depth to length ratio of 5/6 is used

The in-service allowable limit of the crack size is determined by the inspection methods in accordance with the ASME Section XI. Detecting the flaws by surface using the magnetic particle test, liquid penetrant test or volumetric examination by radiagraphic examination will detect flaws

providing the length dimension. The linear surface crack allowable in-service limit from the ASME Section XI is 1.1 in. (28 mm) considering 10% of the thickness. When it employed ultrasonic examination, the crack is classified as a planar crack with two dimensions, length and depth. The allowable in-service limit for a planar crack is drawn with depth to thickness. The maximum in-service allowable planar surface crack is 1.15 in. (29.2 mm) with 1/2 depth to length ratio. These maximum in-service allowable cracks from ASME Section XI as well as the maximum allowable crack determined by FAD approach are plotted together with variation of the irradiation level in (c) of Fig. 2.15 and Fig. 2.16. Before it gets irradiated, all of the allowable cracks remained in acceptable region. After irradiation begins, except for the maximum crack estimated by FAD method, the maximum in-service allowable cracks from ASME Section XI were plotted in the unacceptable region. Unlike the results of the pre-service crack assessment values which are all in acceptable region even in 100% MDF irradiation (see the plot (a) of Fig. 2.15 and Fig. 2.16), the in-service allowable crack limits satisfies only in the unirradiated state according to this FAD assessments.

2.6.3 The Effect of Crack Type in FAD Assessment

The embedded crack (see, Fig. 2.17) is assessed to have lesser stress intensity and less refreference stress than the surface crack has. Fig. 2.16 shows the assessment results of those which are embedded behind the 3 in. (76.2 mm) from the surface in hot-spot 1, experienced level D load and exposed to the irradiation condition. Similar to the surface crack assessment results, the maximum allowable crack size in preservice remained in the acceptable region at 100% MDF neutron fluence level and mostly remain near even though the neutron irradiation increases. The permissible crack of an embedded crack is found to be 1.7 in. (43 mm) length with 5/6 depth, while the permissible embeded crack size by ASME Section XI limits have the depth to length ratio as 1/2. The rate of change across the irradiation dose is identical to the surface crack showed. As the irradiation progresses, the toughness ratio increased by 258% and the load ratio decreased by 74% on average.

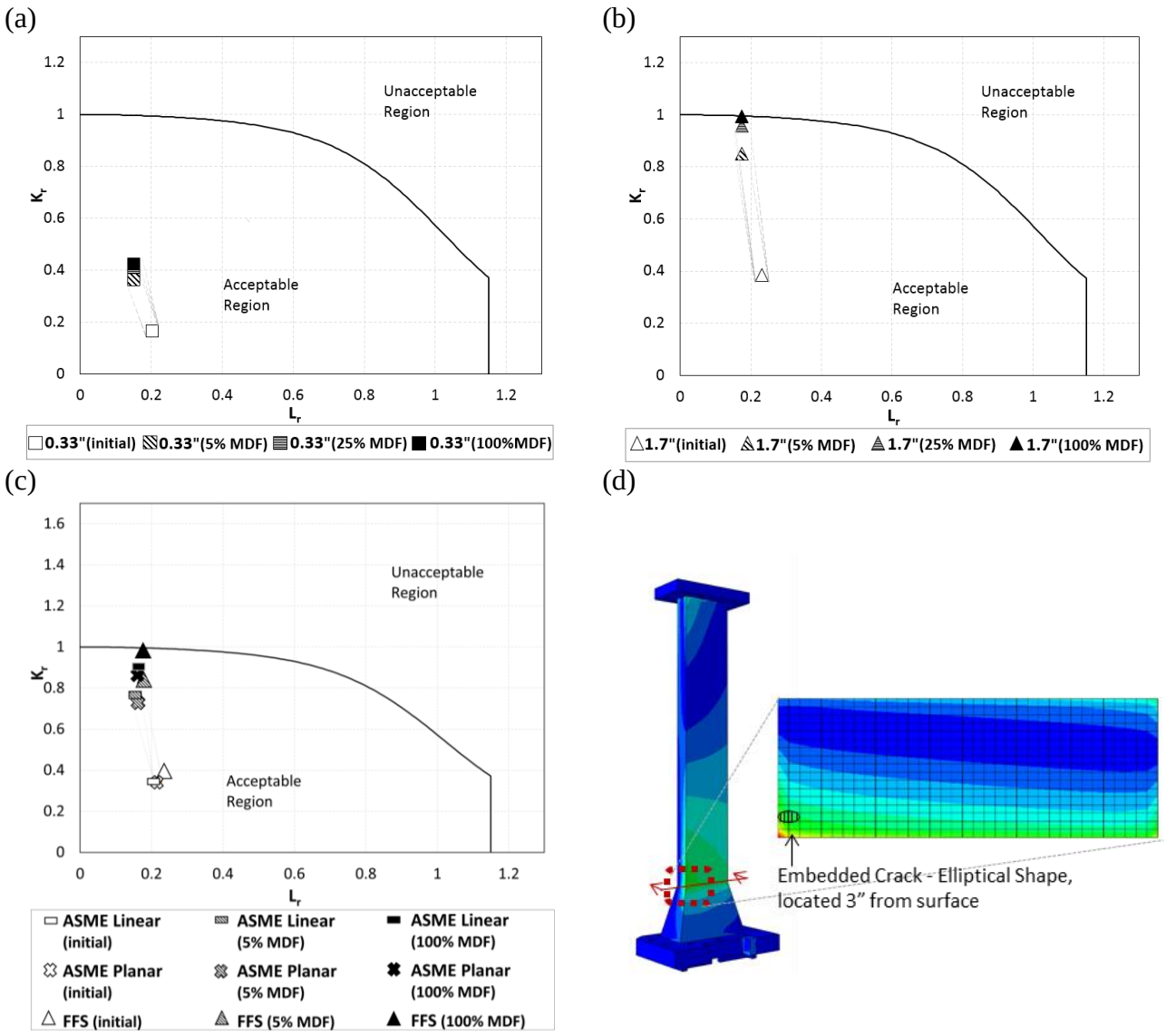

Fig. 2.17 Failure assessment of hot-spot 1 (Level D load case, embedded crack)

(a) Maximum pre-service allowable crack size-0.33" length from un-irradiated to the 100% MDF, (b) Maximum permissible crack size of 1.7" length from un-irradiated to the 100% MDF, (c) Maximum in-service allowable crack size in each method from un-irradiated to the 100% MDF, (d) Embedded crack (3" from the back surface)

However, the difference is that the embedded crack stress intensity is quite lower than the surface crack with comparison plot of maximum allowable crack sizes in Fig. 2.16, (c). All of the maximum allowable limits, ASME linear or ASME planar and the maximum permissible crack size determined by the FAD method remains in the acceptable region. The in-service allowable limits, whether they are fully irradiated or not, provide acceptable values in the FAD approach.

However, the reason that the embedded crack has relatively low stress intensity is characterized by the interaction of the crack location and the stress distribution. Because the stress gradually increases from opposite surface to the front surface when the surface crack was assessed by FAD, the crack on the surface results are relatively unfavorable.

2.6.4 The Effect of Crack Depth to Ratio in FAD Assessment

The postulated crack with different depth to length ratios with stress intensity were plotted in Fig. 2.18. The cracks were assumed to be in structural hot-spot 1 after level D loads are applied under maximum 100% irradiated condition.

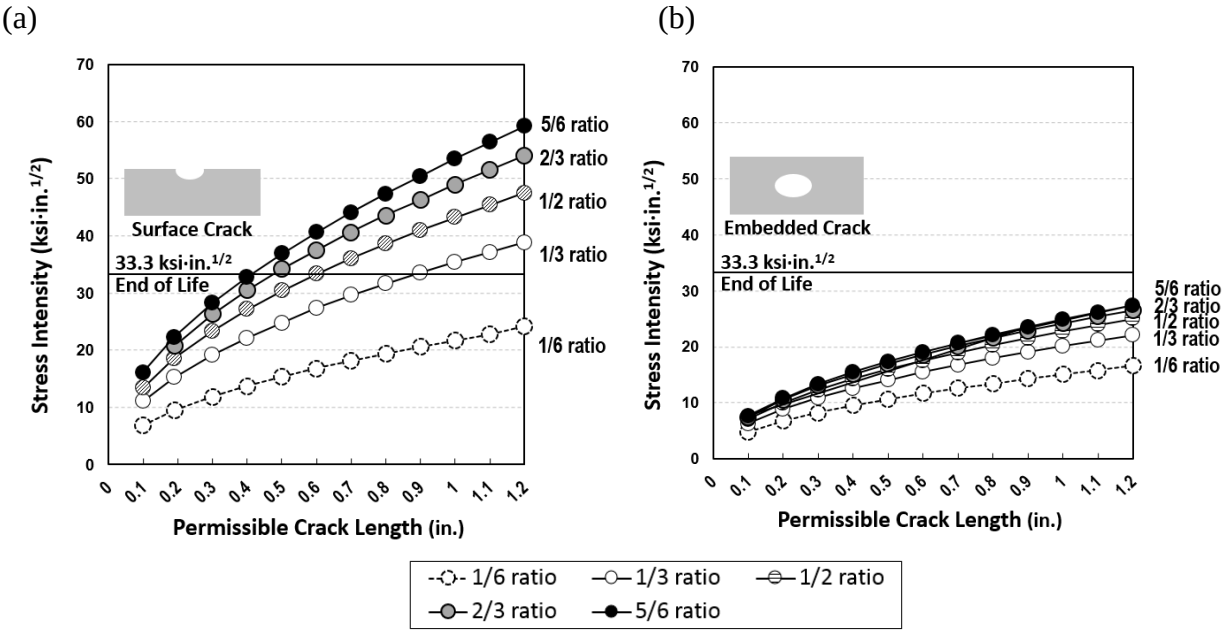

Fig. 2.18 Permissible crack length per aspect depth to length ratio under fracture toughness in 100% irradiated condition, level D load

(a) Permissible surface crack at hot- spot 1, (b) Permissible embedded crack at s hot-spot 1

With respect to the depth to length ratio of the crack, as the crack developed in deeper, the stress intensity increases. As the surface crack detection may have errors in checking the depth, even though the shallow crack (such ase 1/6, 1/3 ratio) allows to about 1 in. (25mm) length crack, the allowable crack was determined by the 5/6 depth to length ratio cracks. This plot also shows the difference between the types of the cracks that the stress intensity values do not have significant difference in embedded crack. Therefore, in the crack inspection during the operation, it is conservative to make the assumption of deep depth to length ratio crack particularly in the surface inspection, when the depth measurement is not applicable.

2.6.5 The Effect of Load Increase Compared in FAD Assessment

The effect of the increase of the load level from B to D is plotted in Fig. 2.19 corresponding to the type of crack and the irradiation effect. The assessment cracks are the maximum preservice allowable size crack in each type of the crack. Along the lines from level B to level D, both the reference stress and stress intensity increases and trajectories were drawn following the slope from level B and D to the FAD envelope given the assumption that the level D load is dominated by the seismic load so the load will be increased proportionally.

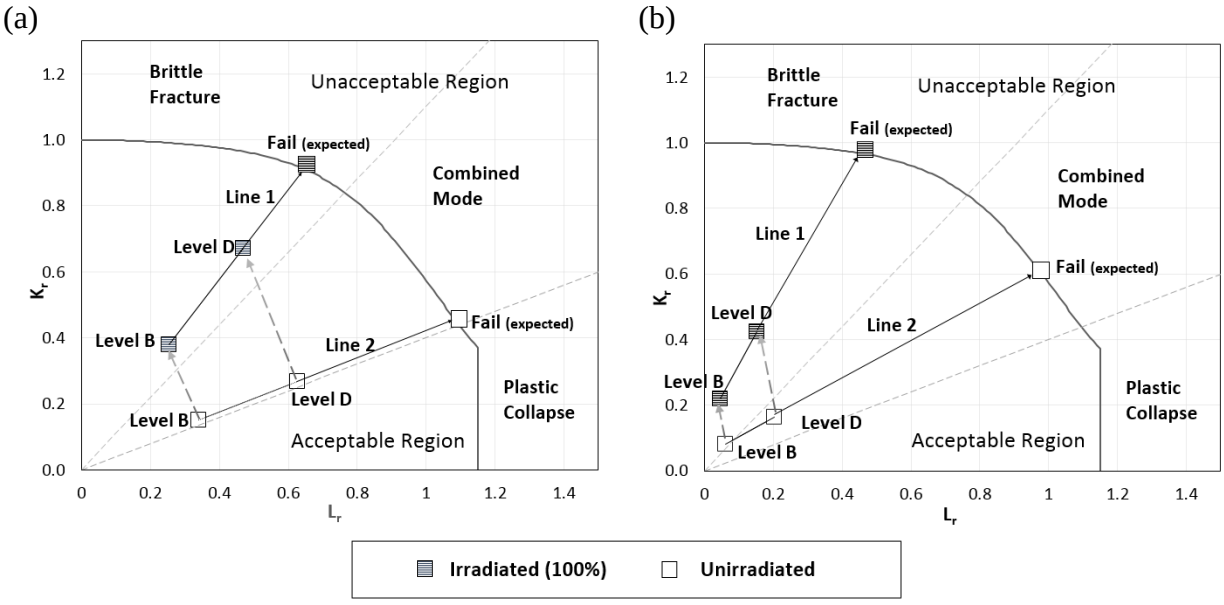

Fig. 2.19 Failure assessment respect to the level of load and the level of irradiation
(a) Surface crack, (b) Embedded crack

The slope represents the toughness ratio to the load ratio and tells us the dominant failure mode whether the failure is brittle fracture or plastic collapse. For the unirradiated assesment points, as the load increases the potential to have plastic collapse rather than brittle fracture is dominant. Comparing the unirradiated assessment points and the 100% MDF assessment points shown in Fig. 2.19 (a) surface crack, under the event of the load increases, the slope of line 1 of the irradiated assessment points is 1.4, while the slope of line 2 of unirradiated assessment points is 0.4. As the irradiated level D assessment points are closer to the FAD envelope in load ratio direction, the effect of the irradiation on FAD assessment under the increased loading condition, helps to move effectively to the failure point compared to the unirradiated ones in the furthur load increase event. The rate of the load increase in the assesment points were repeated in Fig. 2.19 (b) for embedded crack and the results are similar.

In comparison to the effects of the irradiation and the load increase effect, as shown in Fig. 2.15 and Fig. 2.16, the direction from the unirradiated point to the irradiated point is toward left upward in immediate variation. In this study, since the fracture toughness dropped to the lower bound and the irradiated assessment point moved to the FAD failure limit efficiently in load increase condition, so there seems to be high probability that the failure mode tends to follow the slope of line 1. However, the fracture toughness has a lower bound limit as shown in Fig. 2.12, the failure risk of irradiation would be controlled keeping the critical crack size.

From those contributions to the assessment, the effective mitigation strategy to ease the failure risk can be selectively chosen depending on where the assessment point is located and how much the structure had been irradiated. Considering the benefits of the assessment point location change in the FAD, effective measures can be taken such as warming up the temperature to increase the fracture toughness or reinforcing the structure to relieve the stress.

2.6.6 Structural Margin

In an aspect of the structural margin evaluation, the resistance to fracture failure was accounted for by the toughness factor. For the comparison, the pre-service allowable crack was selected to represent the structural integrity in each state because this size of the crack is an acceptable flaw that remains in structure. From the level B load to the level D load, assuming the linear relation in load increase, the length to the FAD envelope curve is calculated and applied to calculate the ratio dividing the asessment point distance from 0. The structural margin has defined as minus one this value. The structural margin in this study indicates an information of remains to reach the failure status in the FAD approach method. The summurized structural margin values are described in Fig. 2.20.

Overall, the pre-service allowable cracks in all cases have sufficient margin that can allow the severe event. Focusing on the level of irradiation, the severe irradiation condition is more vulnarable when it gets level D extreme load case, compared to the unirradiated condition. For example, while the surface crack in initial unirradiated condition loses margin 38% on average when level D event occurs, the sturctural margin which was in severe irradiation condition loses about 54% on average. The embedded crack also loses the structural margin considerably while it is in the irradiated condition and extreme event level D load is applied.

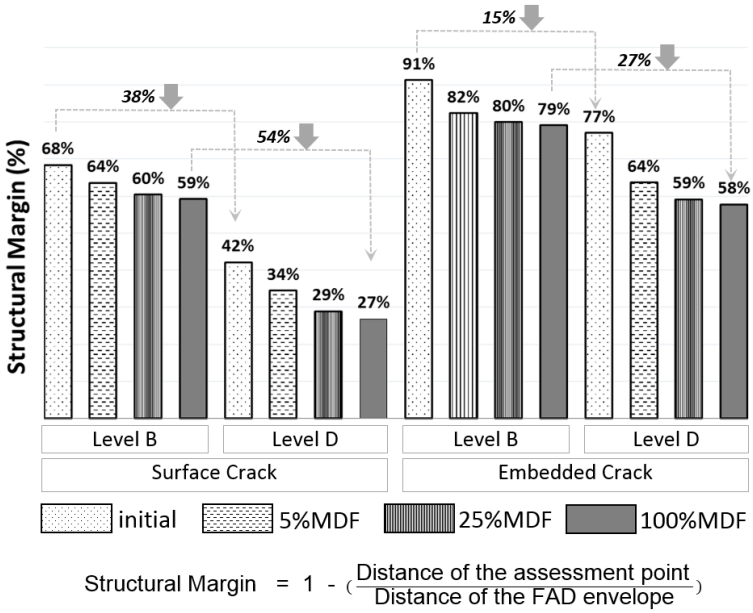

Fig. 2.20 The structural margin based on the maximum pre-service allowable crack of the RPV support in variation of types of crack, load level and the irradiation level

2.7 Conclusions

A failure assessment using the FAD approach of fitness-for-service has been applied to the long-column type RPV supports considering their structural features in harsh conditions such as the neutron embrittlement and the extreme event load case. The long-column type RPV supports design feature was employed in the assessment such as the estimating of the fracture toughness of low-temperature irradiation and the particular structural hot-spots in the column. The finite element analysis was used to analyze the stress generated by this support geometry and the load. The postulated cracks were evaluated with two critical parameters, the toughness ratio, and the load ratio which determine the structure failure mode. The failure assessment followed the API 579. The assessment points were examined by the maximum allowable limits per ASME Sections II [38] and XI [6]. The structural margin was derived from the FAD targeting the pre-service allowable crack. The following conclusions can be drawn from this study.

For defining the physical property of irradiated reactor pressure vessel support system, the low-temperature influence is considered as a sensitive factor in predicting temperature transition for the fracture toughness and the yield strength. When analytic methods are used for a prediction,

a cautious approach is required since most of the analytic equations were derived from the reactor pressure vessel surveillance test data which has a higher temperature than the support system.

The relatively large reference temperature variation moved the fracture toughness in the exponential Equation (3), 44% decrease in fracture toughness initiates from the 25% maximum design fluence level. The fracture toughness trend shows an almost steady value the after. The reason can be explained as follows. The copper and the phosphorus which affect the irradiation hardening reaches to the upper bound and the matrix defect does not influence in this case. The yield strength increase trend is also similar to the fracture toughness.

From the failure assessment of the irradiated RPV supports, the fracture toughness decrease is a parameter more critical rather than the yield strength increase. The maximum permissible assessment points were plotted in the upper part where the toughness ratio governs, rather than to the right part which is the increase of load ratio. The long-column type reactor pressure vessel support system would be predominantly controlled by the brittle fracture mode.

The cracks classified as allowable in the fabrication phase did not cause failure either in the maximum design fluence condition or extreme load events. The in-service maximum allowable size of crack were plotted in the acceptable region in the unirradiated condition. However, after it is irradiated, the maximum allowable crack of surface type surpasses the FAD envelope.

The stress intensity of the surface crack shows conservative result corresponding to its depth compared to the embedded crack. The surface crack may need the depth measurement or to be assumed to classify as a deep crack for a conservative assessment.

When the severe events occur, the cracks which are irradiated tend to move to the unacceptable region more effetively than the unirradiated ones. Likewise in the structural margin, the more irradiated cracks lose considerable structural margin when it comes to the level D load event compared to the less irradiated cracks.

3. STRUCTURAL STRESS DETERMINATION AT A HOT-SPOT

3.1 Introduction

Structural stress analysis is a key procedure to perform a failure assessment in pressure vessel and piping components as the state of stress and deformation are needed for plastic collapse and fracture evaluation. The structural stress in this paper has the meaning of the stress developed in the component across the section thickness, in the form of membrane stress and bending stress in structural analysis. Meanwhile, the finite element analysis (FEA) has been widely used as a practical method to enhance the accuracy over the various structural details so that the structural stress is readily obtained, particularly convenient in shell elements. However, if the structure has a relatively thick cross-section or thickness with complex geometry, then it is recommended not to use the shell elements because the shell theory is less accurate for that geometry. In that case, solid continuum element would be more suitable.

The solid element stress analysis needs an interpretation process such as the stress linearization proposed by Kroenke [70] and Gordon [71] to calculate structural stress in the form of membrane and bending stress. The FEA stress result is total stress combined with non-linear peak stress and the structural stress. The structural stress is taken in a highly concentrated region so the stress in that location usually includes the peak stress in it. Thus, the structural stress needs to be classified in each form of stress separately excluding the peak stress [62]. Moreover, in the highest stressed regions (referred as ‘hot-spots’), singularities are often generated together with the stress analysis result, depending on the geometry and the load combination.

Particularly, this excessive stress in a hot-spot may reach to infinity in a linear elastic analysis if the mesh around this area is sufficiently refined. When the three-dimensional (3D) FEA model is subjected to loads in all three coordinate axes, the singularity affects the structural stress value even though the structural stress was averaged through the thickness. The structural stress determined in a 3D linear elastic analysis is found to be subjective, such as stress divergence with mesh sensitivity, also the structural stress dropping near the hot-spot. Because the six stress components of the orthogonal coordinates are to be substituted into a form of the von Mises equivalent stress or stress intensity, all the stress components influence the von Mises stress whether the stresses components are valid or not.

The works of Kalnins [64] and Trieglaff et al. [72] found relatively non conservative equivalent structural stress in discontinuities. Including Strzelczyk and Stojakovic [73] and Hossain et al. [74], many studies identified the structural stress result is inconsistent, usually in the axisymmetric 3D model.

Meanwhile, there are guidelines for defining the structural stress in 3D. One of the most precise 3D structural stress guidelines of Hechmer and Hollinger [75], endorsed by ASME BPVC Section VIII-2 [62] and Welding Research Council Bulletin 429 [76] provide the guidelines to place the stress classification line (SCL) in a valid location and define the stress using the stress classification rules of the design codes.

Still, engineers often find a gap between applying these guides and the analysis. Valid stress measurement points and the highly stressed regions do not always correspond to same location and stress components to be considered are not clear in the same way by the purpose of analysis between the fatigue analysis and the failure analysis. Also, depending on the failure criteria definition, the equivalent stress results are varied. Therefore, comprehensive methods to determine the structural stress in hot-spots have been largely studied such as, the measurement location or the effective stress to be considered.

However, as an alternative proposal to remove the inconsistency in the 3D FEA hot-spot structural stress analysis, this study divided the 3D geometry into two 2D models in orthogonal directions. After that, five different methods applied in 2D to determine the structural stress. Given that the previous studies, such as Kalnins [64], Trieglaff et al. [72], Strzelczyk and Stojakovic [73] generally covered axisymmetric models for 3D structural stress determination, the transverse stress along the through thickness direction creates the exaggerated structural stress with singularities, the two 2D plane models are needed to study a 3D geometry. Among the applicable previous studies for estimating the structural stress in hot-spots, five approaches are selected for a comparison study, including the stress linearization [62], single point away measurement introduced by Niemi et al. [63], extrapolating stress components applied by Kalnins [64], stress computing from equilibrium equation proposed by Dong [77] and the nodal force method stated by Gordon [71] and Dong [77]. The determined structural stresses in the 2D FEA model are reconstructed as the Cauchy stress tensor components in the 3D stress matrix and are used for the comparison study.

For the 3D FEA stress analysis, a reactor pressure vessel support (RPV support) of a nuclear power plant was selected. The RPV support is a long column type support. It has a relatively thick cross-section in two orthogonal coordinates so the solid continuum element is more applicable for analysis. This support consisted of different cross-sections which are to be gross discontinuities having hot-spots in the 3D model. This support will be vertically divided into two sections according to the *X* coordinate and *Y* coordinate.

3.2 Technical Overview

This section will cover the hot-spot stress concept in FEA and the procedures to determine the corresponding structural stress using different methods.

3.2.1 Hot-Spot Stress Concepts in FEA

The FEA is usually performed to obtain an accurate stress distribution of a component. In the stress analysis result, there may be some highly stressed spots over the structure. These spots are called a 'hot-spot' generally used in the fatigue analysis to identify the most stressed regions [63]. The increased stress at a hot-spot (σ_{total}) contains the added non-linear peak stress (σ_{nlp}) to hot-spot structural stress (σ_{hs}), as expressed in the Eq. (18) and depicted in Fig. 3.1

$$\sigma_{total} = \sigma_{hs} + \sigma_{nlp} \tag{18}$$

The hot-spot structural stress (σ_{hs}) means the structural stress (σ_s) at a hot-spot. The structural stress (σ_s) includes the membrane stress (σ_m) and bending stress (σ_b).

$$\sigma_s = \sigma_m + \sigma_b \tag{19}$$

The membrane stress is the mean stress through the thickness of the section and the bending stress is the linearly proportional stress across the section as given in Eq. (19) and shown in Fig. 3.1. These two structural stresses are used to perform a brittle fracture or crack-like flaw assessment in a form of stress intensity and reference stress [7].

Unless a specific concerned region of a failure assessment component is selected, usually the largest structural stress spot is recommended to select for a conservative failure analysis according to the ASME BPVC Section VIII-2. Typically, the stress determination would be located at a gross structural discontinuity location for failure analysis. The structural stress is a significant parameter in the failure assessment and the largest structural stress can be identified at the hot-

spots. Therefore, as illustrated in Fig. 3.1, the structural stress needs to be determined in the hot-spot to exclude the non-linear peak stress from the total stress and classify the accurate structural stress in a form of membrane and bending stress without being disturbed by the singularity effect.

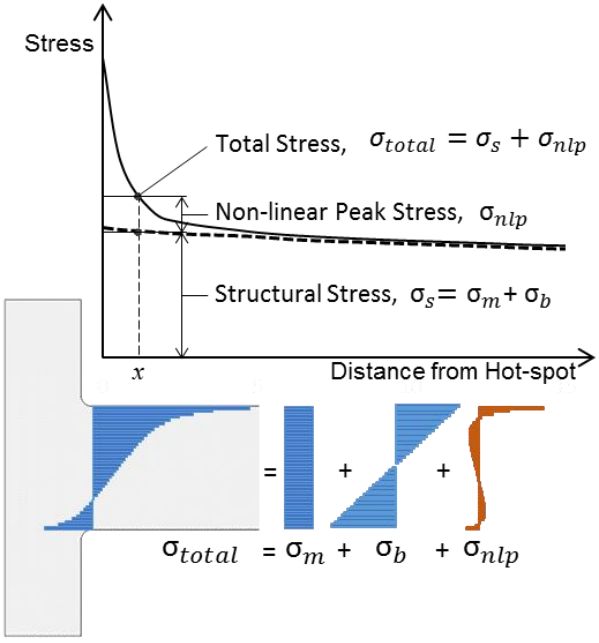

Fig. 3.1. Stress distribution, identification of structural stress (membrane + bending) and non-linear peak stress at hot-spot

In computing the structural stress of the solid element FEA, the structural stress cannot be derived directly from the FEA. Hechmer and Hollinger [75] compared two stress evaluation approaches between the 'stress-at-a-point' and 'stress-along-a-line'. The stress determined at a point was introduced as the simplest but the least accurate method. Thus, taking the stress value at a single point from the stress distribution result would not be desirable. Given that the solid element cannot provide the structural stress which excludes the peak stress at a point, so the stress linearization is applied to read by 'stress along a line' method. To follow the 'stress-along-a-line' evaluation and get classified structural stress in solid element analysis, the stress classification line (SCL) should be defined in the FEA program. The SCL is used to extract the stress components along the through thickness (t) of the section. The stresses found across the section are computed as the membrane and the bending stress tensor components ($\sigma_{ij(m)}, \sigma_{ij(b)}$) with Eq.(20) and Eq.(21). For the membrane stress, the $\sigma_{ij(m)}$ are needed for all the stress components. Meanwhile, for the bending stress, the $\sigma_{ij(b)}$ are calculated with the stress components which are normal to the SCL.

$$\sigma_{ij(m)} = \frac{1}{t}\int_0^t S_{ij}\,dx \tag{20}$$

$$\sigma_{ij(b)} = \frac{6}{t^2}\int_0^t S_{ij}\left(\frac{t}{2} - x\right)dx \tag{21}$$

The stresses are classified by stress components, such as normal stresses S_{11}, S_{22}, S_{33} and shear stresses S_{12}, S_{13}, S_{23}. They are averaged along the thickness in each component ($\sigma_{ij(m)}$, $\sigma_{ij(\mathrm{b})}$) to compute the three principal stresses ($\sigma_1, \sigma_2, \sigma_3$), which are converted into the von Mises equivalent stress (σ_e) by Eq. (22). These Eq. (20) to (22) are from the stress linearization guide in ASME BPVC Section VIII-2 [62] and the fitness-for-service document API 579-1/ASME FFS-1 [7].

$$\sigma_e = \frac{1}{\sqrt{2}}[(\sigma_1 - \sigma_2)^2 + (\sigma_2 - \sigma_3)^2 + (\sigma_3 - \sigma_2)^2]^{0.5} \tag{22}$$

It should be noted that this study covers only the structural stress so that the peak stress is excluded in the hot-spot. Furthermore, the von Mises equivalent stress is implemented for every structural stress result in this study because the failure assessment of API 579-1/ASME FFS-1 method is based on the von Mises yield criterion. Thus, the structural stress result would be rather low as Trieglaff et al. [78] confirmed from a round-robin study.

However, when a FEA program is used in a stress analysis, in spite of the many benefits of the FEA, a numerical disturbance phenomenon often occurs in the hot-spot. This is called the stress singularity. The stress at a singularity contains not only the concentrated stress from geometry but also the unrealistic stress which runs toward the infinite value depending on the mesh size. Given that a hot-spot is mostly at the discontinuities, particularly at a sharp corner or a notch, the stress singularity is usually observed at the hot-spot. Therefore, it is quite challenging to identify the structural stress in the hot-spot excluding not only the non-linear peak stress but also the singularity.

3.2.2 Stress Studies around the Hot-Spot

To understand the structural stress at the hot-spot with the singularity influence, three preliminary studies were performed. One is the stress value at the singularity and the second one is the structural stress at the hot-spot measured over the SCL passing the singularity. Lastly, the structural stress variation according to the distance from the hot-spot was studied. In each study, comparison studies were added between the two-dimensional (2D) models and the three-

dimensional model (3D) and different FEA element sizes. The structural stress value was computed by the ABAQUS stress linearization post processing routine [47], which will be discussed in section 3.4.1 in detail. The ABAQUS linearization report provides classified structural stress into membrane stress, bending stress and nonlinearly varying peak stress.

The 2D stress analysis result is represented by the case study of the Kalnins [64] with an additional even finer mesh size. The 2D model, illustrated in Fig. 3.2 (a), is two overlapped 12 mm thick-plates subjected to a 1,200 N tensile force with the left end restrained from vertical and horizontal displacement and the right end restrained from vertical displacement. The modulus of elasticity, *E* of 207 GPa was chosen and the Poisson`s ratio was 0. The FEA element used in this model was mostly 2D 8 - noded quadratic solid plane strain quadrilateral element (CPE8) and partly 2D 6 - noded quadratic solid plane strain triangle element (CPE6) near the hot-spot. These FEA models have different mesh sizes of one element through the thickness and two elements and four elements through the thickness. The singularities were observed at the hot-spot from the linear analysis and SCLs were defined passing the singularities, see Fig. 3.2 (a).

(a) (b)

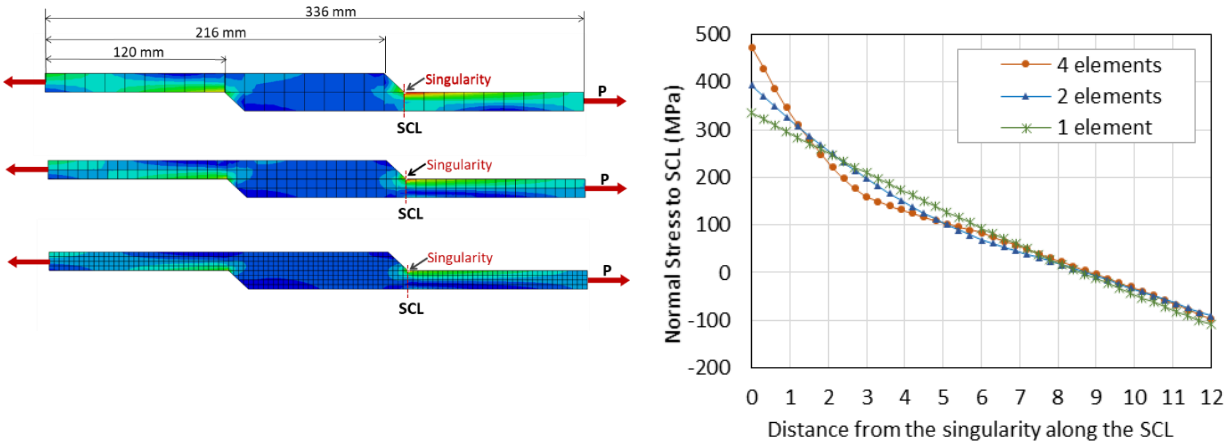

Fig. 3.2. Stress analysis result of 2D plate in tension (Based on the model from Kalnins [64])
(a) 2D Finite element model example (b) Normal stress to SCL result for each number of elements

The 3D linear stress analysis was performed using the RPV support model according to the APR 1400 design control document [16]. The 3D RPV support FEA model and applied loading are shown in Fig. 3.3(a). The RPV support is comprised of 7 in. (178 mm) thick flange plate, 30 in. x 11 in. (762 mm x 279 mm) rectangular cross-section support column and 10 in. (254 mm) thick-base plate. The overall height is 20 ft (6.1 m) and fixed at base plate with the shear key

embedded in concrete foundation. The modulus of elasticity, E is 27,847 ksi (191,998 MPa) and Poisson`s ratio is 0.3. These material properties are taken from the service temperature, 150° F (66° C), of the SA-508 steel provided in ASME BPVC Section II-D [45].

The applied meshes are in three uniform sizes, 0.5 in. (12.7 mm), 1 in. (25.4 mm) and 1.25 in. (31.8 mm) with 3D 20 noded quadratic structural solid element (C3D20). The forces and moments shown in Fig. (a) are applied on the flange plate in x, y and z directions. This support column is built up by forging, in one piece with typical fillet radius of 1 in. (25.4 mm) at the intersection of the flange and the column. However, modelling fillet was not possible because it produces distorted elements in the 3D mesh so sharp corners were hard to be avoided. There were two hot-spots generated at the column in discontinuities. In this analysis, the hot-spot between the flange and the column was selected where the fillet modelling was not feasible in 3D solid mesh. Besides this hot-spot with singularity, several SCLs were additionally selected at and away from the hot-spot. The SCLs for the 3D model are indicated in upper right side of Fig. 3.3(a).

(a)

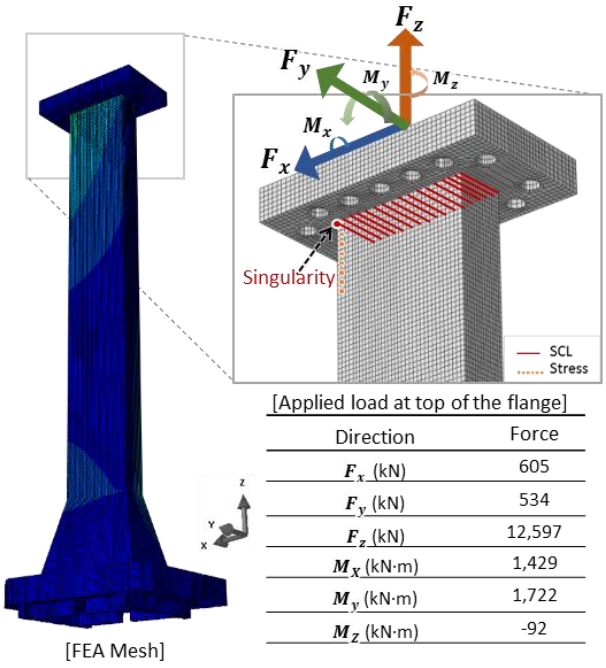

[Applied load at top of the flange]

Direction	Force
F_x (kN)	605
F_y (kN)	534
F_z (kN)	12,597
M_x (kN·m)	1,429
M_y (kN·m)	1,722
M_z (kN·m)	-92

Fig. 3.3. Stress analysis result of RPV support 3D FEA

(a) 3D Finite element model, 1" mesh size mesh and the load applied; (b) Von-Mises stress result from the corner; (c) Structural stress result of SCL from the corner in the hot-spot (To convert to MPa, multiply values in ksi by 6.894. To convert to mm, multiply values in inches by 25.4.)

Fig. 3.3. continued

(b)

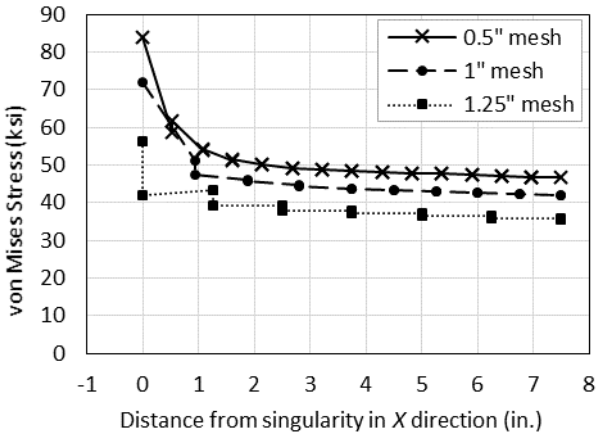

(c)

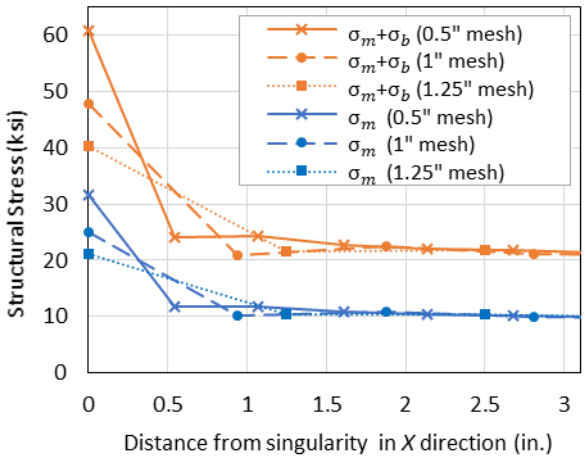

The stress result of each model showed the stress singularities as expected. In 2D analysis, the stress normal to SCL at singularity with one element through thickness mesh FEA shows 336 MPa but the stress with four elements through thickness mesh was 474 MPa (Fig. 3.2 (a)). Likewise, in the 3D model the stress plot of Fig. 3.3 (b), the singularity stress shows about 10 ksi (69 MPa) difference between the different mesh sizes. The stress measuring points of Fig. 3.3(b) are dotted on the Fig. 3.3 (a). Not surprisingly, the observed singularity stresses were unreliable showing different value for the different mesh size.

Meanwhile, the hot-spot structural stresses of 2D FEA show mesh insensitivity as given in Table 3.1, whereas the 3D results do not. Table 3.1 shows that the structural stress results give

similar values for all three mesh sizes even though at the singularity, at the beginning point of SCL, the stress showed divergence (see Fig. 3.2 (b)). It means that the stress linearization in the 2D model results in constant structural stress irrespective of the element size.

Table 3.1. Structural stress result of 2D plate in tension (in MPa)

Number of elements through SCL	Membrane Stress $\sigma_{22(m)}$	Bending Stress $\sigma_{22(b)}$	Stress at Singularity S_{22}
1	100.0	223.1	335.9
2	100.0	224.3	393.3
4	100.1	224.5	473.7

On the other hand, it can be claimed that at least in the 3D analysis, the structural stress of a hot-spot may be inaccurate depending on the mesh size. In the Fig. 3.3 (c) and Table 3.2, the structural stress near the singularity of the 3D RPV support showed different values by element sizes. The structural stress difference at the singularity was approximately 10 ksi (69 MPa) between the different mesh sizes. Taking into account of the elements across the SCL which are confining the load in perpendicular direction to the SCL, the analyzed structural stress components in 3D may still have exaggerated stresses affected by singularity, although structural stresses are an averaged value.

Table 3.2. Structural stress result of 3D RPV support (in ksi[a])

Element Size	Membrane Stress σ_m	Bending Stress σ_b	Stress at Singularity σ_e
1.25”	21	19	56
1”	25	23	72
0.5”	32	29	84

[a.] To convert to MPa, multiply values in table by 6.894

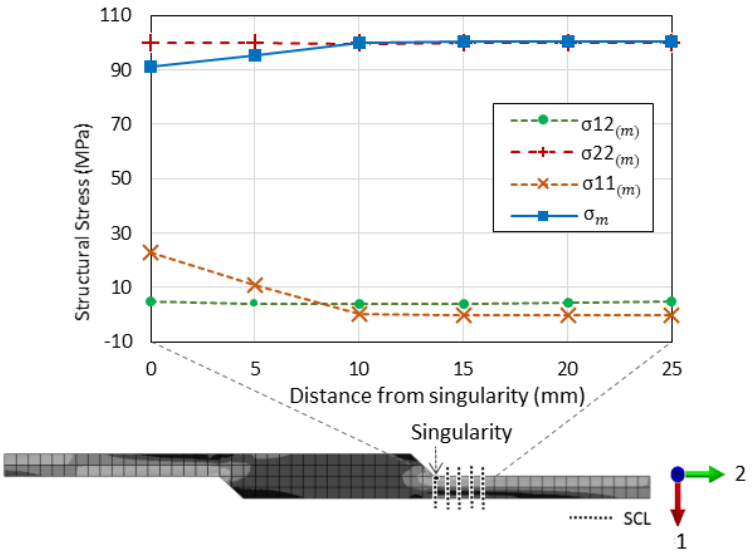

Fig. 3.4. 2D plates structural stress distribution along the distance from the hot-spot (6 mm mesh)

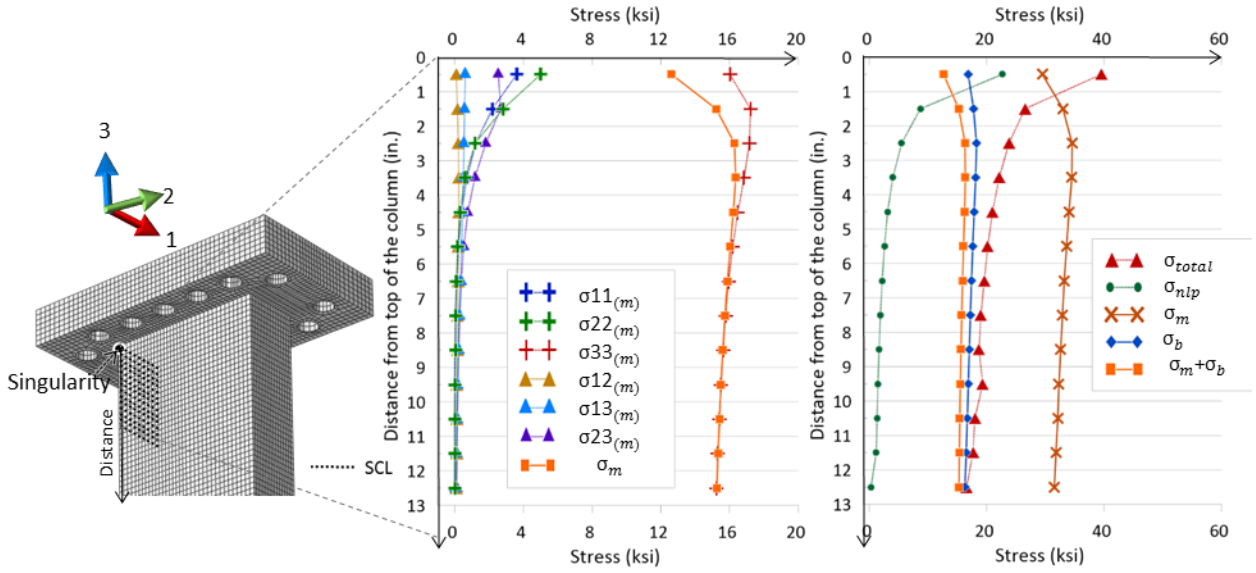

Fig. 3.5. 3D RPV support stress distribution along the distance from the hot-spot (1" mesh) (To convert to MPa, multiply values in ksi by 6.894. To convert to mm, multiply values in inches by 25.4.)

Some other structural stress distribution graphs are plotted in Fig. 3.4 and Fig. 3.5 in order to see the change in structural stress results with respect to the distance from the singularity. Fig. 3.4 is the structural stress distribution of the 2D example. The membrane stress, $\sigma_{11(m)}$ is averaged

normal stress parallel with SCL. The other membrane stress, $\sigma_{22(m)}$ is averaged normal stress perpendicular to SCL. Lastly, another membrane stress, the $\sigma_{12(m)}$ is the average shear stress on the SCL. These membrane stress components are substituted into the von Mises equivalent stress, expressed as σ_m. Fig. 3.5 shows the structural stress of the 3D example measured in different locations along the local coordinate number 3 axis coordinate from the singularity. In 3D FEA stress linearization, $\sigma_{33(m)}$ and $\sigma_{13(m)}$, $\sigma_{23(m)}$ are added to other three in-plane components, $\sigma_{11(m)}$, $\sigma_{22(m)}$, and $\sigma_{12(m)}$. The $\sigma_{33(m)}$ is averaged normal stress in the 3-axis direction, perpendicular to the SCL. The $\sigma_{13(m)}$ and the $\sigma_{23(m)}$ are the averaged out-of-plane shear stresses, flow on the respectively local 1 and 2 coordinates, toward the local 3 coordinate.

From the results of Fig. 3.4 and Fig. 3.5, a distinctive point in stress variations is observed that the hot-spot structural stress location does not correspond to the maximum stress location of the FEA stress distribution result. Seeing the variation of the structural stress, whether it is 2D or 3D, the maximum structural stress is not at the point of singularity, where it was determined as the maximum stress point from FEA. It means that the stress result from the FEA stress analysis does not correspond to the structural stress result. The hot-spot location is usually expected to be at the geometric discontinuities, specifically on a smaller section of the model because the structural stress is concentrated and the peak stress (σ_{nlp}) is maximized. Unless the model parameters are changed in the hot-spot region, the decreased structural stress at the hot-spot is hardly explainable.

The reason for the dislocation between hot-spot structural stress and the FEA total stress is assumed to be the exaggerated stress components within the influence of singularity. As the measuring point approaches the hot-spot, the decrease of the structural stresses ($\sigma_{m,}$ σ_b) and increase of the averaged stress components ($\sigma_{ij(m)}$) occurred together. Considering that the structural stress is calculated by the von Mises stress Eq. (22), using the increased stress components near the singularity would drop the equivalent structural stress.

From these two examples, several characteristics of the hot-spot stress determined by FEA are identified. First, the stress value at the singularity was exaggerated depending on the mesh size. Second, the 3D model shows structural stress divergence at singularity. Lastly, the structural stress analyzed by stress linearization decreased at the hot-spot so the maximum structural stress location is not corresponding to the maximum stress result of the FEA.

3.2.3 Scope and Objective

From the observed findings from Section 3.2.2, this study aimed to investigate the 3D structural stress at the hot-spot excluding the mesh sensitivity and singularity. The 3D model will be divided into two 2D plane models to resolve the confined stress in 3D SCL and remove the sharp edges to relieve the singularity. The structural stress will be estimated in the 2D FEA model in each of five different approaches to compute reasonably accurate values. Also, not only the structural stress value, the mesh sensitivity and the structural stress decrease effect will be investigated for each method. Lastly, the structural stress from two 2D models will be assembled to a 3 x 3 stress matrix to derive the structural stress in 3D analysis result to propose the most suitable structural stress approach for 3D solid element FEA.

3.2.4 Previous Studies in Hot-Spot Stress Using FEA

The hot-spot stress approaches were initiated from the fatigue analysis of offshore structures and expanded for use to other types of plate structures. With the need of assessing fatigue life particularly the welded part under the cyclic loads, the approaches of structural stress determination has largely been developed. The International Institute of Welding (IIW) provided a hot-spot stress determination method based on the Niemi and coworkers` study on the stress in fatigue analysis [63]. They developed the surface stress extrapolation procedures. Also, the stresses at the discontinuities were widely studied using the stress concentration factors for specific joints. However, these approaches were often sensitive in mesh size, geometries and loading modes. Depending on the structural geometry and size, the stress concentration factors had been investigated [79–82]. In consideration of structural force and moment equilibrium independent of the influence of the mesh size and loading modes, another stress analysis method was presented by Dong [77]. Furthermore, as the design and analysis of pressure vessels or tubular structures use the categorized stress from the FEA result, the stress classification has been focused on as a prominent issue. Gordon [71] compared the structural stress calculation in various approaches. Lu, Chen and Li [83] proposed to decompose the stress from FEA. Hollinger and Hechmer [65] developed the 3D structural stress criteria for ASME BPVC VIII-2 [62]. Strzelczyk and Stojakovic [73] and Kalnins [64] discussed the stress and stress intensity in singularity. To decrease the effort of solid element stress linearization method, Strzelczyk and Ho [84] proposed an element stress linearization method and simplified the non-linear stress distribution. Hélénon et al. [85] proposed

an approach to distinguish the high stress in FEA whether it leads to failure. Rother and Fricke [86] suggested a method to derive notch stress in low stress concentration. Muscat et al. [87] compared the structural stress approaches in pressure vessel components with mesh density and different elements in 2D. Pedersen [88] analyzed the multi-axial load criteria with respect to the probability of fatigue failure. Mackenzie [89] studied the stress linearization restrictions in elastic design by analysis and Trieglaff et al. [72] compared the methods for structural stress determination of European Pressure Vessel Standard (EN 13445). The recommended guides to understand structural stress are endorsed in the American Society of Mechanical Engineers (ASME) BPVC code [37,62] and Welding Research Council (WRC) designer`s guide [63].

3.3 Computational 2D Model of RPV Support

The RPV support 3D model discussed in the preliminary study in Section 3.2.2 was vertically cut into two 2D models, X and Y sections, as illustrated in Fig. 3.6.

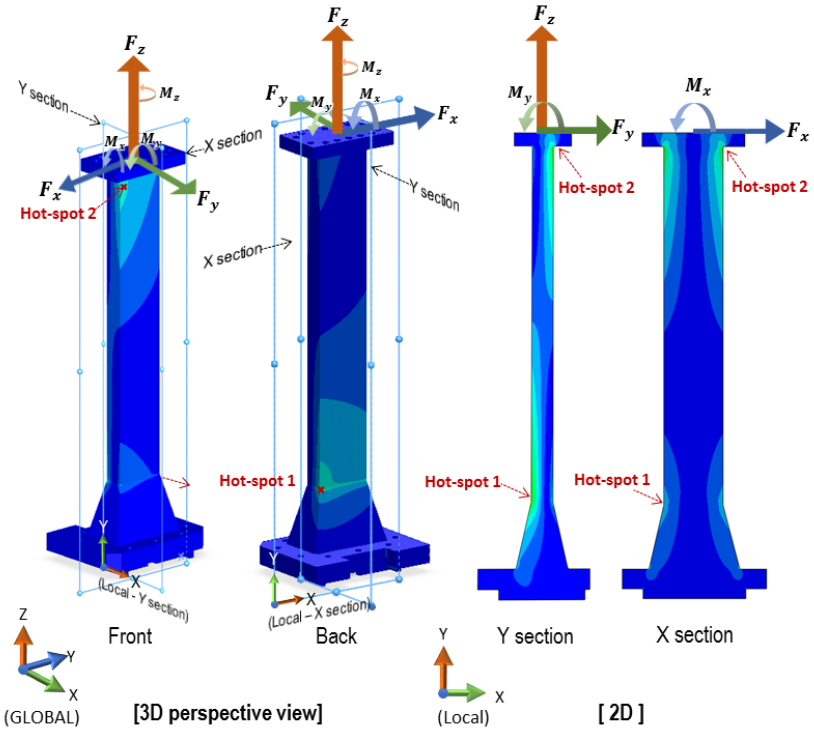

Fig. 3.6. Reactor vessel support FEA stress analysis in 2D and 3D

The forces of 3D model separately applied to 2D models to avoid overlapping when they are constructed in a 3D stress matrix. The shear force F_x and moment force M_x act in the X section

and the shear force F_y, moment force M_y and tension force F_z act in the Y section. The only ignored force component is the twisting moment, M_z. The M_z was so small relative to other forces that it is hardly effective in analysis. See Fig. 3.6 for the applied loadings. Each 2D model is including the two hot-spots which were previously found in 3D analysis in Section 3.2.2. The hot-spot 1 is the point where the rectangular column section changes to the trapezoidal frustum in the bottom. The hot-spot 2 is in the upper corner of the column where the column intersects to the flange. These two hot-spot locations are marked with red arrows in Fig. 3.6 and Fig. 3.7.

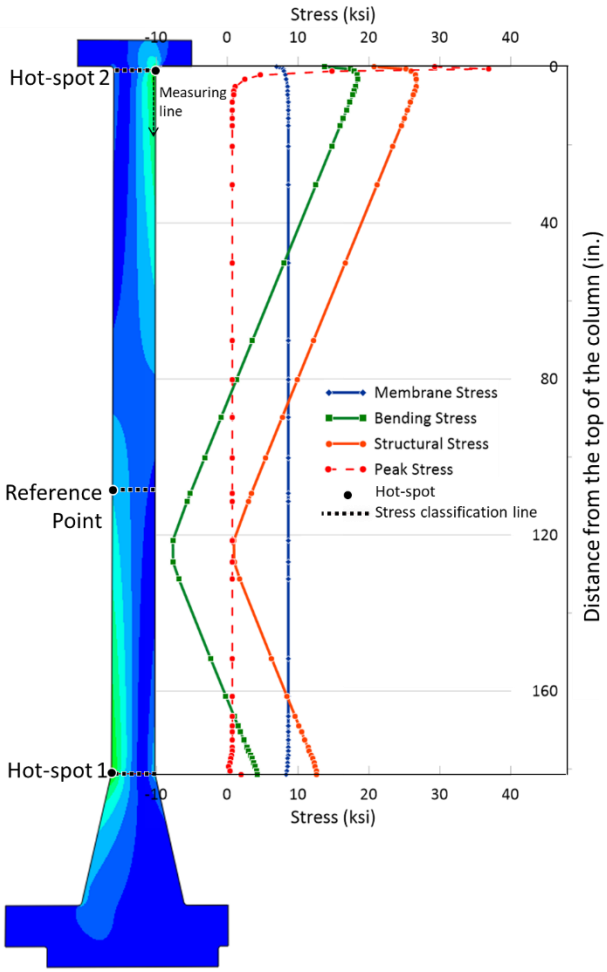

Fig. 3.7. The stress distribution along the vertical direction through the structural hot-spots (To convert to MPa, multiply values in table by 6.894. To convert to mm, multiply values in inches by 25.4.)

The Fig. 3.7 shows the structural stress distributions on the 2D -Y section along the height, derived from the ABAQUS stress linearization in using 0.4 in. (10 mm) uniform mesh size. As shown in the stress plot in Fig. 3.7, a large magnitude of peak stress occurred at hot-spots and structural stress decreased at hot-spots.

3.3.1 Finite Element Modelling

The RPV 2D model linear analysis was carried out using the finite element program, ABAQUS 2017 [47]. The model was meshed using 2D 8 - noded quadratic structural solid plane stress elements, CPS8, because the stress perpendicular to the 2D section at nominal location was found to be negligible in 3D analysis. There were six models built to examine the mesh sensitivity, in three different mesh sizes of 0.4 in. (10 mm), 0.25 in. (6.4 mm) and 0.1 in. (2.5 mm), and in both X and Y sections. The mesh size was selected based on the suggested element size from the Niemi et al. [63]. They introduced two suggested mesh sizes. One is the 10 mm size course mesh to screen the hot-spot location and the other one is 4 mm and less size which is a finer mesh to check the stress in detail. In accordance with the suggested element size, the course mesh is represented as 0.4 in. (10 mm) mesh and the finest mesh is 0.1 in. (2.5 mm), and medium sized mesh is 0.25 in. (6.4 mm). The same material properties as listed in the 3D FEA model in Section 3.2.2 were used.

The 2D model configuration and applied loads are presented in the right hand side of Fig. 3.6. The RPV support in the X section consists of 30 in. (762 mm) width 214 in. (5,436 mm) long column support, 7 in. (178 mm) thick and 52 in. (1,321 mm) width flange plate and 10 in. (254 mm) thick and 73 in. (1,854 mm) width base plate. The components in the Y - section have the same height as the X - section because they lie in a perpendicular plane to the X section. The column width in the Y - section is 11 in. (279 mm), 30 in. (762 mm) width flange plate in the upper, and 56 in. (1,422 mm) width base plate are attached to the column support. The applied load values are shown in Fig. 3.4. The F_x, F_y and F_z forces are distributed over the top of the flange. The applied load values are converted to distributed loads by dividing the load by the transverse section thickness and the upper flange plate width.

Another difference between the 2D and 3D models is the fillet modeling. In 2D models, a fillet of 1 in. (25.4 mm) fillet radius was created at the intersection of the flange plate and the column support which is at the start point and end point of the hot-spot 2 SCL line. Likewise, 0.2 in. (5.1 mm) radius fillet was modeled on the top of the trapezoidal section where hot-spot 1 SCL line starts and finishes. The 1 in. (25.4 mm) fillet was specified in the design documents, however, the 0.2 in. (5.1 mm) fillet was not specified in the design documents, but a reasonable size fillet considering the forging process. All structural stress estimating approaches in this study used the fillet 2D model. To check the fillet effect, a no-fillet-2D model was also created for comparison.

3.3.2 The Method of Assembling the Structural Stress Result in 3D Using the Result of 2D Models

The 3D hot-spot structural stress along the SCL passing through the singularity is calculated from the 3x3 matrix with six stress tensor components as expressed in brackets in the lower left corner of Fig. 3.8.

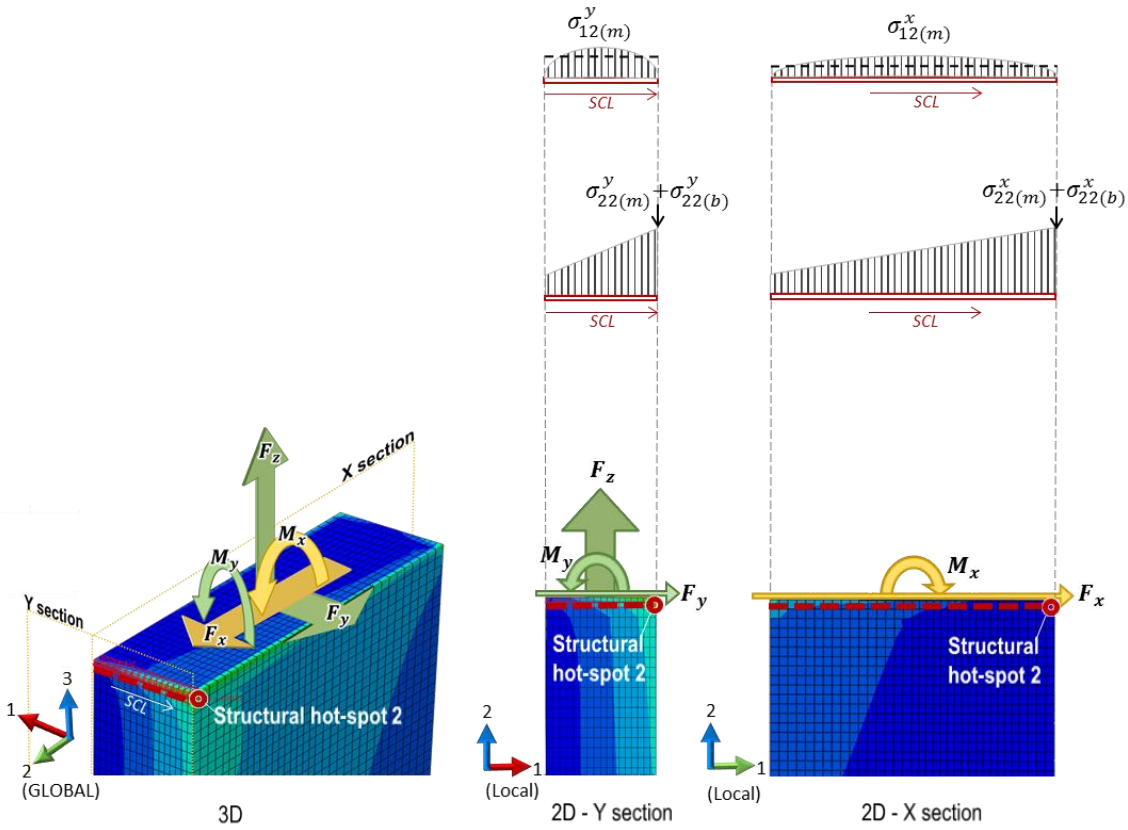

$$\sigma_S = \begin{bmatrix} 0 & 0 & \sigma^{y}_{12(m)} \\ & 0 & \sigma^{X}_{12(m)} \\ Symmetric & & \sigma^{y}_{22(m)}+\sigma^{y}_{22(b)} + \sigma^{X}_{22(m)}+\sigma^{X}_{22(b)} \end{bmatrix} = \begin{bmatrix} 0 & 0 & \sigma^{y}_{12(m)} \\ & 0 & 0 \\ Symmetric & & \sigma^{y}_{22(m)}+\sigma^{y}_{22(b)} \end{bmatrix} + \begin{bmatrix} 0 & 0 & 0 \\ & 0 & \sigma^{X}_{12(m)} \\ Symmetric & & \sigma^{X}_{22(m)}+\sigma^{X}_{22(b)} \end{bmatrix}$$

Fig. 3.8. The stress matrix composition of the RPV support FEA stress analysis

The 2D – *X* and *Y* section and corresponding stress components ($\sigma^{x}_{12(m)}$, $\sigma^{y}_{22(m)}$, $\sigma^{y}_{12(m)}$) are following local coordinate system. The applied loads illustrated in Fig. 3.8 are to be applied on the top surface of the flange plate in the analysis. However, the flange plate was omitted from Fig. 3.8 for clarification to show the SCL line. The F_x and F_y generate the shear stress ($\sigma^{x}_{12(m)}$, $\sigma^{y}_{12(m)}$) and the F_z is converted to the normal stress ($\sigma^{y}_{22(m)}$). The moments (M_x, M_y) contribute to

perpendicular stress over the SCL, which are the bending stress ($\sigma^{y}_{22(b)}$) and the normal stress ($\sigma^{y}_{22(m)}$). The loads to be applied to the *Y* section are F_y, M_y and F_z forces. An SCL in the *Y* section along the thickness is set to get the stress components by the stress linearization method. In the stress linearization result, the F_y will be expressed in the form of the averaged shear stress $\sigma^{y}_{12(m)}$and the F_z and M_y will return the normal stress $\sigma^{y}_{22(m)}$ acting on the SCL. The bending stress $\sigma^{y}_{22(b)}$ will be the result from the M_y force. Likewise, in the *X* section, the applied F_x generates the shear stress, $\sigma^{x}_{12(m)}$ and the M_x generates the bending stress $\sigma^{x}_{22(b)}$and the normal stress $\sigma^{x}_{22(m)}$.

Considering the coordinate system in 3D analysis, the shear stress of *Y* section ($\sigma^{y}_{12(m)}$) is inserted into the S_{13} location and the shear stress in *X* section $\sigma^{x}_{12(m)}$ will compose the S_{23} location in the matrix. Meanwhile, F_z, M_y and M_x forces stretch the support to the 3 direction. Therefore, the stresses generated by this stretching direction, such as $\sigma^{y}_{22(m)}$, $\sigma^{y}_{22(b)}$, $\sigma^{x}_{22(m)}$, and $\sigma^{x}_{22(b)}$ will be included in the S_{33} location. The $\sigma^{y}_{22(m)}$, $\sigma^{x}_{22(m)}$ and $\sigma^{x}_{22(b)}$ account for membrane stress because they are constant through the SCL. It should be noted that the $\sigma^{x}_{22(b)}$, taken from the *X* direction SCL, acts as constant membrane stress in 3D and this contributes to the hot-spot stress to affect the higher stress value. The $\sigma^{x}_{22(b)}$ is illustrated in the stress distribution along the SCL, upper right part of Fig. 3.8. When it comes to include the bending stress, the stress linearly varies perpendicular to the SCL direction, and $\sigma^{y}_{22(b)}$ should be included in the matrix.

Meanwhile, the stress value in the matrix expressed in zero may occur depending on the stress components to be considered in structural stress analysis. Depending on the structural stress approaches, some normal stresses which are not from the mechanical load can be included in the analysis. These cases will be defined after the analysis and introduced in section 3.5.2.

Except for these cases, the structural stress, which combines the membrane stress and bending stress, is presented by the 3x3 matrix in Fig. 3.9. For the membrane stress, the $\sigma^{y}_{22(b)}$ should be removed from the matrix. By the matrix composed of the 2D sections, the principal stresses and the von Mises stress are calculated by the Eq. (22).

3.4 2D Structural Stress Analysis

This section will review the available approaches to hot-spot stress and estimate the structural stress based on the 2D RPV support computational models discussed earlier. The structural stress will be measured at three points: hot-spot 1, hot-spot 2 and a reference point away from the discontinuities. The reference point is at 116 in. (2.94 m) height which is half of the column height. This point is where the cross-section is far from the hot-spots so that peak stress effect is negligible compared with the hot-spot stress. These three locations are presented in Fig. 3.7. The structural stress is normalized by nominal stress to observe the influence of the hot-spot using the Eq. (23).

$$SSR = \sigma_s/\sigma_{nom} \tag{23}$$

The structural stress ratio (*SSR*) is computed by dividing the structural stress (σ_s) of the point by the nominal structural stress (σ_{nom}).The nominal structural stress is obtained by hand calculation using the classical beam theory. The nominal stresses including membrane, bending and structural stresses at each point are provided in Table 3.3. There were three models with different sizes of elements to study the mesh sensitivity with respect to locations and estimating approaches.

Table 3.3. Nominal structural stress (σ_{nom}) in each spot in ksi [a]

Location	Membrane Stress (σ_m)	Bending Stress (σ_b)	Structural Stress ($\sigma_s = \sigma_m + \sigma_b$)
Hot-spot 1	13.12	21.55	34.67
Reference Point	8.63	5.92	14.55
Hot-spot 2	16.95	18.55	35.50

[a] To convert to MPa, multiply values in table by 6.894

The structural stress obtained from ABAQUS stress linearization tool is used for comparison together with each hot-spot stress approach result to identify the changes of structural stress near hot-spots. A comparative study of different structural stress approaches is carried out in the *Y* section on behalf of the 2D FEA study because the loads applied in *Y* are larger than *X*. The *X* section results were calculated separately and were presented in Section 3.5 to construct 3D

FEA structural stress. In each analysis, the stress result was selected with no averaging option in ABAQUS for conservative results.

In the following sections, the structural stress determination approaches applied in 2D FEA will be explained and their stress results will be provided.

3.4.1 Stress Linearization

In solid continuum element models, the stress result from FEA is total stress. Therefore, the membrane and bending stresses should be computed separately from the total stress, and a line across the thickness of the section is needed. Therefore, the stress classification line (SCL) is defined across a section through the thickness to compute the structural stress. Stress linearization is classifying the stress components in all directions along the SCL and computing the von Mises equivalent structural stress using the Eq. (20) to (22). This study used the ABAQUS stress linearization tool, which conveniently computes the structural stresses. The SCL paths were defined to pass through the singularities of the two hot-spots and the reference point at the mid-height of the column.

The results of the structural stress using the stress linearization are shown in Fig. 3.9 and the stress values for 0.4 in. (10 mm) mesh size are provided in Table 3.4. In Fig. 3.9 (a), the structural stress of the two hot-spots shows relatively smaller results as compared to the nominal stress. The smaller structural stress result in hot-spots is similar to the result obtained from the preliminary study in the 3D RPV support example analysis presented in Section 3.2.2. At the hot-spot 2 the *SSR* is approximately 0.90 while the hot-spot 1 SSR is about 0.97. Meanwhile the *SSR*s of reference point are 1.0 which means that the structural stress is the same as the nominal stress value. In all measuring spots, mesh sensitivity is not very influential to the result when the stress linearization approach is applied. This result supports that the 2D FEA does not have mesh sensitivity, with respect to the structural stress results. This was also observed at the plate example result of Kalnins [64] presented in Section 3.2.2 and the preliminary study in Table 3.1

(a)

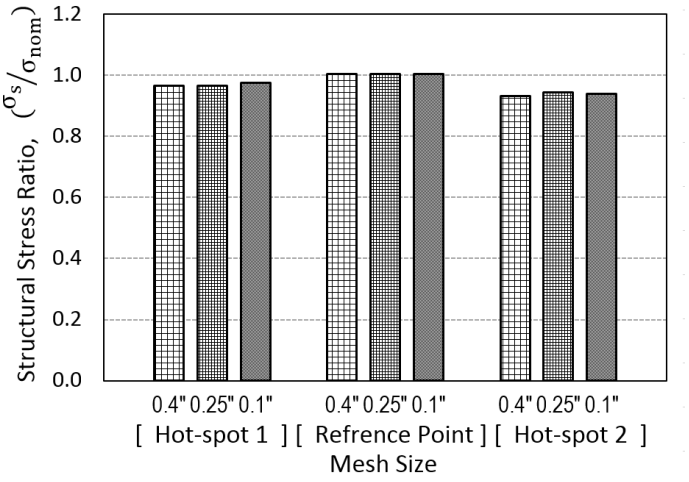

(b)

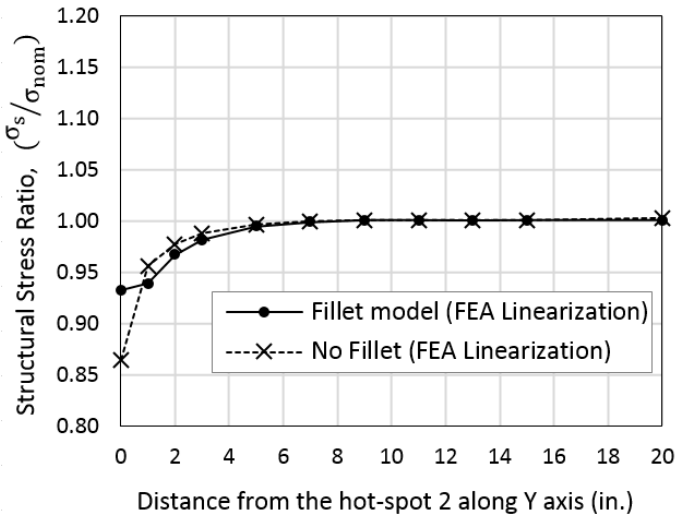

Fig. 3.9. Structural stress result from the stress linearization

(a) Comparison of mesh sensitivity at hot-spots and the reference point, (b) Distribution of the structural stress close to the hot-spot 2, comparing the fillet model and the no fillet model in ABAQUS linearization at hot-spot 2 with 0.4" (10.2 mm) mesh size (To convert to mm, multiply values in inches by 25.4.)

Table 3.4 The structural stress measured from the hot-spots in 0.4 in. (10.2 mm) size mesh, 2D model (*Y* section, in ksi [a])

Method	Structural stress (ksi)					
	Hot-spot1			Hot-spot2		
	σ_m	σ_b	σ_s	σ_m	σ_b	σ_s
Fillet modelling	8.3	21	29	7.8	17	25
Single point away from hot-spot [63]	8.3	21	29	8.0	18	26
Extrapolated in 2D [64]	8.6	21	30	8.5	19	27
Stress from equilibrium [77]	8.3	21	29	8.0	18	26
Nodal force method [71]	8.6	21	30	8.5	19	27

[a] To convert to MPa, multiply values in table by 6.894

The structural stress plot with respect to the distance from the singularity of hot-spot 2 is plotted in Fig. 3.9 (b). As expected in the Fig. 3.3 Fig. and Fig. 3.9 (a) graphs, the structural stress near the singularity shows a decrease when it is derived using the ABAQUS stress linearization tool. This conforms to the decrease of structural stress observed in 3D FEA presented in Section 3.2.2. Given that the fillet modelling was not feasible in 3D analysis, another 2D model with no fillet was modeled and processed with the stress linearization approach to check the effect of the fillet modeling, plotted in dashed line with x-shaped markers. The *SSR* at the singularity of the model with a fillet is 0.93 and the model without a fillet is 0.86. In the model with a fillet, the nominal stress drops as the fillet enlarges the area of cross-section. Thus, the slope near the hot-spot rebounded in the fillet model. This fillet modeling helped to relieve the amount of *SSR* with a increase in the hot-spot by 8% compared to without fillet case.

The benefit of modelling the fillet in structural analysis was observed in Fig. 3.9 (b) in terms of the rebounded *SSR* in the hot-spot. Moreover, the stress divergence is quite removed at the fillet. The von Mises stress result at hot-spot 2 of the *Y* section is given in Fig. 3.10. When the model was created with a fillet at the reentrant corner, the maximum stress range was from 58 ksi (400 MPa) to 59 ksi (407 MPa) in different mesh sizes. However, the maximum stress in the no-fillet models show considerable difference according to the mesh sizes. In particular, the 0.4 in. (10 mm) mesh size shows 91 ksi (627 MPa), while the 0.1 in. (0.25 mm) mesh showed 168 ksi (1,158 MPa) maximum stresses. Therefore, even though the 2D analysis with a fillet still showed

decreased structural stress at hot-spot, it can be claimed that the singularity problem seems to be solved after removing the reentrant corners and adding fillet. However, it is not reasonable to state that the singularity effect was removed in structural stress analysis because the structural stress result still drops near the hot-spot.

With Fillet	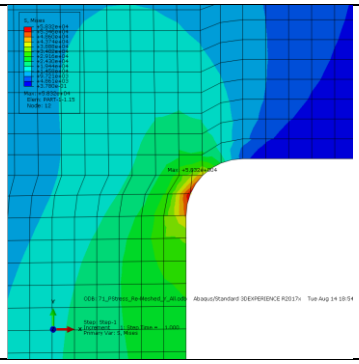	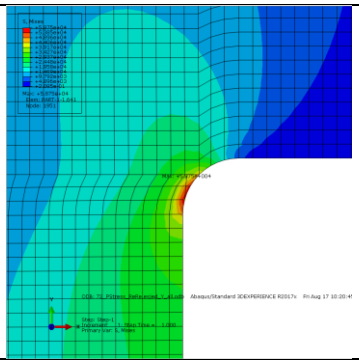	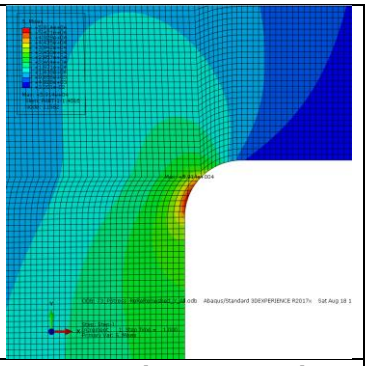
Result	0.4 in. mesh, Max. 58.32 ksi	0.25 in. mesh, Max. 58.75 ksi	0.1 in. mesh, Max. 59.14 ksi
No Fillet	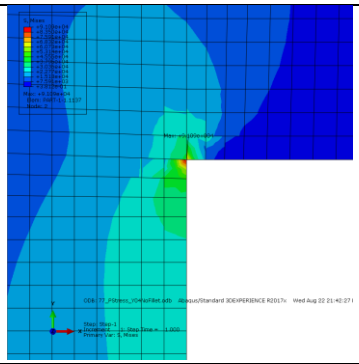	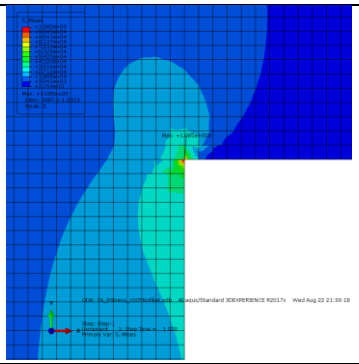	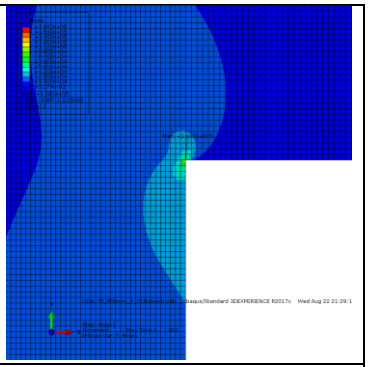
Result	0.4 in. mesh, Max. 51.09 ksi	0.25in. mesh, Max. 108.5 ksi	0.1in. mesh, Max. 168.0 ksi

Fig. 3.10. The maximum von-Mises stress at hot-spot 2 from the 2D Y section model (in ksi, To convert to MPa, multiply values in ksi by 6.894. To convert to mm, multiply values in inches by 25.4.)

As discussed in Niemi et al. [63], stress linearization is generally applicable to where the discontinuities in geometry occur on the surface such as the fillet weldment region. Stress linearization in a thick plate type structure is not recommended because of the possibility of structural stress exaggeration. Reminding that the thicknesses of the model are 11 in. (279 mm) in *Y* direction and 30 in. (762 mm) in *X* direction (see Fig. 3.6). The singularity occurred at the gross discontinuities, the stress linearization approach may be not recommendable. Kalnins [64] also discovered a similar trend in structural stress analysis suggesting that the stress linearization using

FEA should not be used where the SCL passes through the singularity because the value of equivalent stress output is not valid, rather smaller than expected. From this observation, an alternative approach was proposed. Kalnins extrapolated exaggerated stress components at the hot-spot. This extrapolating approach will be reported in Section 4.3. Similarly, Niemi et al. [63] proposed surface extrapolation using the structural stress in the vicinity of the hot-spot surface and taking the structural stress at a single element away from the hot-spot which will be discussed next.

3.4.2 Stress at Single Point Close to Hot-Spot

Stress concentrates in a relatively short distance at the discontinuities of the model where the stress flow has been disturbed (see Fig. 3.1). Niemi et al. [63] proposed that at a single point sufficiently close to the hot-spot, the influence of nonlinear peak stress can be avoided. As previously stated in section 3.4.1, this RPV support has a relatively thick section with global discontinuities. According to the category of the hot-spot suggested in Niemi et al. [63], this RPV support is classified as type "b". The suggested extrapolation point for the type "b" is 5 mm.

Meanwhile, the proposed mesh size in Niemi et al. is smaller than 0.5 mm (0.02 in.) to sufficiently the remove the influence of the stress singularity. However, meshing the 0.5 mm (0.02 in.) refined element size on the entire model is very inefficient since the major stress gradient occurs at the location of hot-spots. Therefore, this study applied a gradual mesh size from 0.5 in. (12.5 mm) to the 0.008 in. (0.2 mm) size in concentric circular shaped partitioning near the hot-spots as shown in Fig. 3.11 (a). The measurement point was 5 mm away from the hot-spot, following the Niemi et al. [63].

Moreover, this study analyzed three additional models for the single point away approach. The uniform mesh sizes of 0.4 in. (10 mm), 0.25 in. (6.4 mm) and 0.1 in. (2.5 mm) models were added with no localized gradient mesh to check whether the peak stress was removed at one element away with no mesh sensitivity. The 0.4 in. (10 mm) mesh size model is illustrated in Fig. 3.11 (b) indicating the single point for measurement at one element away distance. Note that, the 0.1 in. (2.5 mm) mesh size model also conforms with the Haibach [78] proposed distance of 2.5 mm.

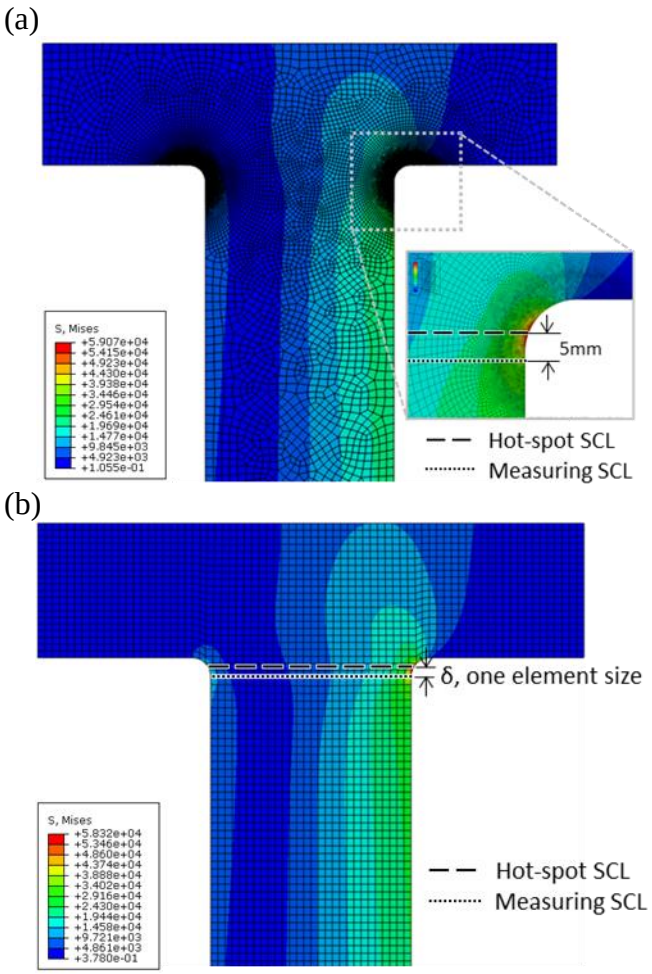

Fig. 3.11. Stress at single point away from the hot-spot approach in two different ways (a) Meshed with a gradual mesh refinement near the hot-spot and stress measured at 0.2 in. (5mm) away from the-hot-spot, (b) Measuring one element away from the hot-spot, illustrated on the 0.4 in. (10.2 mm) uniform mesh size.

The results of single point away from the hot-spot shows some improved trend result when it reaches the hot-spot compared to the stress linearization result. Fig. 3.12 (a) shows the structural stress ratio results among the four different mesh sizes at the hot-spots and reference point. There was no significant differences in the results between the two distances, both the one element away and 5 mm away. That is, the mesh size was not affecting the structural stress result. The hot-spot structural stresses were smaller than the nominal stress, but the decreased amount at hot-spots were smaller than the stress linearization approach (see Table 3.4). In Fig. 3.12 (b), the structural stress ratio shows a decrease when it approaches the hot-spot. Comparing the FEA linearization result derived in section 3.4.1, plotted in dotted line in Fig. 3.12 (b), this single

element away approach (of 0.4 in. (10 mm) mesh size) showed an increase in stress at the hot-spots. However, the structural stress at the hot-spot with this approach is not significant compared to the FEA linearization result. It is assumed that the measured location still has the peak stress, but somewhat alleviated. Still the influence of the increase in stress components exists. Therefore, the increased stress in each component will be examined next.

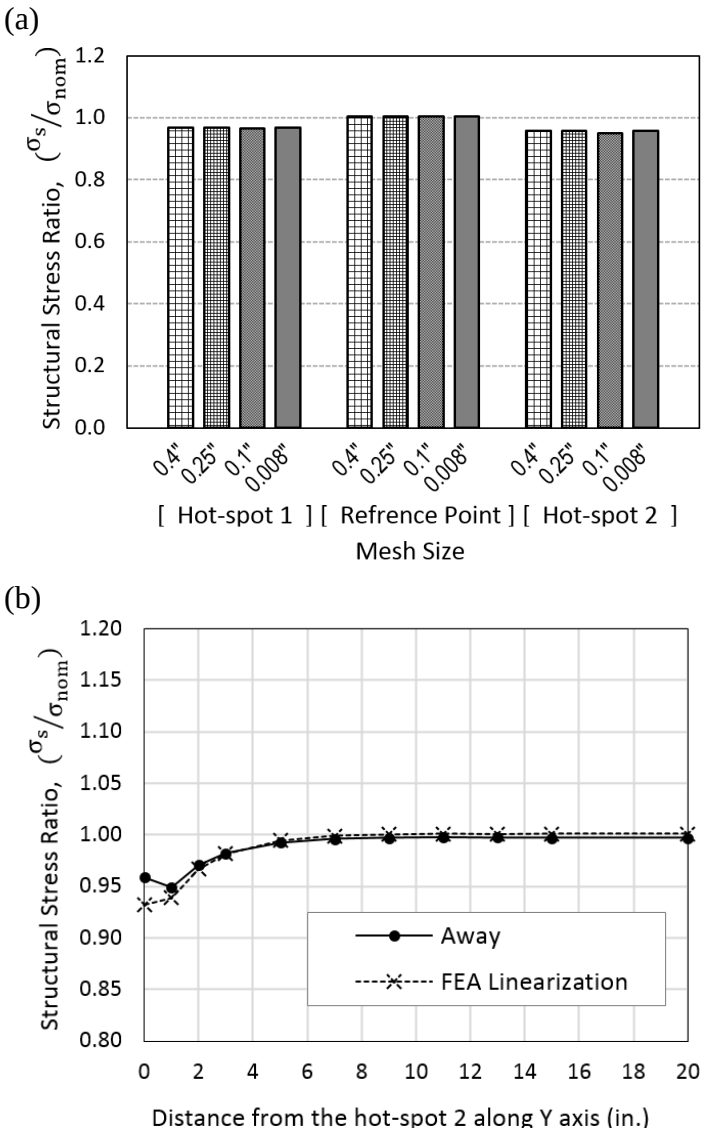

Fig. 3.12. Structural stress result at single point away from the influence area of hot-spot according to Niemi et al. [63]

(a) Comparison of Mesh sensitivity at hot-spot and the reference point, (b) Distribution of the structural stress close to the singularity, comparing the fillet model and the no fillet model in ABAQUS linearization at hot-spot 2 with 0.4 in. (10.2 mm) mesh size (To convert to mm, multiply values in inches by 25.4.)

3.4.3 Stress Extrapolation

From the 3D example stress analysis (see Fig. 3.5), the exaggerated stress components near the singularity were observed. The stress extrapolation approach is used in Kalnins` study [64] to modify the increased stress components near the singularity. In Kalnins approach, the exaggerated stresses are modified by extrapolating from the valid SCL location as illustrated in Fig. 3.13. Therefore, the equivalent stress did not reduce considerably compared to the equivalent von Mises structural stress disturbed by singularity. The reasonable value for the exaggerated stress components are various per estimating methods. While Kalnins proposed the extrapolating value for the exaggerated stress, Gordon [71] suggested to use the nominal stress value which can be calculated from the mechanical loads. This study used both concepts depending on the stress components. According to the ASME BPVC Section VIII-2, the valid SCL definition for the normal stress component is where the stress distribution across the SCL (through the thickness) varies monotonically. In case of the shear stress distribution, the distribution shape is close to the parabolic at a valid SCL location.

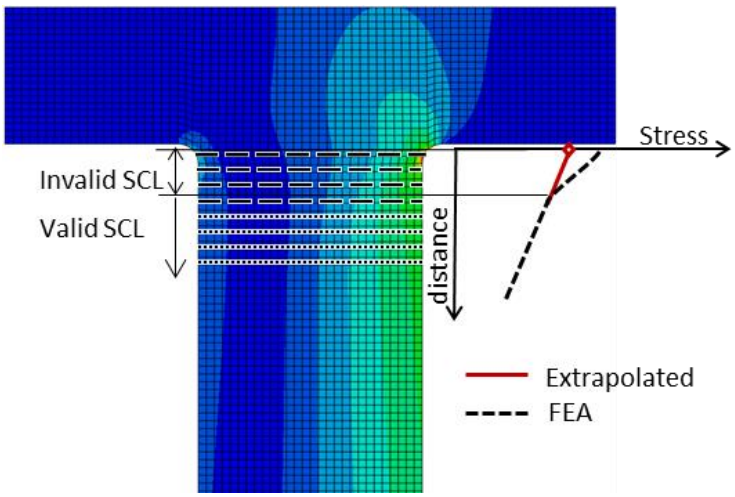

Fig. 3.13. Stress extrapolation from the valid SCL

The distribution across the SCL plot for each stress component is derived by stress linearization by the FEA program, illustrated in Fig. 3.14.

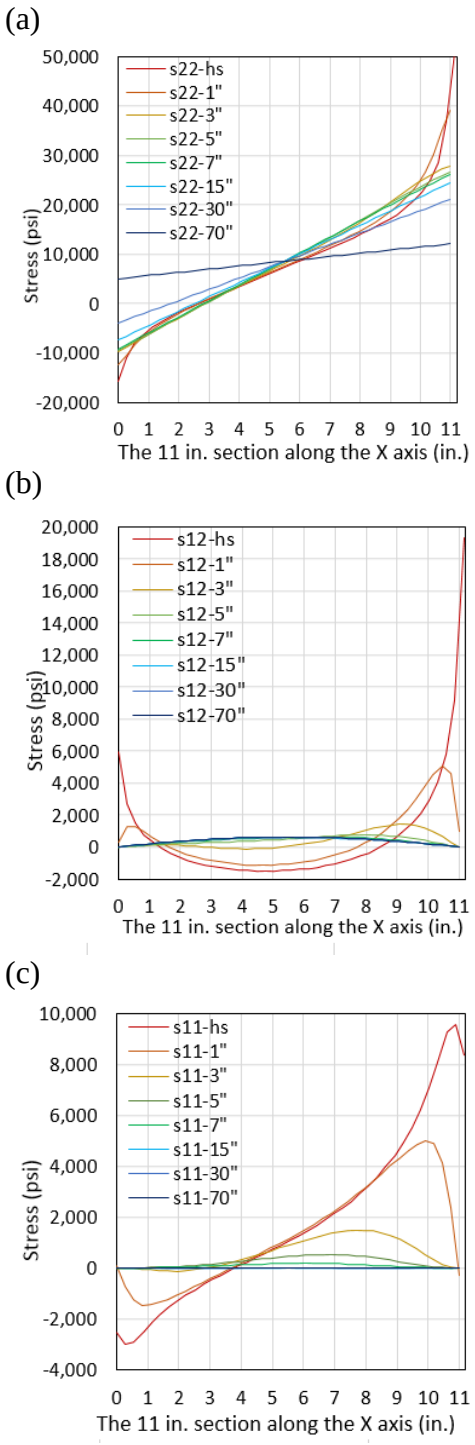

Fig. 3.14. Distribution of stress components across the 11 in. (279 mm) section along the X axis (a) S22 (normal stress perpendicular to SCL direction) distribution, (b) S12 (shear stress across the along the SCL direction) distribution, (c) S11 (normal stress in SCL direction) distribution (To convert to MPa, multiply values in psi by 0.0069. To convert to mm, multiply values in inches by 25.4.)

The distribution across the SCL plot for each stress component is derived by stress linearization by the FEA program, illustrated in Fig. 3.14. This figure shows the variations of through thickness stress distribution with respect to the distance from the singularity along the *Y* axis in each color. The red color line which fluctuates greatly is the hot-spot stress distribution, while the black color line of almost no fluctuation is the stress distribution measured at 70 in. (1.8 m) away from the hot-spot. As the measurement distance goes far away from the hot-spot, the distribution plot shows a reduction in fluctuation trend. The SCLs away from the hot-spot locations are schematically illustrated in Fig. 3.13. Generally, as the SCL is far away from the hot-spot, the graphs are showing gradual variation with smaller slopes. Among them, three locations are selected to represent the plot in Fig. 3.15. The selected locations are 1 in. (25.4 mm) distance, 6 in. (152 mm) distance, and 20 in. (508 mm) distance from the hot-spot.

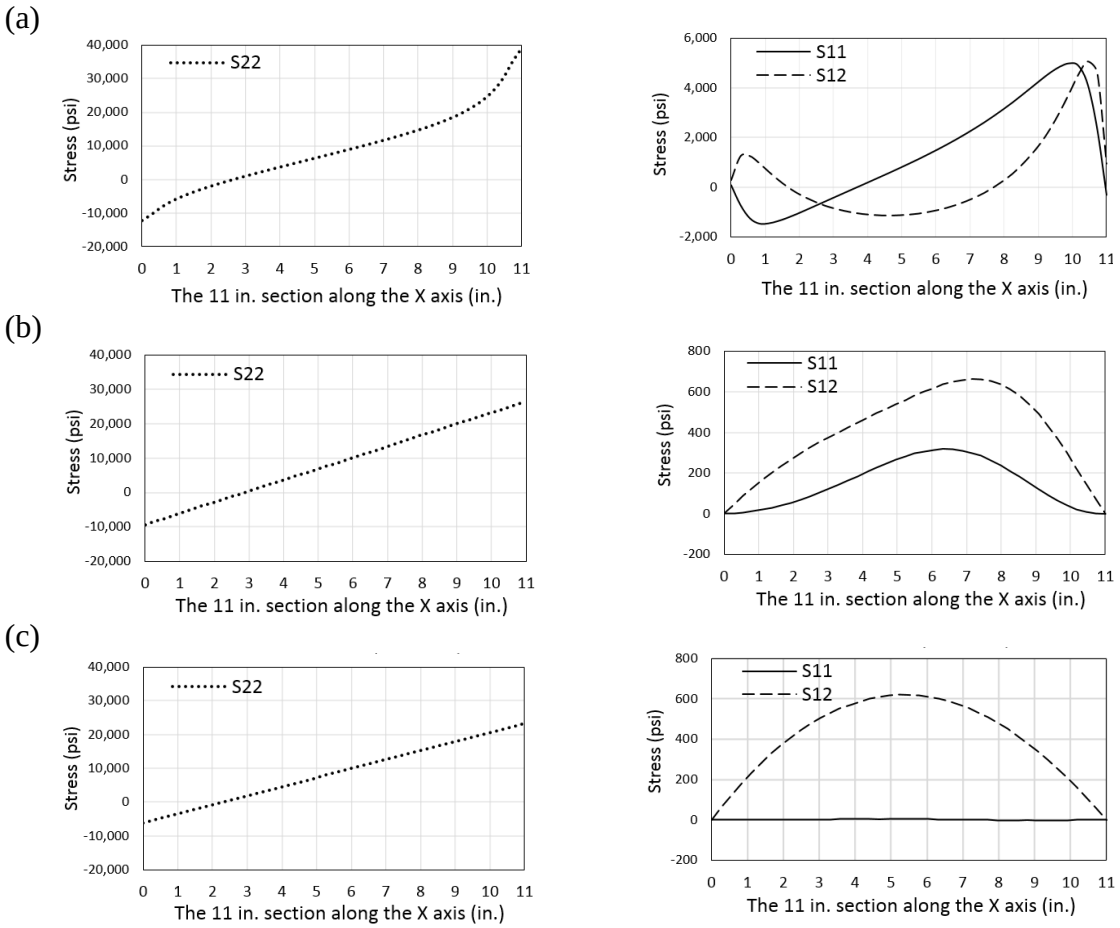

Fig. 3.15. Stress distribution from FEA linearization result

(a) Normal stress plot across the section, measured at 1 in. (25.4 mm) away from the hot-spot, (b) Normal stress plot across the section, measured at 6 in. (152 mm) away from the hot-spot, (c) Normal stress plot across the section, measured at 20 in. (508 mm) away from the hot-spot

The normal stress S_{22} plot in Fig. 3.15 (a) to (c), shows that the S_{22} stress distribution is valid in all locations. They varied monotonically along the thickness except for the edges Fig. 3.15 (a), where the slopes are steeper than other locations due to the singularity effect. The slope of S_{22} decreases as it is measured further away from hot-spot.

At least 6 in. (152 mm) away from the hot-spot, the S_{12} distribution can be regarded as valid SCL. The shear stress, S_{12} plots show a parabolic shape in the case that it is measured further than 6 in. (152 mm) away from the hot-spot as shown in Fig. 3.15 (b). At the hot-spot, the S_{12} stress passing through the singularity shows exaggerated stress at the ends and shapes are distorted, rather than parabolic (Fig. 3.15 (a)). This means the S_{12} stress distribution in hot-spots is not valid.

Meanwhile, the S_{11} plots which hardly show the valid points, are not monotonic distribution in Fig. 3.15 (a) and (b). Even when it goes further, the S_{11} distribution at 20 in. (508 mm) away from a hot-spot dies out to zero as observed in Fig. 3.15 (c). The S_{11} value is questionable since the nominal value does not exist while the S_{22} and S_{12} are the resultant stress from of the applied load. The S_{12} stress was attributed to the F_y force, and S_{22} is originating from the F_z and M_y.

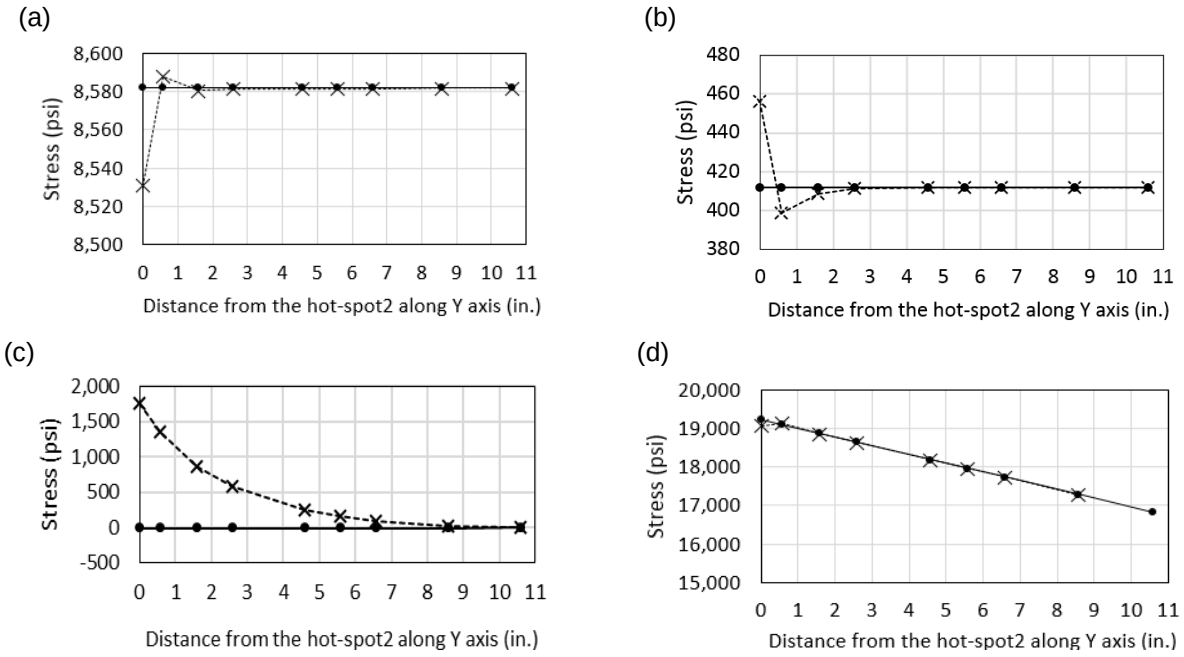

Fig. 3.16. Comparison of the stress in each component after extrapolation (dashed lines are from FEA linearization, solid lines are extrapolated)

(a) Normal stress plot across the section, measured at 1 in. (25.4 mm) away from the hot-spot, (b) Normal stress plot across the section, measured at 6 in. (152 mm) away from the hot-spot, (c) Normal stress plot across the section, measured at 20 in. (508 mm) away from the hot-spot

To extrapolate the stress from the valid points, further plots were generated. The average stress distribution with respect to the distance from the singularity in *Y* direction is shown in Fig. 3.16 and Fig. 3.17. The averaged stress variation along the *Y* direction and the extrapolated stress plots are illustrated together in Fig. 3.16. The valid points per stress components can be found in Fig. 3.17. In Fig. 3.16 (a), most of the $\sigma_{22(m)}$ value was computed as 8.58 ksi (59.2 MPa) consistently except in the vicinity of the singularity point. Near 1 in. (25.4 mm) from the singularity point, the $\sigma_{22(m)}$ slightly increased and soon reduced to 8.53 ksi (58.8 MPa) at the singularity. Although the S_{22} SCL distribution around 1 in. (25.4 mm) distance from the singularity was valid as shown in Fig. 3.15, the $\sigma_{22(m)}$ value near the singularity was extrapolated to match the nominal value, 8.58 ksi (59.2 MPa).

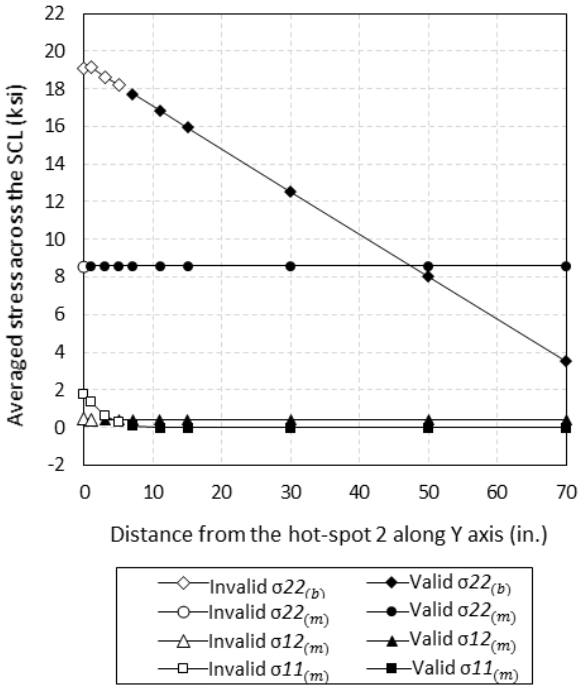

Fig. 3.17. Structural stress across the SCL along the distance from the singularity (Results from the FEA linearization. To convert to MPa, multiply values in ksi by 6.894. To convert to mm, multiply values in inches by 25.4.)

Likewise, the $\sigma_{12(m)}$ is 0.412 ksi (2.84 MPa) at any location because it is identical with the nominal $\sigma_{12(m)}$ except for three points closest to the singularity. The stress at these points showed steep fluctuation near the singularity as shown in Fig. 3.16 (b), so these three points are invalid. The $\sigma_{12(m)}$ value was extrapolated to 0.412 ksi (2.84 MPa) at the singularity.

As discussed about the nominal S_{11}, the $\sigma_{11(m)}$ does not originate from the mechanical loads. So, it needs engineering judgement to modify because there is no nominal value. The Fig. 3.16 (c) shows that the $\sigma_{11(m)}$ of singularity reaches to 1.7 ksi (11.7 MPa) but it soon drops and converges to zero value as it goes further away from hot-spot. Back to the Fig. 3.14 (c), the two surface points, 0 in. and 11 in. (279 mm) along the *X* axis, show a large stress increase. This exaggerated stress at the ends may contribute to the large membrane result near the hot-spot, so it is determined to ignore the abnormally exaggerated value. Therefore the $\sigma_{11(m)}$ extrapolation result is zero value in Fig. 3.16(c).

The bending stress, $\sigma_{22(b)}$ was extrapolated from the valid point, 6 in. (152 mm) distance away from the singularity. The valid point was defined following the $\sigma_{12(m)}$ valid point (Fig. 3.15(b)). The nominal bending stress should show a steady increase with a constant slope because the moment generated by the shear force weakens as it approaches the singularity. However, as shown in Fig. 3.17, the bending stress near the hot-spot slightly drops. To modify this decrease, the $\sigma_{22(b)}$ was extrapolated from the 6 in. (152 mm) distance away from the singularity. The valid and invalid stress components are illustrated in Fig. 3.17.

The structural stress in the hot-spot using the stress extrapolation approach shows improvement as compared to the two previous approaches, the stress linearization and the single point away approach. The structural stress results of this extrapolation approach are illustrated in Fig. 3.18. The SSR at hot-spot 2 was calculated based on the nominal stress at the fillet area. It is notable that extrapolated structural stress does not drop at any location in Fig. 3.18 (a). The reason for this result is that any disturbed stress component due to the singularity has been modified by extrapolating. The modifications are: 1) exaggerated stress is reduced, and 2) decreased stress is recovered to increase in accordance with the stress slope. Also, the mesh insensitivity is observed in the extrapolating approach as well. Furthermore, the structural stress does not drop compared to the nominal stress (see Fig. 3.18 (b)).

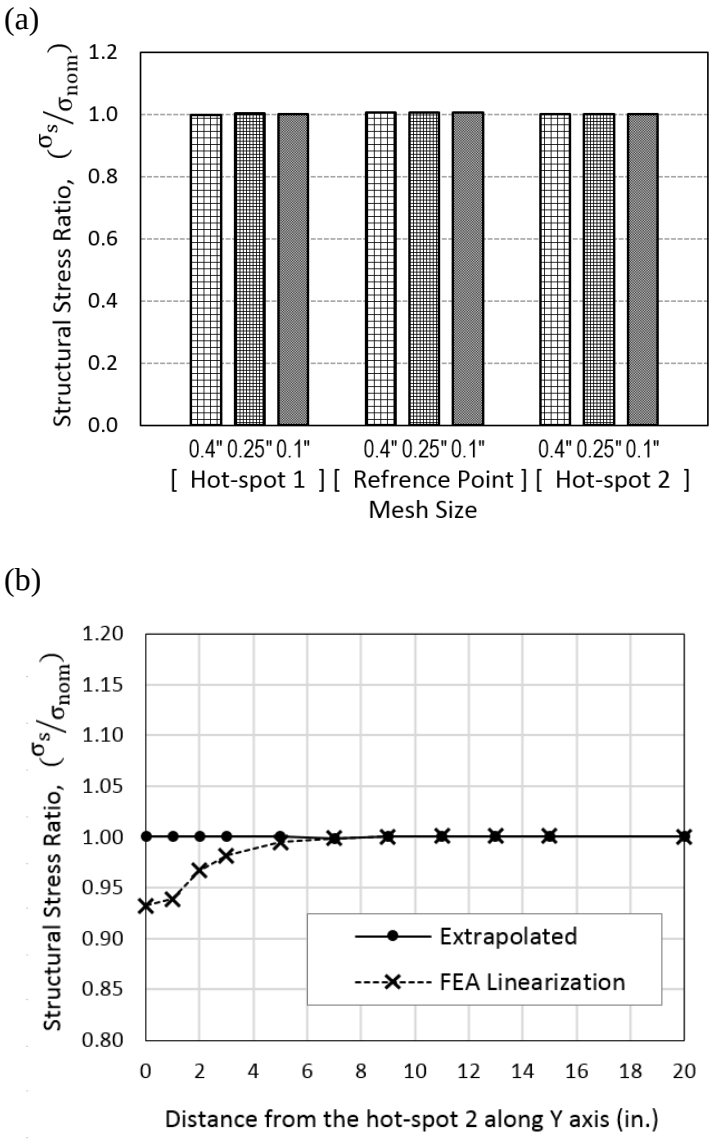

Fig. 3.18. Structural stress result from the stress extrapolating according to Kalnins [64]
(a) Comparison of mesh sensitivity at hot-spot and the reference point, (b) Distribution of the structural stress close to the singularity, comparing the structural stress from stress extrapolation method and the FEA linearization at hot-spot 2 with 0.4 in. (10 mm) mesh size (To convert to mm, multiply values in inches by 25.4.)

However, this extrapolation method needs engineering judgement to select the valid point and to define the right value of the uncertain stress components. This study referenced approaches of both Gordon [71] and Kalnins [64]. The stress components except for the $\sigma_{22(b)}$ and $\sigma_{11(m)}$, were extrapolated to match with the nominal value by hand calculation following

Gordon`s study [71] which proposed using the extrapolating value by the applied pressure. The $\sigma_{22(b)}$ was extrapolated using the slope of the valid SCL point, which was 6 in. (152 mm) in this study, following the one of the extrapolating approach of Kalnins [64]. Meanwhile, the $\sigma_{11(m)}$ value modified as zero was used another approach of Kalnins [64] adjusting the uncertain stress component to zero value for simple and conservative stress intensity result.

3.4.4 Stress in Equilibrium of Stress Resultants

This hot-spot structural stress determination method using stress equilibrium developed by Dong [77] is independent of mesh size and loading combination. This method is based on the structural equilibrium condition at both the hypothetical crack plane (A-A') and the reference plane (B-B'). It should be noted that in a fatigue analysis, the structural stress distribution used for the analysis is the stress that is normal to the assumed hypothetical crack plane [90]. Following this stress equilibrium approach, the stress distribution illustrated in Fig. 3.19 represents the S_{22} stress of the B-B' plane which is the largest stress component in this model.

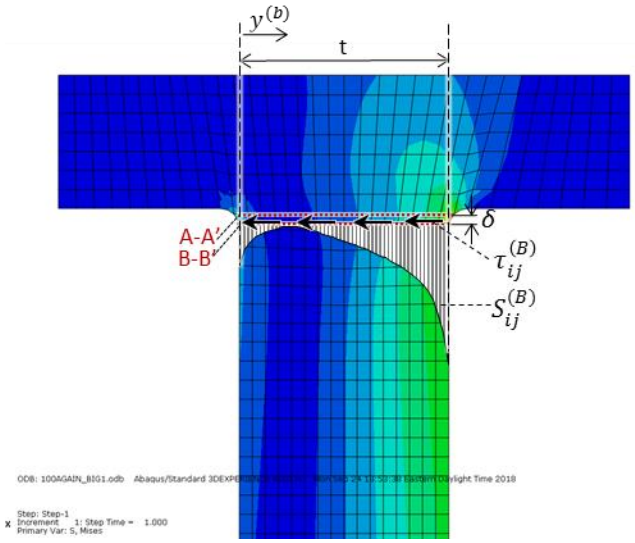

Fig. 3.19. Structural stress calculation for stress equilibrium method according to Dong [77] (plotted on the von-Mises stress result)

Not only the S_{22} stress, but the shear stress (S_{12}) which flows in B-B' is applied to Eq. (24) and (25) for the equilibrium with the A-A' hot-spot structural stress. Equation (24) shows the balanced membrane stress and equation (25) is based on the moment equilibrium between A-A' and B-B' sections.

$$\sigma_{ij(m)}^{(A)} = \frac{1}{t}\int_0^t S_{ij}^{(B)}\, dy \tag{24}$$

$$\sigma_{ij(m)}^{(A)} \cdot \frac{t^2}{2} + \sigma_{ij(b)}^{(A)} \cdot \frac{t^2}{6} = \int_0^t S_{ij}^{(B)}\left(y^{(B)}\right) dy + \delta \int_0^t \tau_{ij}^{(B)}\, dy \tag{25}$$

where,

$\sigma_{ij(m)}^{(A)}$: Membrane stress tensor of section A-A', at the hot-spot

$S_{ij}^{(B)}$: Normal stress component of section B-B' (S_{22} in this 2D study)

t : Thickness of the section along the *X* axis (see Fig. 3.19)

$\sigma_{ij(b)}^{(A)}$: Bending stress tensor of section A-A', at the hot-spot

$y^{(B)}$: Distance from the end of section B-B'

δ : Distance between section A-A' and B-B', one element size

$\tau_{ij}^{(B)}$: Transverse shear stress component of section B-B' (S_{12} in this study)

The structural stress ratio result using these equilibrium equations is shown in (a). The structural stress ratio *SSR* is 1.00 in hot-spots 1 and 2 which is the average of the three different mesh size results. Comparing these results to the stress linearization results of Section 3.4.1, in Fig. 3.20 (b), the distribution near the hot-spot is higher than the linearization result. The applied stress in this method excludes the stress that is not normal to the hypothetical crack section so that the structural stress does not drop near the hot-spot where typically other stress components rise to exaggerated values. It is interesting that, though, the method is different from extrapolation discussed in Section 3.4.3, and consequentially the considered stress components were very similar. Only the S_{22} and S_{12} were valid effective stress components but the S_{11} was ignored as zero value. Therefore, the result of the two structural stress estimation approaches are similar to each other.

(a)

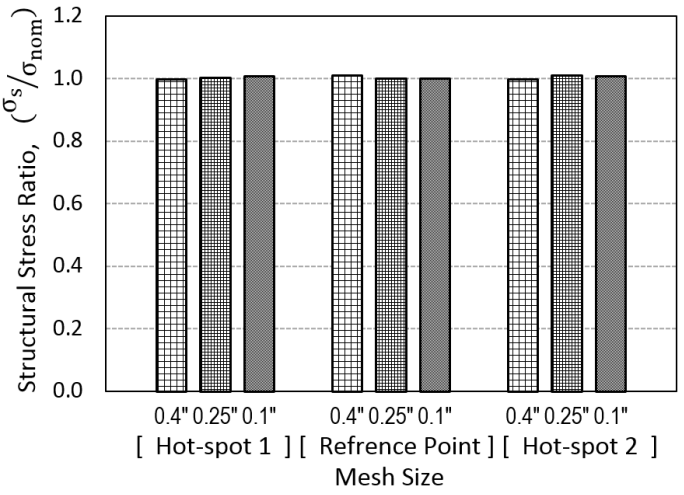

(b)

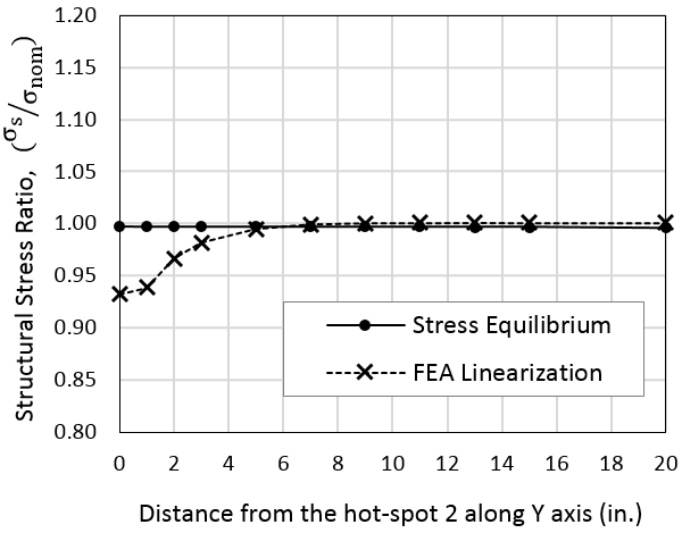

Fig. 3.20. Structural stress result from the structural stress equilibrium method according to Dong [77]

(a) Comparison of mesh sensitivity at hot-spot and the reference point, (b) Distribution of the structural stress close to the singularity, comparing the structural stress from stress equilibrium method and the FEA linearization at hot-spot 2 with 0.4 in. (10 mm) mesh size (To convert to mm, multiply values in inches by 25.4.)

3.4.5 Nodal Force Method

Stress calculation using the element nodal forces always yields a constant stress value regardless of the mesh size. This nodal force method was proposed by Gordon [71]. The structural stress were derived from the nodal forces of sets of the element using the Eq. (26) to (28)(28).

$$\sigma_{12(m)} = \frac{1}{t}\sum_{m=1}^{n} NFORC1_m \tag{26}$$

$$\sigma_{22(m)} = \frac{1}{t}\sum_{m=1}^{n} NFORC2_m \tag{27}$$

$$\sigma_{22(b)} = \frac{6}{t^2}\sum_{m=1}^{n} (x_m - x_c)NFORC2_m \tag{28}$$

where, t is the thickness of the section along the X axis at hot-spot, x_c is the centroid of the SCL line and x_m is the location which defines the nodal force location along the SCL. *NFORC* is the variable name that is used in ABAQUS. *NFORC*1 stands for the nodal force of the element stack in the X direction, *NFORC*2 is in the Y direction. The coordinates follow the global coordinate system, and the coordinate system is expressed in Fig. 3.21.

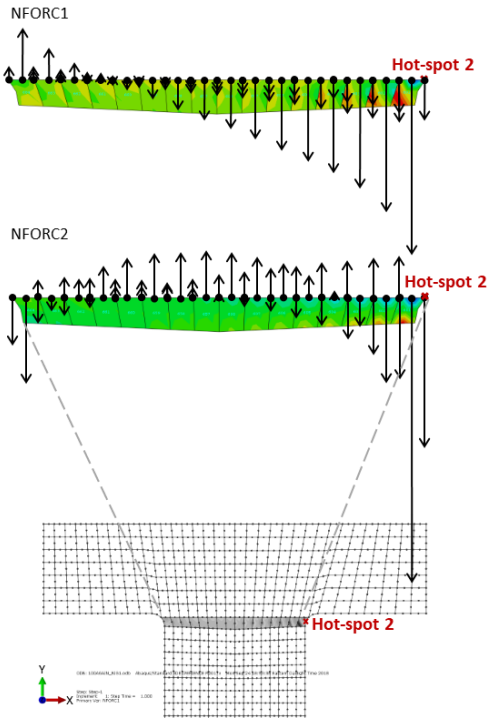

Fig. 3.21. Nodal force on the element stack across the structural hot-spot 2 according to Gordon [71] (plotted on the simplified with 1 in. (25.4 mm) element size analysis)

Fig. 3.21 represents the simplified 1 in. (25.4 mm) mesh element stack passing through the hot-spot 2 in the 2D *Y* direction model for illustration purpose. The arrows marked on the element stack represents nodal forces with the directions explained earlier are taken from the FEA output. The *NFORC*2 forces illustrated with vertical arrows correspond to the *Y* direction. However, the *NFORC*1 forces act in the horizontal coordinate, *X* coordinate, but the force arrows were rotated in the figure from horizontal to vertical to show the force distributions.

(a)

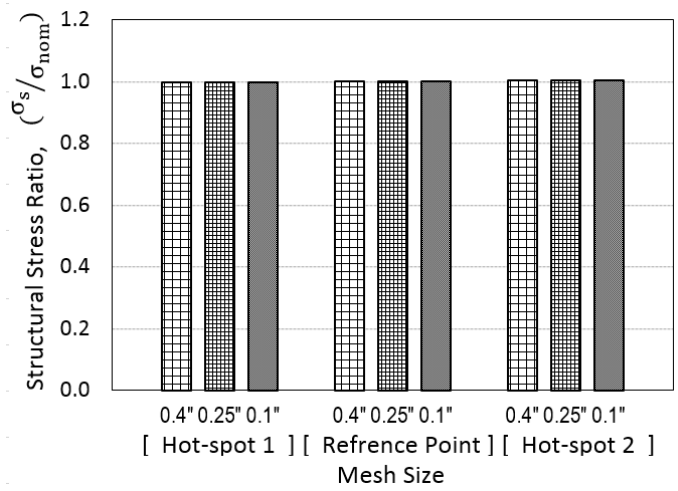

(b)

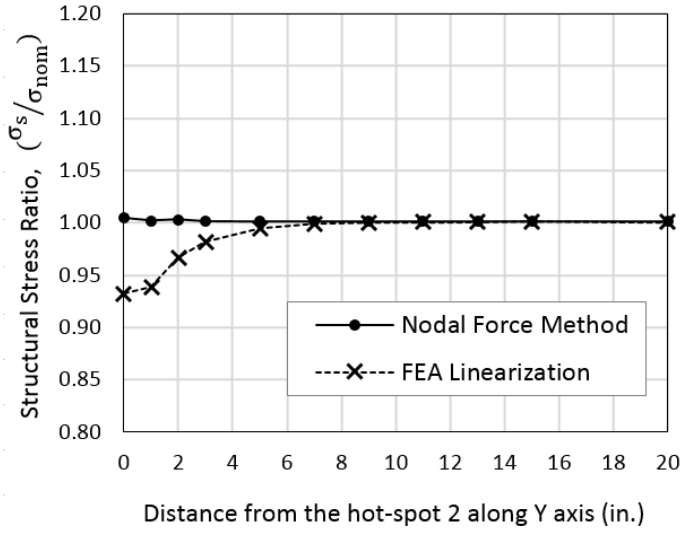

Fig. 3.22. Structural stress result from nodal force method according to Gordon [71], (a) Comparison of mesh sensitivity at hot-spot and the reference point, (b) Distribution of the membrane stress close to the singularity, comparing the structural stress from nodal force method and the FEA linearization at hot-spot 2 with 0.4 in. (10.2 mm) mesh size (To convert to mm, multiply values in inches by 25.4.)

The structural stress results in Fig. 3.22 show that wherever the elements stack is located, hot-spot 1, 2 or the reference location, the structural stresses obtained from this method were identical to the nominal values. The sum of *NFORC*2 was 94.4 kips (500 kN) and *NFORC*1 was 4.53 kips (20.2 kN) regardless of mesh size and locations. Thus, the $\sigma_{12(m)}$ was calculated as 0.412 ksi (2.84 MPa) and $\sigma_{22(m)}$ was 8.53 ksi (58.8 MPa) which are same as the nominal values from hand calculation. The *SSR* ratios of the stress by the nodal force method are identical regardless of the mesh size or location as shown in Fig. 3.22 (a). Fig. 3.22 (b) indicates that the structural stress using this method near the singularity does not drop. This trend is attributed to the fact that the structural stresses applied in the nodal force approach are accurate in any sizes of mesh, once the elements stack is lying in the same direction of the model. Particularly, the $\sigma_{11(m)}$ near the hot-spot commonly observed in the previous approaches in stress linearization (section 3.4.1) or the single point close to hot-spot (section 3.4.2) does not exist in this method because the $\sigma_{11(m)}$ is not the resultant of the mechanical forces applied in this study. This nodal force method was also implemented in Kalnins [64] based on the calculation from Gordon`s effective force edit [71]. Also, this nodal force method was introduced by Dong [77] for the shell and plate element models, when the section of interest is not available for the stress, such as lying in hot-spot, the force in opposite section taken by the nodal force method can compute the corresponding structural stress in the section of interest.

3.5 Structural Stress in 3D Coordinates

3.5.1 Stress Extrapolated from 3D FEA

The structural stresses of the 3D model were derived by extrapolating the stress from the stress linearization result. The stress linearization result before extrapolation was introduced in section 3.2 preliminary study. As briefly discussed in section 3.2, three considerations were derived from the stress linearization in 3D FEA analysis. As illustrated in Fig. 3.5, (i) it was obvious that all stress components were exaggerated near the hot-spot and this causes the structural stress drop. (ii) Even structural stress showed fluctuation at the singularity point because of the reentrant corner where fillet modelling was impossible. (iii) When the largest force (F_z) was applied, not only the stress $\sigma_{33(m)}$ in *Z* coordinate, but also stress components in other directions, such as $\sigma_{22(m)}$, $\sigma_{11(m)}$ were increased at the same time. This was studied by applying the load step

by step, as illustrated in Fig. 3.23. The stresses ($\sigma_{11(m)}$, $\sigma_{22(m)}$ and $\sigma_{33(m)}$) are membrane stresses measured at the hot-spot 2 in 3D model. Fig. 3.23 (a) is the membrane stress plots after the shear load (F_x, F_y) were applied. All stress values were small, nearly zero. Meanwhile, after applying the largest load, F_z, the membrane stress in Fig. 3.23 (b) were increased not only the $\sigma_{33(m)}$ membrane stress, but also the $\sigma_{22(m)}$ and $\sigma_{11(m)}$, which are not in the same direction of the load, F_z.

(a)

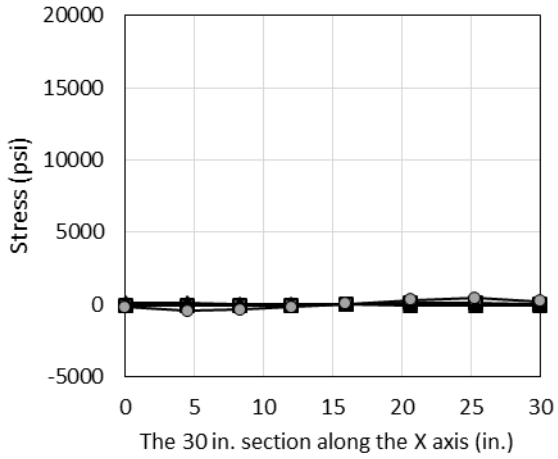

(b)

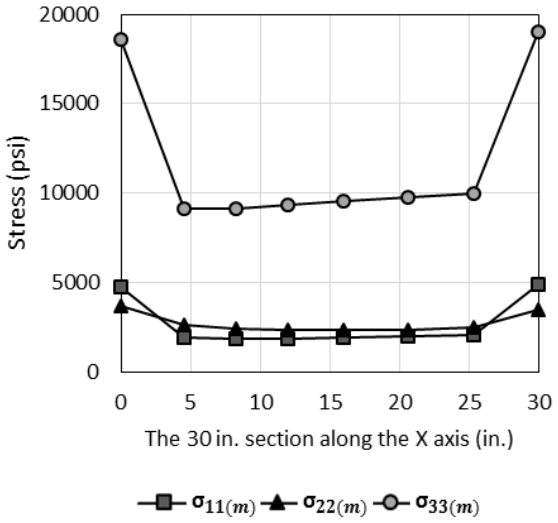

Fig. 3.23. The sequential plot of membrane stress components along the thickness of 30 in. (762 mm) of the 3D RPV support

(a) before the applying F_z force, (b) after applying F_z force (To convert to MPa, multiply values in psi by 0.0069. To convert to mm, multiply values in inches by 25.4.)

Hechmer and Hollinger [75] stated that the ASME BPVC Section III [37] stress limits were basically developed based on the shell theory. In thin shell analysis, the transverse shear stress is zero. However, these stresses need to be determined for 3D solid stress analysis. Grant et al. [91] found that the Poisson`s ratio effect should be considered particularly in three-dimensional FEA. From the stress linearization result derived from 3D FEA, the increased stress was not only the normal stress in the Z direction $\sigma_{33(m)}$ but also every stress component in all directions and it occurred at the same time. From this result, it can be claimed that the Poisson`s ratio affects the volumetric change which affects the stress analysis. Therefore, each stress component was extrapolated based on the valid SCL found by stress linearization. Particularly, stress extrapolation was carried in two directions, the Z coordinate and X coordinate as illustrated in Fig. 3.24.

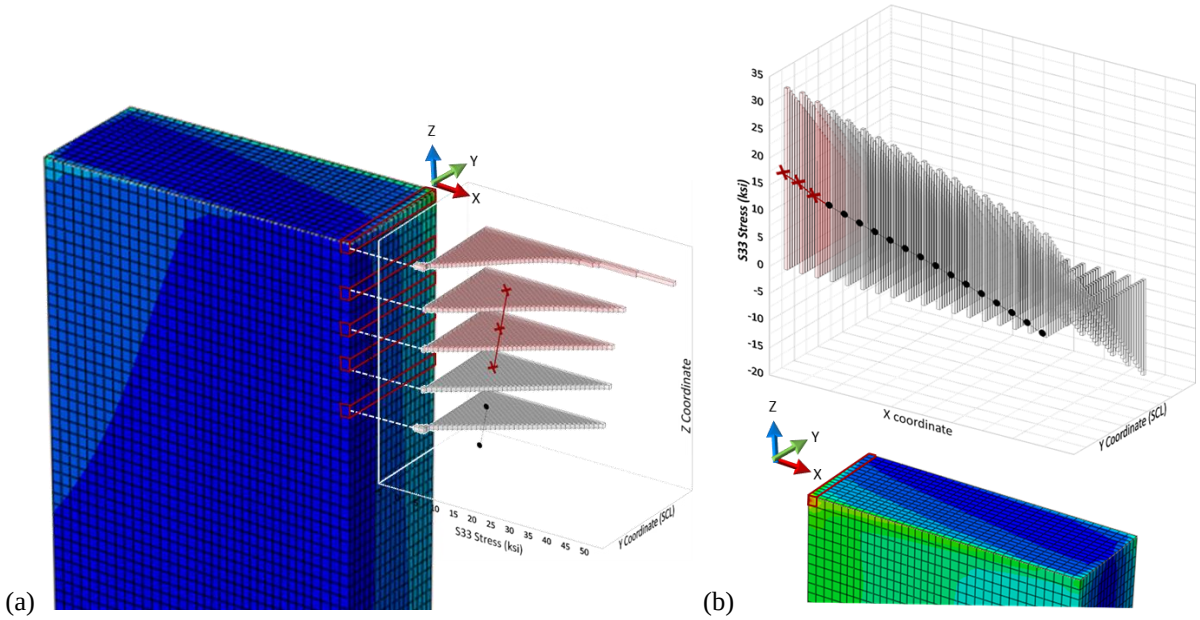

Fig. 3.24. Schematic illustration of stress extrapolation in 3D FEA according to Kalnins [64], (a) Extrapolating in Z coordinate, (b) Extrapolating in X coordinate (To convert to MPa, multiply values in ksi by 6.894.)

The SCL lies along the Y coordinate, the X and Z directions are the paths which are approaching the hot-spot SCL. The result of the structural stress (σ_s) using 3D extrapolation was 37.5 ksi (258 MPa) in hot-spot 1 and 36.4 ksi (251 MPa) in hot-spot 2. The nominal 3D structural stress by hand calculation in hot-spot 1 was 34.7 ksi (239 MPa) showing a 7.5% difference and 35.5 ksi (245 MPa) which is a 0.2% difference in hot-spot 2. The result from 3D extrapolation is

quite close to the nominal value obtained from the hand calculation. Given that the effect of the Poisson`s ratio was considered in 3D extrapolation, the extrapolated value appears may be more close to the nominal value because according to Grant et al. [91], the Poisson`s ratio effect generally produces a 5% difference.

3.5.2 Building the Structural Stress in 3D Using Two 2D Models

The 2D model was analyzed with five different structural stress determination approaches in Section 3.4. To evaluate the structural stress in 3D, the Cauchy stress matrix should be formed. Therefore, the *X* section in the 2D analysis was further analyzed. The hot-spot structural stress in the *X* section model was calculated by the same approaches as applied in the *Y* section. The matrix at the left bottom of Fig. 3.8 computes the structural stress(σ_s) by using two shear stresses and one normal stress and two bending stresses. This structural stress component composition in Fig. 3.8 is exclusively applicable for the 2D stress extrapolation, stress equilibrium and nodal force method because the disturbed stress components are not considered. The $S_{11}$and S_{22} positions may be filled in when the approaches are stress linearization and single point away approach depending on the existence of the computed stress components. The structural stress component matrix for the stress linearization and the single point away would be composed as below using Eq. (29) and (30). The Eq. (29) provides the structural stress (σ_s) which is included the membrane and bending stress and Eq. (30) is for the membrane stress (σ_m) only. The final result, the structural stress which are constructed by 3D matrix are given in Table 3.5 for hot-spot 1 and hot-spot 2, respectively.

$$\sigma_s = \begin{bmatrix} \sigma^{y}_{11(m)} & 0 & \sigma^{y}_{12(m)} \\ & \sigma^{x}_{11(m)} & \sigma^{x}_{12(m)} \\ & & \sigma^{x}_{22(m)}+\sigma^{x}_{22(b)} \\ symm. & & + \\ & & \sigma^{y}_{22(m)}+\sigma^{y}_{22(b)} \end{bmatrix} \tag{29}$$

$$\sigma_m = \begin{bmatrix} \sigma^{y}_{11(m)} & 0 & \sigma^{y}_{12(m)} \\ & \sigma^{x}_{11(m)} & \sigma^{x}_{12(m)} \\ symm. & & \sigma^{x}_{22(m)}+\sigma^{x}_{22(b)} \\ & & + \\ & & \sigma^{y}_{22(m)} \end{bmatrix} \quad (30)$$

Table 3.5 The structural stress constructed in 3D at hot-spots (in ksi [a])

Location	Stress	Stress in each method					
		Fillet [b]	Awy.[c]	Extr.[d]	SE.[e]	NF.[f]	3D.[g]
Hot-spot 1	σ_m	12.88	12.83	13.20	13.10	13.07	13.42
	σ_b	21.63	21.50	21.51	21.52	21.48	24.08
	σ_s	34.52	34.33	34.71	34.61	34.55	37.50
Hot-spot 2	σ_m	16.66	17.30	17.19	17.13	17.10	17.03
	σ_b	18.99	18.65	18.57	18.43	19.16	19.41
	σ_s	35.65	35.95	35.76	35.56	36.26	36.44

[a.] To convert to MPa, multiply values in table by 6.894
[b.] Linearized by ABAQUS in fillet model
[c.] Single point away from the influence area of hot-spot by Niemi et al. [63]
[d.] Stress extrapolated in 2D model by Kalnins [64]
[e.] Stress equilibrium method by Dong [77]
[f.] Nodal force method using by Gordon [71]
[g.] Stress extrapolated in 3D model by Kalnins [64]

3.6 The Structural Stress Results

To compare all the different structural stress estimating approaches used in 2D analysis, the hot-spot stress distribution graphs are plotted in Fig. 3.25 and corresponding numerical values are given in Table 3.4. The nominal stress value is the hand calculation which is shown in the red solid line. Four plots showed similar structural stresses as the nominal value : extrapolated stress by Kalnins [64], stress equilibrium by Dong [77], the nodal force method by Gordon [71] and the nominal value. These four plots including the nominal stress plot are hard to distinguish from each other due to the almost over-lapping results. On the other hand, the stress linearization and single point away stress values were lower than the other methods, showing decreased stress value starting from around 5 in. (127 mm) away from the hot-spot. The lowest hot-spot structural stress

was 25.2 ksi (174 MPa) determined using stress linearization and the highest was 27.1 ksi (187 MPa) obtained from the nodal force method. Even though the singularity was removed by fillet modelling and the stress linearization process readily excluded the peak stress, the result from stress linearization and single point away method considers all the stress components including those which were not generated by the applied force. Therefore, they still show decreased structural stress as it approaches to the hot-spot.

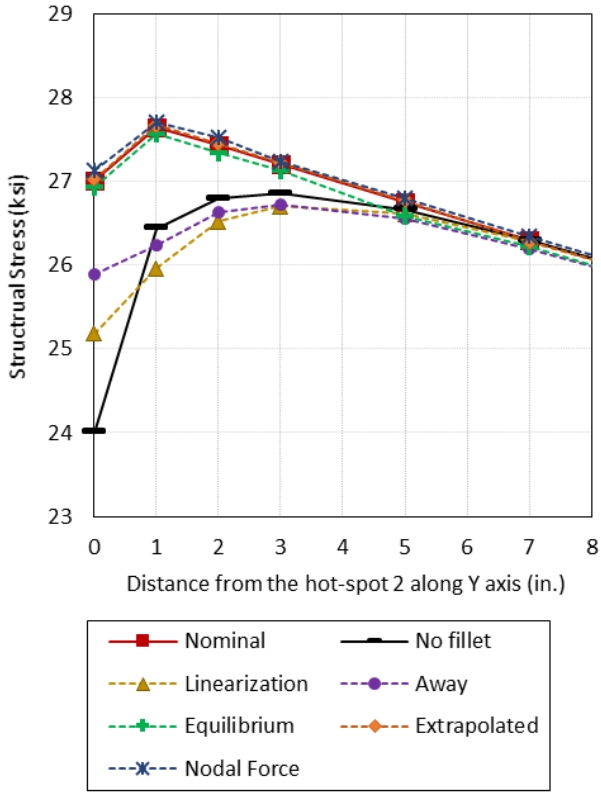

Fig. 3.25. Structural stress result along the Y axis from the singularity (To convert to MPa, multiply values in ksi by 6.894. To convert to mm, multiply values in inches by 25.4.)

Basically, the equilibrium approach [77] and the nodal force method [3], starts from same the equilibrium equation so the results are very similar to each other. The difference is what kinds of output are used for calculation, one is stress and the other is nodal force. Moreover, the nodal force and the stress equilibrium approach also do not have any stress which is produced by the geometry of the problem, and are solely produced by the actual applied load.

However, the stress components modified by extrapolating consequently are similar to the stress equilibrium even though extrapolation is not based on the equilibrium equation. The extrapolated stress neglects the stresses that are not from the mechanical forces and modifies the valid stress values by linear extrapolation from the valid point. Consequently, the stress component considered in the extrapolation is the same as the stress equilibrium, which is the stress normal to the postulated crack plane and the shear stress flows in the hot-spot section. Therefore, the results of stress extrapolation and stress equilibrium agree with each other quite closely.

Another important point to notice is that the maximum hot-spot location is not identical with respect to estimating approaches and is also different from the maximum von Mises stress distribution result from FEA. Orginally, the hot-spot was determined from the von Mises distribution result and it is located in the fillet area, which is the zero distance location of the horizontal axis of Fig. 3.25 graph. However, the maximum structural stress derived from 2D FEA study, stress extrapolation, nodal force method and stress equilibrium, was found at around 1 in. (25.4 mm) away from the maximum von Mises stress location. The stress distribution from FEA is displaying the total stress, so the non-linear peak stress is included. Even after removing the peak stress by the estimating approaches, the maximum structural stress was found at different location. In the case of the stress linearization or single point away approach, the maximum structural stress is located around 3 in. (76.2 mm) away from the maximum von Mises stress location while others showed the maximum structural stress point at 1 in. (25.4 mm) from the original hot-spot. Kyuba and Dong [92] found these differences in maximum stress location and maximum stress values between the different stress indices (such as von Mises stress or principal stress) and the actual crack location. One should be cautious to use the maximum stress result from FEA and conduct further investigation.

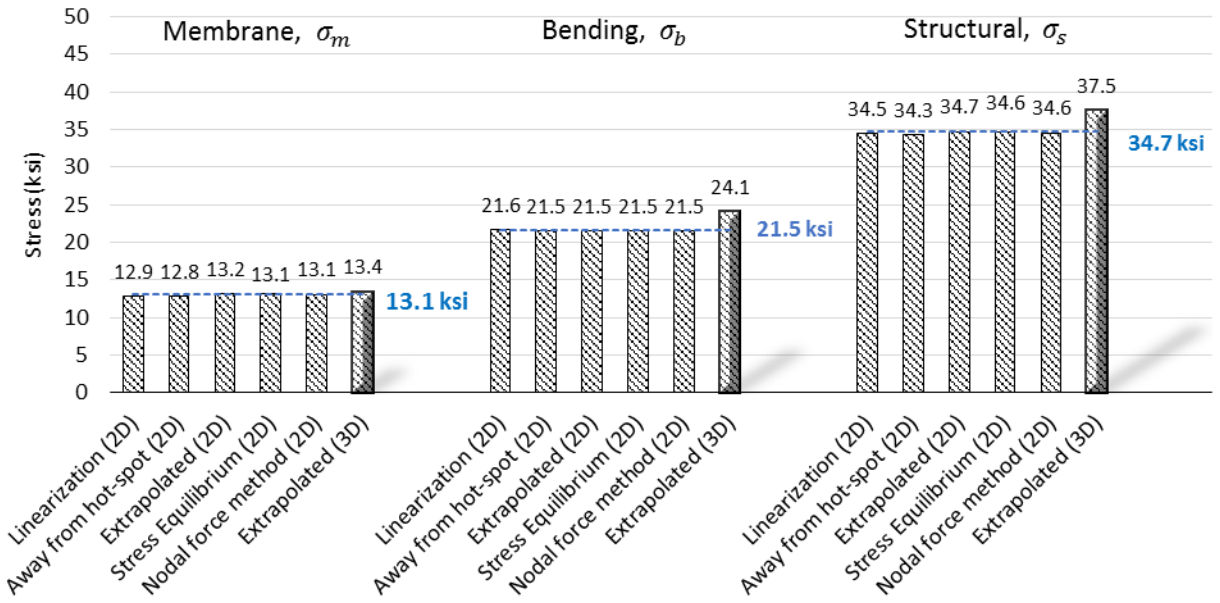

Fig. 3.26. Comparison of structural stress of hot-spot 1 in 3D coordinate

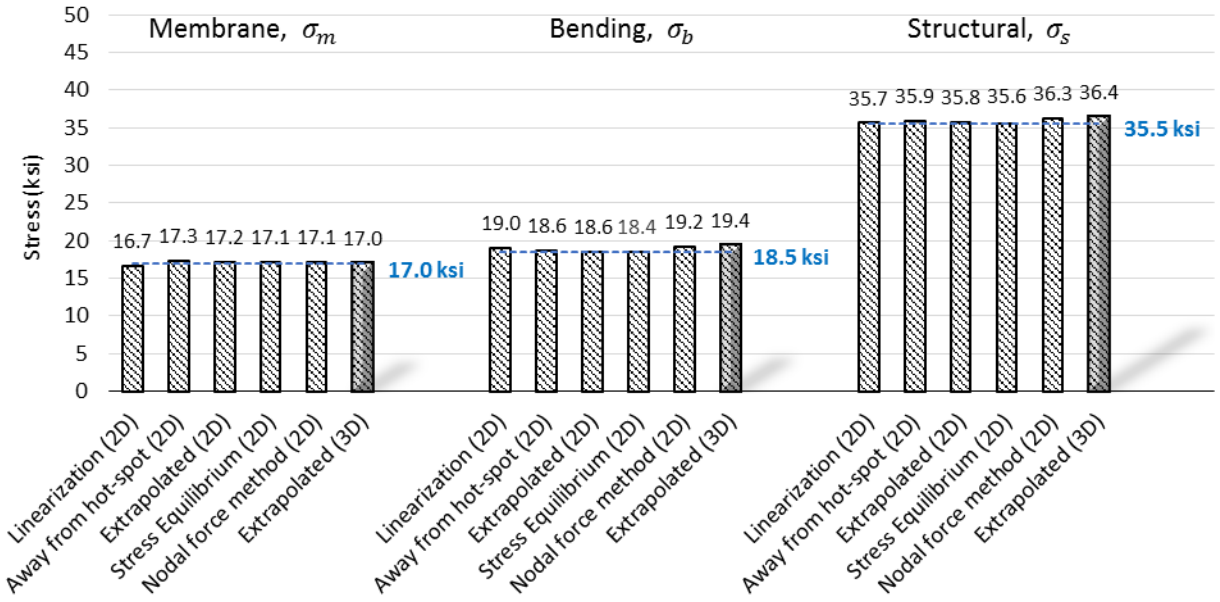

Fig. 3.27. Comparison of structural stress of hot-spot 2 in 3D coordinate

When stresses are reconstructed in 3D analysis, the difference between the different estimating approaches are almost removed. Fig. 3.26 and Fig. 3.27 show the comparison of 3D constructed structural stresses built from the 0.4 in. (10 mm) mesh - 2D model, hot-spot 1 and 2, respectively. The 3D extrapolated structural stress from section 3.5.1 and the nominal values expressed in blue dotted line are plotted together for comparison. While the structural stress difference in 2D analysis was about 2 ksi (13.8 MPa) in Fig. 3.25, most of the 3D analysis derived from 2D varies from only 0.38 to 0.71 ksi (2.6 to 4.9 MPa) each other. The 3D structural stresses derived from 2D are almost identical to the nominal values expressed in the dotted line. The reason seems to be that the principal stress does not have significant difference between the structural stress in different approaches when they are constructed in 3D. The exaggerated S_{11} stress is relatively small when it is constructed in 3D because the S_{33} stress components become considerable by summation of the two 2D FEA. The tension force in the *Z* direction is significant, therefore the other increased stress components were not countable as much as it affected in 2D analysis. Therefore, the 3D constructed structural stress shows constant value regardless of the estimating methods. Meanwhile, the 3D structural stress shows a rather higher value than others. It is assumed that the extrapolating point and the stress extrapolating slopes determined from the 3D analysis may be conservative.

3.7 Conclusions

The structural stress at hot-spot in FEA has demonstrated several estimating approaches without interference by numerical disturbances and has shown mesh insensitivity.

Using the 3D FEA stress linearization result without removing reentrant corners at hot-spots is hardly acceptable because it diverges depending on the mesh size. Also the structural stress at hot-spot shows a decrease due to the singularity effect. With the 2D FEA model, it was possible to remove the infinite stress value of the singularity by modelling the fillet. However, the 2D FEA stress linearization still has the exaggerated stress components that are not participating in the stress equilibrium of the structure.

The 2D structural stress estimating approaches, stress extrapolating used in Kalnins [64], stress equilibrium approach by Dong [77] and the nodal force method by Gordon [71] were applied in this study and they produce higher structural stress than the stress linearization results regardless of the mesh size. The structural stress from these approaches does not drop near the hot-spot. Given

that the stress extrapolating is sensitive to the SCL selection and assumptions to estimate the reasonable value, the stress equilibrium approach and the nodal force method are relatively, simple and clear.

The 3D stress matrix results were similar to each other in this study even though the 2D structural stress near the hot-spot showed a distinct difference. The principal stress difference generated near the hot-spot was alleviated by other large stress components, so the existence of that inaccurate stress does not affect the result. Comparing the extrapolated stress values in the 3D model, the results were similar but slightly higher than the exact solution. The reasons appear to be from the valid stress point selection which is an inherent variable in the extrapolating method and also the Poisson`s ratio which has a big impact particularly in the 3D model.

4. SUMMARY AND CONCLUSION

In this thesis, the neutron embrittled reactor pressure vessel support failure mode and its safety margin have numerically investigated with the use of the failure assessment diagram evaluation and finite element analysis focusing the structural stress value at hot-spot. The failure assessment diagram evaluated the structural integrity of reactor pressure vessel support in simplified values according to the different level of applied load and the neutron fluence. The long column type RPV support was considered to verify its safety under the maximum neutron fluence and maximum design level load events. The fracture toughness and yield strength affected by the neutron embrittlement in low irradiation temperature were numerically computed by the proposed empirical equations. The hot-spot structural stress of the RPV support was computed by extrapolating the linearized stress in 3D FEA model. Based on these physical properties and the structural stress, the postulated cracks were evaluated in the failure assessment diagram. The structural stress computed by the extrapolating approach in 3D FEA model was examined with the structural stress estimated in 2D FEA model by dividing the 3D

to two 2D plane. Reconstructed structural stress in 3D by a stress tensor components matrix shows similar result regardless of the five studied estimating approaches.

Based on the results of this thesis, for the neutron embrittled reactor pressure vessel, it is concluded in brief as follows:

- Under the event of a stress increase by accidents, the irradiated structure would lose its structural margin more than the unirradiated structure.
- The neutron embrittled physical properties were considerably influenced by the low irradiation temperature. The empirical equations for estimating fracture toughness and yield strength in certain irradiation level are developed using the reactor pressure vessel experimental data. Therefore, it should be cautious to determine the empirical equations for the fracture toughness estimation and they may need to be modified considering the low irradiation temperature effect.
- The fracture toughness decrease is expected to occur from initial state even before the 25% maximum design fluence level. Meanwhile the yield strength increases concurrently. The two variation trends of the fracture toughness and the yield strength vary in the earlier stage,

until 5% MDF. They do not change with respect to the neutron fluence levels after the 5% MDF.

- The hot-spot structural stress determination of 3D solid element analysis by using the stress linearization shows lower structural stress by substituting to the equivalent von Mises stress. Dividing the 3D model into two 2D plane models made possible to estimate structural stress in five different stress estimating methods. The differences results in the given by between each method in 2D model was essentially disappeared after reconstructing in 3D stress matrix.
- The postulated crack which is permissible in the preservice inspection found to be stable. However, if the crack size is increased to the in-service permissible crack size defined in ASME BPVC Section XI, the crack leads the support to the brittle fracture. The failure assessment diagram evaluation was conservative compared to the ASME BPVC Section XI assessment.

For future research, experimental studies of the low temperature irradiated steel respect to the neutron fluence are needed to enhance the accuracy of failure assessment. An impact test for the fracture toughness and tensile tests to define the modulus of elasticity and Poisson`s ratio should be investigated. The fracture toughness results computed by reactor pressure vessel empirical equations should be examined for the low irradiation temperature. The modulus of elasticity and the yield strength may be used to determine the standard stress-strain curve for the irradiated structural steel. Also, the Poisson`s ratio with respect to the level of embrittlement may be helpful in estimating the structural stress. Based on the mechanical properties from experimental studies, the elastic plastic fracture analysis would be possible and crack propagation modeling with dynamic finite element analysis may be applicable.

REFERENCES

[1] Commission, E., 2012, "Communication from the Commission Ti the Council and the European Parliament on the Comprehensive Risk and Safety Assessments ('Stress Tests') of Nuclear Power Plants in the European Union and Related Activities," Brussels, Belgium, p. COM(2012) 571 final.

[2] Miller, C., Cubbage, A., Dorman, D., Grobe, J., Holahan, G., and Sanfilippo, N., 2011, *Reccomendations for Enhancing Reactor Safety in the 21st Century*.

[3] U.S. Nuclaer Regulatory Commission, 1996, *NUREG-0933, Issue 15, Radiation Effects on Reator Vessel Supports (Rev. 3)*, Washington, DC 20555-0001.

[4] Brumovsky, M., 2010, "Irradiation Hardening and Materials Embrittlement in Light Water Reactor (LWR) Environments," Underst. Mitigating Ageing Nucl. Power Plants Mater. Oper. Asp. Plant Life Manag., pp. 357–373.

[5] U.S. Nuclear Regulatory Commission, 1989, *NUREG/CR-5320 Impact of Irradiation Embrittlement on Integrity of Pressure Vessel Supports for Two PWR Plants*, Washington, D.C. 20555.

[6] ASME, 2017, *BPVC.Section XI.Rules For Inservice Inspection Of Nuclear Power Plant Components*, New York, NY 10016-5990.

[7] API/ASME, 2016, *API 579-1/ASME FFS-1, Fitness-For-Service*, API Publishing Services, Washington, D.C.

[8] The British Standards Institution, 2015, *BS 7910, Guide to Methods for Assessing the Acceptability of Flaws in Metallic Structures*, London W4 4AL UK.

[9] 2003, *SINTAP(Structural Integrity Assessment Procedures for European Industry) Procedure Final Version*.

[10] 2015, *R6, Revison 4. Assessment of the Integrity of Structures Containing Defects*, Gloucester, UK.

[11] Barsom, J. M., and Rolfe, S. T., 1999, *Fracture and Fatigue Control in Structures : Applications of Fracture Mechanics*, ASTM, West Conshohocken, PA.

[12] Callister, W. D., and Rethwisch, D. G., 2010, *Materials Science and Engineering: An Introduction*, John Willey&Sons,Inc, Hoboken, New Jersey.

[13] International Atomic Energy Agency, 2009, *Integrity of Reactor Pressure Vessels in Nuclear Power Plants*, International Atomic Energy Agency.

[14] U.S. Nuclaer Regulatory Commission, 1981, *NUREG-0705, Identification of New Unresolved Safety Issues Relating to Nuclear Power Plant Stations*, Washington, D.C. 20555.

[15] U.S. Nuclaer Regulatory Commission, 1996, *NUREG-1509, Radiation Effects on Reactor Pressure Vessel Supports*, Washington, DC 20555-0001.

[16] Korea Hydro & Nuclear Power Co, 2014, *APR 1400 Design Control Document*.

[17] Electric Power Research Institute, 2016, *Structural Model of PWR Concrete Reactor Pressure Vessel Supports-Revison 1*, Palo Alto, California 94304.

[18] Le Pape, Y., 2015, "Structural Effects of Radiation-Induced Volumetric Expansion on Unreinforced Concrete Biological Shields," Nucl. Eng. Des., **295**, pp. 534–548.

[19] Kryukov, A., Sevikyan, G., Petrosyan, V., and Vardanyan, A., 2014, "Irradiation Embrittlement Assessment and Prediction of Armenian NPP Reactor Pressure Vessel Steels," Nucl. Eng. Des., **272**, pp. 28–35.

[20] Lin, Y., Yang, W., Tong, Z., Zhang, C., and Ning, G., 2017, "Charpy Impact Test on A508-3 Steel after Neutron Irradiation," Eng. Fail. Anal., **82**(June), pp. 733–740.

[21] Yu, M., Luo, Z., and Chao, Y. J., 2015, "Correlations between Charpy V-Notch Impact Energy and Fracture Toughness of Nuclear Reactor Pressure Vessel (RPV) Steels," Eng. Fract. Mech., **147**, pp. 187–202.

[22] Li, C., Shu, G., Liu, Y., Huang, Y., Chen, J., Duan, Y., and Liu, W., 2018, "Effects of Neutron Irradiation on Resistivity of Reactor Pressure Vessel Steel," J. Nucl. Mater., **499**, pp. 446–450.

[23] Qian, G., González-Albuixech, V. F., and Niffenegger, M., 2018, "Effects of Embedded Cracks and Residual Stresses on the Integrity of a Reactor Pressure Vessel," Eng. Fail. Anal., **90**(January), pp. 451–462.

[24] Murtaza, U. T., and Javed Hyder, M., 2018, "Fracture Analysis of the Set-in Nozzle of a PWR Reactor Pressure Vessel – Part 1: Determination of Critical Crack," Eng. Fract. Mech., **192**, pp. 343–361.

[25] U.S. Nuclear Regulatory Commission, 2015, “Fracture Analysis of Vessels - Oak Ridge FAVOR , V04 . 1 , Computer Code : Theory and Implementation of Algorithms , Methods , and Correlations Office of Nuclear Regulatory Research,” pp. 1–26.

[26] Bass, B. R., Dickson, T. L., and Williams, P. T., 2017, “PVP2017-65262 Nuclear Reactor Pressure Vessels 1,” pp. 1–10.

[27] González-Albuixech, V. F., Qian, G., Sharabi, M., Niffenegger, M., Niceno, B., and Lafferty, N., 2016, “Integrity Analysis of a Reactor Pressure Vessel Subjected to a Realistic Pressurized Thermal Shock Considering the Cooling Plume and Constraint Effects,” Eng. Fract. Mech., **162**, pp. 201–217.

[28] Chou, H. W., and Huang, C. C., 2016, “Fracture Risk Assessment for the Pressurized Water Reactor Pressure Vessel under Pressurized Thermal Shock Events,” Nucl. Eng. Des., **300**, pp. 412–421.

[29] Chen, B. Y., Huang, C. C., Chou, H. W., Lin, H. C., Liu, R. F., Weng, T. L., and Chang, H. J., 2014, “Reactor Pressure Vessel Integrity Assessment by Probabilistic Fracture Mechanics - A Plant Specific Analysis,” Int. J. Press. Vessel. Pip., **117**–**118**, pp. 64–69.

[30] Bergant, M. A., Yawny, A. A., and Perez Ipiña, J. E., 2015, “Structural Integrity Assessments of Steam Generator Tubes Using the FAD Methodology,” Nucl. Eng. Des., **295**, pp. 457–467.

[31] Zaccari, N., Caria, S., and Rubeo, G., 2014, “High Energy Pipe Break Analysis for a Main Steam Line of a WWER NPP,” Nucl. Eng. Des., **266**, pp. 100–111.

[32] Payten, W. M., Wei, T., Snowden, K. U., Bendeich, P., Law, M., and Charman, D., 2011, “Crack Initiation and Crack Growth Assessment of a High Pressure Steam Chest,” Int. J. Press. Vessel. Pip., **88**(1), pp. 34–44.

[33] Bakhtiari, R., Zangeneh, S., Bakhtiari Fotouh, M., Jamshidi, S. M., and Shafeie, A., 2017, “Fitness for Service Assessment of a Pressure Vessel Subjected to Fire Damage in a Refinery Unit,” Eng. Fail. Anal., **80**(July 2016), pp. 444–452.

[34] Li, Y., Miura, N., Hasegawa, K., and Hoshino, K., 2015, “Experimental Study On Failure Estimation Method For Circumferentially Cracked Pipes Subjected To Multi-Axial Loads,” ASME 2015 Press. Vessel. Pip. Conf., **139**(February 2017), pp. 1–10.

[35] Nagai, M., Miura, N., and Shiratori, M., 2015, "Stress Intensity Factor Solution for a Surface Crack with High Aspect Ratio Subjected to an Arbitrary Stress Distribution Using the Influence Function Method," Int. J. Press. Vessel. Pip., **131**, pp. 2–9.

[36] Gregg, R. E., Smith, C. L., and Garner, R. W., 1994, "Cost/Benefit Analysis of GSI-15:Radiation Effects on Reactor Vessel Supports (Final Report)."

[37] ASME, 2015, *BPVC.Section III.Rules for Construction of Nuclear Facility Components, Division 1 -Subsection NF*, New York, NY 10016-5990.

[38] ASME, 2017, *BPVC. Section II.Materials Part A-Ferrous Materials Specifications*, The American Society of Mechanical Engineers, New York, NY 10016-5990.

[39] Nguyen, A. T., and Namgung, I., 2017, "Structural Assessments of Plate Type Support System for APR1400 Reactor," Nucl. Eng. Des., **314**, pp. 256–270.

[40] 10 CFR 50.61, 1995, *Fracture Toughness Requirements for Protection against Pressurized Thermal Shock Events*, 60 FR 65468, Dec. 19, 1995, as amended at Jan. 4, 2010, United States.

[41] U.S. Nuclaer Regulatory Commission, 1988, *Regulatory Guide 1.99 Radiation Embrittlement Of Reactor Vessel Materials*, Washington, DC 20555-0001.

[42] Anderson, T. L., 2005, *Fracture Mechanics: Fundamentals and Applications*, CRC, Boca Raton.

[43] Larrosa, N. O., and Ainsworth, R. A., 2016, "Comparisons of the Solutions of Common FFS Standard Procedures to Benchmark Problems," Int. J. Press. Vessel. Pip., **139**–**140**, pp. 36–46.

[44] Matlack, K. H., Kim, J. Y., Wall, J. J., Qu, J., Jacobs, L. J., and Sokolov, M. A., 2014, "Sensitivity of Ultrasonic Nonlinearity to Irradiated, Annealed, and Re-Irradiated Microstructure Changes in RPV Steels," J. Nucl. Mater., **448**(1–3), pp. 26–32.

[45] ASME, 2017, *BPVC.Section II.Materials Part D-Properties*, The American Society of Mechanical Engineers, New York, NY 10016-5990.

[46] ASTM, 2016, *E185 Standard Practice for Design of Surveillance Programs for Light-Water Moderated Nuclear Power Reactor Vessels*, West Conshohocken, PA 19428-2959.

[47] Dassault Systemes, *ABAQUS*, 2017, Providence,RI.

[48] Oak Ridge National Laboratory, 2007, *ORNL/TM-2006/530, A Physically Based Correlation of Irradiation-Induced Transition Temperature Shifts for RPV Steels*, Oak Ridge, TN 37831-6161.

[49] Eason, E. D., Odette, G. R., Nanstad, R. K., and Yamamoto, T., 2013, "A Physically-Based Correlation of Irradiation-Induced Transition Temperature Shifts for RPV Steels," J. Nucl. Mater., **433**(1–3), pp. 240–254.

[50] Electric Power Research Institute, 1984, *NP-3319 Physically Based Regression Correlations of Embrittlement Data From Reactor Pressure Vessel Surveillance Programs*, Palo Alto, California 94304.

[51] Haggag, F. M., 1993, *Effects of Irradiation Temperature on Embrittlement of Nuclear Pressure Vessel Steels*, The American Society for Testing and Materials, West Conshohocken, PA 19428-2959.

[52] Fabry, A., Velde, V. de, Puzzolante, J. L., Ransbeeck, T. V., Verstrepen, A., Biemiller, E. C., Carter, R. G., and Petrova, T., 1996, *Research to Understand the Embrittlement Behavior of Yankee/BR3 Surveillance Plate and Other Outlier RPV Steels*, The American Society for Testing and Materials, West Conshohocken, PA 19428-2959.

[53] Odette, G. R., and Lucas, G. E., 1986, "Irradiation Embrittlement of Reactor Pressure Vessel Steels: Mechanisms, Models, and Data Correlations," *Radiation Embrittlement of Nuclear Reactor Pressure Vessel Steels: An International Review, American Society for Testing and Materials*, ASTM STP 909, Philadelphia.

[54] U.S. Nuclaer Regulatory Commission, 1998, *NUREG/CR-6551 Improved Embrittlement Correlations for Reactor Pressure Vessel Steels*, Washington, DC 20555-0001.

[55] ASTM, 2015, *ASTM E900 Standard Guide for Predicting Radiation-Induced Transition Temperature Shift in Reactor Vessel Materials*, West Conshohocken, PA 19428-2959.

[56] ASTM, 2015, *Adjunct for ASTM E900-15 Technical Basis for the Equation Used to Predict Radiation Induced Transition Temperature Shift in Reactor Vessel Materials*, West Conshohocken, PA 19428-2959.

[57] Chaouadi, R., 2005, *SCK-CEN Report R-4235,An Engineering Radiation Hardening Model for RPV Materials*.

[58] Odette, G. R., Lombrozo, P. M., and Wullaert, R. A., 1985, *Relationship Between Irradiation Hardening and Embrittlement of Pressure Vessel Steels*, The American Society for Testing and Materials, West Conshohocken, PA 19428-2959.

[59] Wechsler, M. S., Berggren, R. G., Hinkle, N. E., and Stelzman, W, J., 1969, "Radiation Hardening and Embrittlement in a Reactor Pressure Vessel Steel," *Irradiation Effects in Structural Alloys for Thermal and , American Society for Testing and Materials*, ASTM STP 457, Philadelphia.

[60] Odette, G. R., and Lucas, G. E., 1998, "Recent Progress in Understanding Reactor Pressure Vessel Steel Embrittlement," Radiat. Eff. Defects Solids, **144**(1–4), pp. 189–231.

[61] Chaouadi, R., and Gérard, R., 2005, "Copper Precipitate Hardening of Irradiated RPV Materials and Implications on the Superposition Law and Re-Irradiation Kinetics," J. Nucl. Mater., **345**(1), pp. 65–74.

[62] ASME, 2017, *BPVC.Section VIII.Division 2 Alternative Rules*, The American Society of Mechanical Engineers, New York, NY 10016-5990.

[63] Niemi, E., Fricke, W., and Maddox, S. J., 2006, *Fatigue Analysis of Welded Components: Designer's Guide to the Structural Hot-Spot Stress Approach*, IIW International Institute of Welding, Cambridge, Woodhead.

[64] Kalnins, A., 2008, "Stress Classification Lines Straight Through Singularities," ASME Pressure Vessels and Piping Division Conference, Chicago, Illinois, USA, pp. 1–10.

[65] Hollinger, G., and Hechmer, J., 2000, "Three-Dimensional Stress Criteria—Summary of the PVRC Project," J. Press. Vessel Technol., **122**(1), p. 105.

[66] Electric Power Research Institute, 2017, "Carbon Macrosegregation in Large Forgings," *29th NRC Regulatory Information Conference*, Electric Power Research Institute, Rockville, MD.

[67] API/ASME, 2007, *API 579-1/ASME FFS-1, Fitness-For-Service*, API Publishing Services, Washington, D.C.

[68] U.S. Nuclaer Regulatory Commission, 1991, *NUREG-1407, Procedural and Submittal Guidance for the Individual Plant Examination of External Events (IPEEE) for Severe Accident Vulnerabilities*, Washington, DC 20555-0001.

[69] Margolin, B. Z., Yurchenko, V., Kostylev, V. I., Morozov, Varovin, A. Y., Rogozkin, S. V., and Nikitin, 2018, "Radiation Embrittlement of Support Structure Materials for WWER RPVs," J. Nucl. Mater., **508**, pp. 123–138.

[70] Kroenke, W. C., 1974, "Classification of Finite Element Stresses According to ASME Section III Stress Categories.," *Pressure Vessels Piping Conf*, Miami Beach, FL, pp. 107–140.

[71] Gordon, J. L., 1976, "Outcur: An Automated Evaluation of Two-Dimensional Finite Element Stresses Accordig to ASME Section III Stress Requirements," ASME Winter Annual Meeting, Paper 76-WA/PVP-16.

[72] Rudolph, J., Beckert, M., and Hauser, F., 2017, "Comparison of Methods for Structural Stress Determination According to EN 13445-3 ANNEX NA," *ASME 2017 Pressure Vessels and Piping Conference, ASME Paper No. PVP2017-66112*, pp. 1–11.

[73] Strzelczyk, A. T., and Stojakovic, M., 2013, "Simplified Stress Linearization Method, Maintaining Accuracy," J. Press. Vessel Technol., **135**(5), p. 051205.

[74] Hossain, M. M., Reinhardt, W. D., and Seshadri, R., 2009, "Simplified Stress Categorization Using a Single Linear Elastic Analysis," J. Press. Vessel Technol., **131**(6), p. 061204.

[75] Hechmer, J. L., and Hollinger, G. L., 1991, "The ASME Code and 3D Stress Evaluation," J. Press. Vessel Technol., **113**(November), pp. 481–487.

[76] Hechmer, J. L., and Hollinger, G. L., 1998, "3D Stress Criteria Guidelines for Application," Welding Research Council Bulletin No. 429.

[77] Dong, P., 2001, "A Structural Stress Definition and Numerical Implementation for Fatigue Analysis of Welded Joints," Int. J. Fatigue, **23**(10), pp. 865–876.

[78] Trieglaff, R., Rudolph, J., Beckert, M., and Hauser, F., 2017, "Comparison of Methods for Strutural Stress Determination According to EN 13445-3 ANNEX NA," *ASME 2017 Pressure Vessels and Piping Conference, ASME Paper No. PVP2017-66112*, pp. 1–11.

[79] Mukhtar, F. M., and Al-Gahtani, H. J., 2017, "Design-Focused Stress Analysis of Cylindrical Pressure Vessels Intersected by Small-Diameter Nozzles," J. Press. Vessel Technol. Trans. ASME, **139**(2), pp. 1–11.

[80] Kazemi, A., and Nassar, S. A., 2018, "Principal Stress-Based Equation for Multi-Axial Fatigue Analysis of Preloaded Threaded Fasteners," J. Press. Vessel Technol., **140**(2), p. 021405.

[81] Jaćimović, N., 2018, "Analysis of Piping Stress Intensification Factors Based on Numerical Models," Int. J. Press. Vessel. Pip., **163**(January), pp. 8–14.

[82] Kushan, D. S., Sanyal, S., and Bhowmick, S., 2018, "Parametric Study of Interaction Effect between Closely Spaced Nozzles in a Thin Cylinderical Pressure Vessel," Int. J. Press. Vessel. Pip., **165**(May), pp. 34–42.

[83] Lu, M.-W., Chen, Y., and Li, J.-G., 2000, "Two-Step Approach of Stress Classification and Primary Structure Method," J. Press. Vessel Technol., **122**(1), p. 2.

[84] Strzelczyk, A. T., and Ho, S. S., 2007, "Evaluation of 'Linearized' Stresses Without Linearization," *ASME 2007 Pressure Vessels and Piping Division Conference ASME Paper No. PVP2007-26357*.

[85] Hélénon, F., Wisnom, M. R., Hallett, S. R., and Allegri, G., 2010, "An Approach for Dealing with High Local Stresses in Finite Element Analyses," Compos. Part A Appl. Sci. Manuf., **41**(9), pp. 1156–1163.

[86] Rother, K., and Fricke, W., 2016, "Effective Notch Stress Approach for Welds Having Low Stress Concentration," Int. J. Press. Vessel. Pip., **147**, pp. 12–20.

[87] Muscat, M., Degiorgio, K., and Wood, J., 2009, "Comparison Between Different Approaches for the Evaluation of the Hot Spot Structural Stress in Welded Pressure Vessel Components," *ASME 2009 Pressure Vessels and Piping Division Conference ASME Paper No. PVP2009-77139*, pp. 1–10.

[88] Pedersen, M. M., 2016, "Multiaxial Fatigue Assessment of Welded Joints Using the Notch Stress Approach," Int. J. Fatigue, **83**, pp. 269–279.

[89] Mackenzie, D., 2017, "Stress Linearization Concepts and Restrictions in Elastic Design The ASME Boiler and Pressure Vessel Code Section," *ASME 2017 Pressure Vessels and Piping Conference, ASME Paper No. PVP2017-65678*, pp. 1–8.

[90] ASME, 2017, *BPVC.Section VIII.Division 2 Alternative Rules*, The American Society of Mechanical Engineers, New York, NY 10016-5990.

[91] Grant, R. J., Lorenzo, M., and Smart, J., 2007, "The Effect of Poisson's Ratio on Stress Concentrations," J. Strain Anal. Eng. Des., **42**(2), pp. 95–104.

[92] Kyuba, H., and Dong, P., 2005, "Equilibrium-Equivalent Structural Stress Approach to Fatigue Analysis of a Rectangular Hollow Section Joint," Int. J. Fatigue, **27**(1), pp. 85–94.

PUBLICATIONS

Journal Papers:

G.Han and S.Guzey, "A Study on the Brittle Fracture of the Neutron Embrittled Reactor Pressure Vessel Support in Low Irradiation Temperature" International Journal of Pressure Vessel and Piping (under review)

G.Han and S.Guzey, "Structural Stress Determination at a Hot-Spot" Journal of Pressure Vessel Technology (under review)

Conference Papers:

G.Han and S.Guzey, "Assessment of Structural Integrity On Irradiated Steel Structure: Focusing On Long Column Type Reactor Pressure Vessel Supports", ASME 2019 Pressure Vessels & Piping Conference, San Antonio, TX, July 14-19, 2019 (conference paper, in preparation)

G.Han and S.Guzey, "Structural Stress Determination Through Hot-Spot For Failure Assessment Using Finite Element Analysis", ASME 2019 Pressure Vessels & Piping Conference, San Antonio, TX, July 14-19, 2019 (presentation, in preparation)

G.Han and S.Guzey, "A Study on the Failure Analysis of Irradiated Reactor Pressure Vessel Support using Finite Element Analysis " SMiRT 25, Charlotte, NC, August 04-09, 2019 (conference paper, in preparation)